



Universiteit
Leiden
The Netherlands

Methanol masers and millimetre lines : a common origin in protostellar envelopes

Torstensson, K.J.E.

Citation

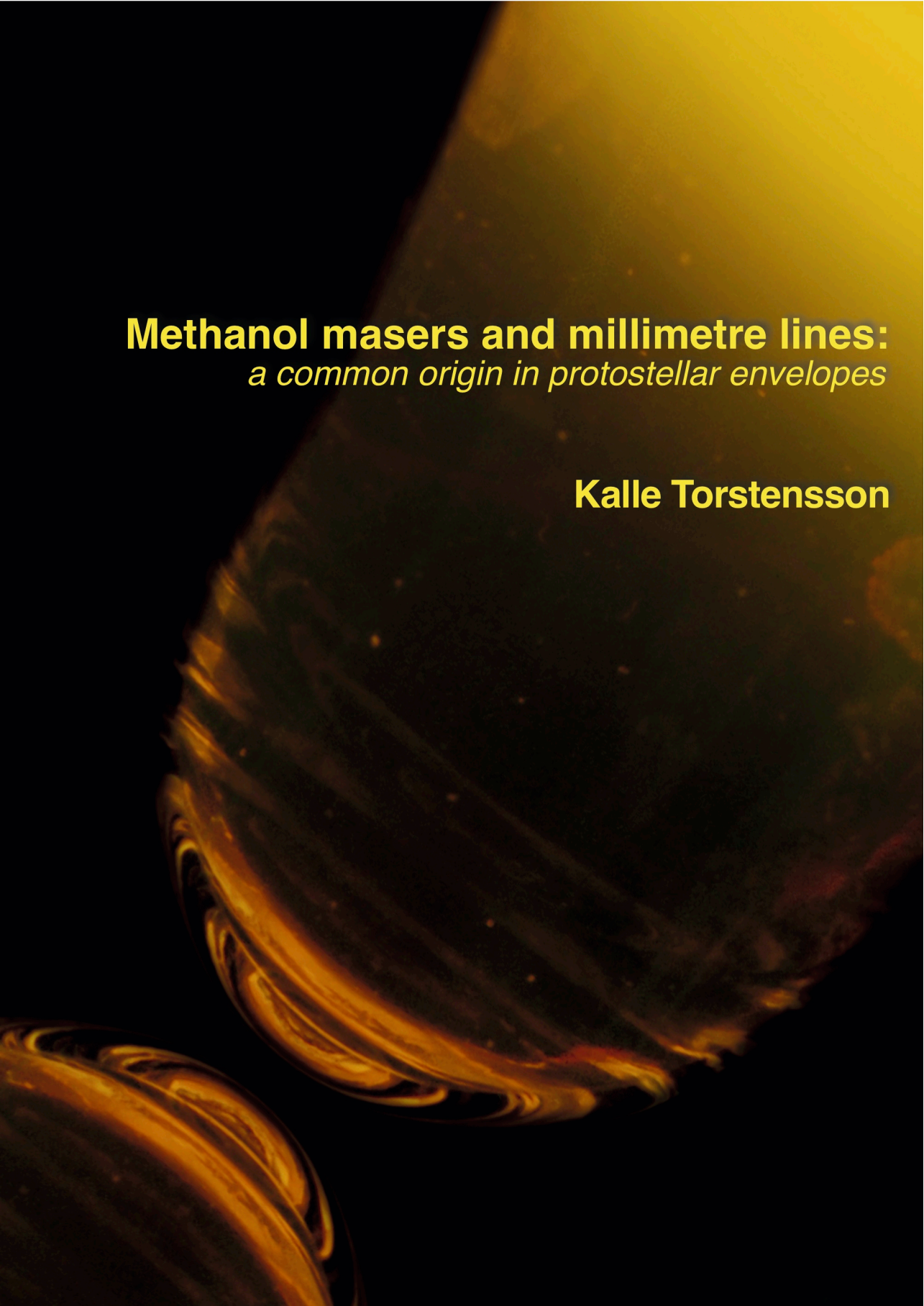
Torstensson, K. J. E. (2011, December 6). *Methanol masers and millimetre lines : a common origin in protostellar envelopes*. Retrieved from <https://hdl.handle.net/1887/18187>

Version: Corrected Publisher's Version

License: [Licence agreement concerning inclusion of doctoral thesis in the Institutional Repository of the University of Leiden](#)

Downloaded from: <https://hdl.handle.net/1887/18187>

Note: To cite this publication please use the final published version (if applicable).



Methanol masers and millimetre lines:
a common origin in protostellar envelopes

Kalle Torstensson

Methanol masers and millimetre lines:
a common origin in protostellar envelopes

Cover: Photograph of a shot glass filled with Rhodamine 6G laser dye dissolved in methanol. The dye is illuminated by the 355 nm output of a pulsed Nd:YAG laser. The exposure time of 25 s corresponds to ~250 pulses, each with a duration of 4 ns. Produced with a lot of help from Dr. Guss.

Methanol masers and millimetre lines:
a common origin in protostellar envelopes

PROEFSCHRIFT

ter verkrijging van
de graad van Doctor aan de Universiteit Leiden,
op gezag van de Rector Magnificus prof.mr. P.F. van der Heijden,
volgens besluit van het College voor Promoties
te verdedigen op dinsdag 6 december 2011
klokke 11.15 uur

door

Karl Johan Erik Torstensson
geboren te Högsbo, Sweden
in 1977

Promotiecommissie

Promotores: Prof. dr. E. F. van Dishoeck
Co-promotor: Dr. H. J. van Langevelde

Overige Leden: Prof. dr. K. Kuijken
Prof. dr. A. G. G. M. Tielens
Prof. dr. J. E. Conway
Dr. F. F. S. van der Tak
Dr. W. H. T. Vlemmings

Onsala Space Observatory
SRON Netherlands Institute for Space Research
Chalmers University of Technology

1	Introduction	1
1.1	Star formation	1
1.2	Molecular astrophysics	3
1.3	Masers	6
1.4	Radio interferometry	8
1.5	This thesis	8
1.6	Main conclusions	10
1.7	Future prospects and outlook	11
2	Dynamics of the methanol masers around Cepheus A HW2	13
2.1	Introduction	14
2.2	Observations and data reduction	15
2.2.1	6.7 GHz data	15
2.2.2	12.2 GHz data	17
2.3	Results	17
2.3.1	6.7 GHz results	17
2.3.2	12.2 GHz results	22
2.4	Analysis	24
2.4.1	Ring model	24
2.4.2	Parallax - distance	26
2.5	Discussion	27
2.6	Conclusions	28
3	Distribution and excitation of thermal methanol in Cepheus A	31
3.1	Introduction	33
3.2	Observations and data reduction	35
3.3	Results	37
3.3.1	Methanol lines	37
3.3.2	Spatial distribution of methanol	39
3.4	Analysis	41

Contents

3.4.1	Rotation diagrams	41
3.4.2	Population diagram modelling	43
3.4.3	Spatial distribution of the excitation	43
3.4.4	Non-LTE analysis	45
3.4.5	H ₂ column density	48
3.4.6	Methanol abundance	48
3.5	Discussion	50
3.5.1	Outflow morphology	50
3.5.2	Methanol distribution	50
3.5.3	Physical conditions	51
3.5.4	Origin of maser emission	52
4	Thermal methanol toward 6.7 GHz methanol maser sources	55
4.1	Introduction	57
4.2	Observations and data reduction	58
4.3	Results	61
4.3.1	AFGL 5142	61
4.3.2	DR21 (FIR1 & FIR2)	64
4.3.3	G23.207-00.377	67
4.3.4	G23.389+00.185	70
4.3.5	G23.657-00.127	72
4.3.6	G24.541+00.312	73
4.3.7	G40.62-0.14	74
4.3.8	G73.06+1.80	76
4.3.9	G78.12+3.63	78
4.3.10	L1206	80
4.3.11	S255	82
4.3.12	W3(OH)	85
4.4	Analysis	88
4.4.1	Rotation diagram analysis	88
4.4.2	CH ₃ OH gas distribution	89
4.4.3	Population diagram analysis	91
4.5	Discussion	92
4.5.1	Excitation of CH ₃ OH gas	92
4.5.2	Morphology	94
4.6	Conclusions	94
5	Dynamics of 6.7 GHz methanol masers in high-mass star-forming regions	97
5.1	Introduction	99
5.2	Observations and data reduction	100
5.3	Results	101
5.4	Discussion	104
5.5	Summary	108

Contents

Bibliography	113
Nederlandse Samenvatting	119
Publications	125
Curriculum Vitae	127
Acknowledgements	129

1.1 Star formation

Popular wisdom states that we are all made out of star dust, which to a very large extent is true, as all elements heavier than lithium have been formed in stars and supernovae in some way or another. But we can actually be a bit more specific than that; we are mainly made out of dust from stars more massive than our sun. Because the luminosity of a star depends on its mass $L \propto M^{3.5}$, the heavier the star is the hotter and faster it will burn. A star like our sun has a life expectancy of approximately 10 billion years, and our sun is now a comfortable 4.5 billion years old. As the universe is circa 13.7 billion years old, the material that makes up our sun (and solar system) cannot have had time to pass through a star such as our sun before forming our solar system. Most of the heavy elements around today must have formed in stars with shorter lifetimes and consequently more mass than our sun. In addition to enriching the Galaxy with heavier elements, the massive stars impact their local environment in at least two other ways: through their outflows, winds, and eventual supernovae they inject a large amount of mechanical energy in the interstellar medium (ISM). Furthermore their harsh uv-radiation ionises the environment. Also, when observing the powerful starburst galaxies, most of what we see is the intense radiation from the high-mass stars. All these reasons imply that high-mass stars are very important and understanding their formation is a key piece of the puzzle that makes up our universe (Zinnecker & Yorke 2007, Beuther et al. 2007a).

Most stars form in giant molecular clouds, dense interstellar clouds of tens of thousands to millions of solar masses, where most hydrogen is in the form of H_2 and with typical temperatures of 10 K. Inside the giant molecular clouds are clumps and filaments with the denser material called molecular clumps and dense molecular cores, Fig. 1.1. The cores are supported by the gas pressure (both thermal and non-thermal components) inside, working against the gravitational force. If the mass of the core is greater than the so-called Jeans mass, the internal pressure is not able to support the core and it will start to collapse. Depending on the size of the core and its internal dynamics the core may fragment into smaller cores. Another source of energy that is often ignored in models

1 Introduction

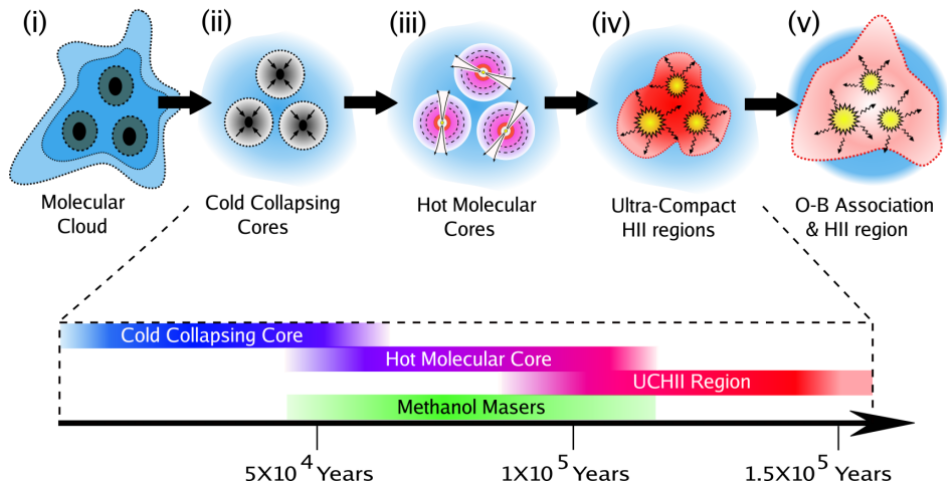


Figure 1.1: A cartoon of the early stages of high-mass star-formation, from molecular cloud to main sequence star. Also outlined are the time scales of the different phases and when the methanol maser emission supposedly occurs. Credit: Cormac Purcell.

of star formation is that of the magnetic fields. On large scales, the magnetic field can help support the cloud against gravitational collapse but also on smaller scales the magnetic field is important in regulating the feedback processes (e.g. Vlemmings et al. 2010). Also turbulence can be important, it affects the fragmentation of the cloud and can on small scales promote collapse. As the core collapses, gravitational energy is released as radiative energy, but the denser the core becomes, the more opaque it will get and when the gravitational energy can no longer be radiated away, the temperature of the core will increase. The protostar in the centre of the core will continue to accrete material and as the temperature increases through released gravitational energy and shocks, the dust in the dense part of the cloud will warm up and start to radiate thermal emission at mm and infra-red wavelengths. At some point the star will turn on and start to burn first deuterium and subsequently hydrogen and the accretion of material onto the star will stop. The star is then said to have reached the main sequence, where stars like our Sun spend billions of years, but massive stars only millions of years. The advent of the star turning on when it is still embedded in its natal core separates in a natural way the high-mass stars from their lower mass equivalents. In a first order approximation one can consider the gravitational collapse as spherically symmetric. In this case, as the star turns on, the radiation pressure will counteract the gravitational force and when the star reaches a mass of eight solar masses radiation pressure overcomes the gravitational force and accretion ceases (Eddington limit). However, stars with masses $> 200 M_{\odot}$ have been observed and so they must be able to form in some manner (Crowther et al. 2010).

While low mass stars can form in relative isolation most stars form in groups or clusters, and many end up as binaries. It seems that more massive stars almost always form in

clusters. The result of the clustered nature of massive star formation are open clusters that consists of tens of stars with combined masses of a few tens to hundreds of solar masses. The most well known example in the northern hemisphere is the Pleiades. The nature of high-mass star-formation has further consequences for observational astronomy. First of all the massive stars form in the densest part of the molecular clouds and they are therefore heavily obscured at optical wavelengths, so we are forced to turn to longer wavelengths, such as infra-red or radio emission. The longer wavelengths suffer from much less attenuation by the dust. Secondly, because of their short lifetimes and rapid evolution massive stars are far and few between. While the nearest low-mass star-forming regions can be found at a distance of ~ 100 pc, the nearest high-mass star-forming region (Orion) is at a distance of 414 pc (Menten et al. 2007), and most regions are found at several kpc. The larger distances to the high-mass star-forming regions imply that the linear sizes become much larger for a given resolution compared with the low mass case. Also, because of the clustered nature of high-mass star-formation confusion is often a problem in that it is difficult to separate the different protostars and disentangle the —often multiple— outflows. All in all, these conditions make the observations of high-mass star-formation particularly challenging.

Several theories of how massive stars form have been proposed (Zinnecker & Yorke 2007, Beuther et al. 2007a). In the coalescence or merger scenario (Bonnell & Bate 2005) individual low- or intermediate-mass protostars merge to form higher mass protostars, requiring very high stellar densities. The two other scenarios, competitive accretion (Bonnell et al. 1998) and monolithic collapse or core accretion (McKee & Tan 2003) differ mainly in how a molecular clump fragments and how the high-mass protostar acquires its mass. In the competitive accretion scenario the clump fragments into low mass cores at an early stage and the individual cores then compete for the remaining unbound gas of the clump. Models have shown that this process has a very high star formation efficiency, and almost all gas is turned into stars. Although feedback processes that likely lower the star formation efficiency have not been included in the models, the observed star formation efficiency is much lower. Today, the most favoured scenario is that of monolithic collapse or core accretion. This scenario is basically an upscaled version of how low mass stars form, a core that has condensed from the larger molecular clump proceeds to evolve without much interaction (mass transfer) with other cores to form one or more stars. In this model it is proposed that a self-shielding, possibly magnetically controlled, accretion disk regulates the accretion beyond the Eddington limit. The stellar mass depends on the initial core mass as more massive cores would form higher mass stars. The result of this scenario is a relatively low star formation efficiency and a core mass function similar to the initial mass function (IMF) of stars, both of which are in good agreement with observations.

1.2 Molecular astrophysics

One of the diagnostics available when exploring the early stages of star formation are the radiative transitions of interstellar molecules. The first molecule to be detected in space was CH in 1937. In the 1960s and 1970s the field of molecular astrophysics really took off

1 Introduction

so that today, a mere 80 years after the discovery of CH, there are almost 170 molecules detected in space (see www.cdms.de for an up-to-date list). In particular, the rotational emission lines observable in the mm and sub-mm regime of the electromagnetic spectrum are valuable tools to explore the cold and dense regions of star formation, as the transitions are easily excited in cold environments and the longer wavelength radiation can penetrate through the dense clouds much more readily than radiation at shorter wavelengths. The spectrum of a molecule is determined by its internal structure and its dipole moment, but more than just identifying the molecule, the relative intensities of the different radiative transitions can be used to determine the physical conditions of the gas. Depending on the structure of the molecule one can constrain the temperature, column density, density and excitation of the gas. Symmetric rotors such as CH₃CN and NH₃ are particularly suitable probes of the temperature as several transitions can be observed within a single bandpass, whereas linear molecules such as CS, HCO⁺, and HCN have traditionally been used as density probes (Evans 1999, van der Tak et al. 2007).

Gas in thermodynamic equilibrium is described by a single temperature, its kinetic temperature (T_k), which determines the energy level populations. However, in many astrophysical environments the conditions are such that the gas is not in thermodynamic equilibrium and therefore there may not be a single temperature that describes the excitation of the gas. The relative population of two energy levels is then described by what is called the excitation temperature (T_{ex}). Whether a particular transition is thermalised or not, depends on the balance of collisional (de-)excitation and the spontaneous emission coefficient (Einstein coefficient A_{ul}) of the particular transition. Therefore there exist for each molecule and transition a critical density for which collisions are more important than radiative processes. This mechanism populates the upper energy level, and the excitation temperature approaches the kinetic temperature. In contrast, in the low density case when collisions are not (or less) important the relative population is determined by the balance between collisional excitation and radiative decay. Also, stimulated absorption and emission can start to play a role, at the very least through the cosmic microwave background $T_{rad} > 2.7$ K. If infrared radiation from warm dust is significant T_{rad} can be greater than T_{ex} (and even T_k), otherwise $T_{rad} < T_{ex} < T_k$.

Another important factor that needs to be considered is the optical depth (τ_ν) of the lines. The optical depth describes the absorption coefficient or the detailed balance of radiative absorption (described by the Einstein coefficient B_{12}) and stimulated emission (Einstein coefficient B_{21}) of the gas. Another, perhaps more intuitive way to looking at the optical depth is as the interaction of the emitted photon with other molecules within a parcel of gas. In the case of optically thin emission the photon emitted by a molecule does not interact with any other molecule before escaping the parcel of gas. On the other hand, if the photon is absorbed by a molecule it will after a certain time be re-emitted in a random direction (isotropically). So, the higher the optical depth the more interactions of absorption and (isotropic) re-emission before the photon escapes the parcel of gas.

To analyse thermal emission from molecules a common assumption is that their excitation follow a Boltzmann distribution so that it can be described by a single temperature. Combined with the assumption that the lines are optically thin and that the emitting region is the same for all lines the temperature and column density of the gas can be determined

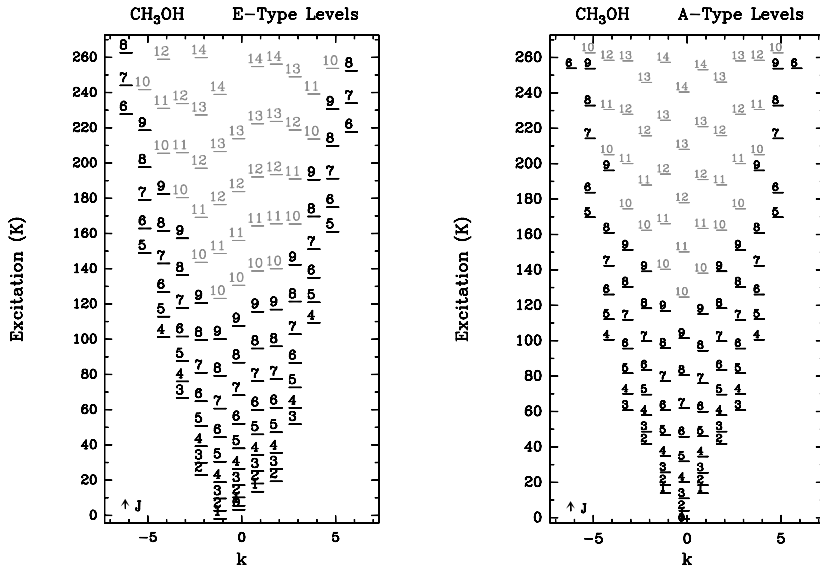


Figure 1.2: Energy level diagram of the CH₃OH E and A species. Credit: Silvia Leurini

by a least square solution to the relative populations of several pairs of the observed energy levels as measured by their respective line strengths, the so called rotation diagram analysis or Boltzmann plot (e.g. Helmich et al. 1994). Although this excitation temperature is not necessarily the same as the kinetic temperature, it provides a measure of the conditions in the gas. The analysis method can be extended to the population diagram method by including corrections for a finite optical depth and source size (Goldsmith & Langer 1999).

During the early stages of star formation a rich chemistry occurs, both in the solid phase in the icy mantles of dust grains, and in the gas phase (for a review, see van Dishoeck & Blake 1998). Also, complex molecules with ten and more atoms have been identified (Herbst & van Dishoeck 2009). The focus of this thesis is the CH₃OH (methanol) molecule and I will therefore limit the discussion to that species. CH₃OH was first discovered in the ISM in 1970 (Ball et al. 1970) and it was soon realised that the observed abundances could not be explained by gas phase chemistry only as the yields are too low. Subsequent studies have shown that the CH₃OH molecules are formed in the icy mantles of interstellar dust grains by hydrogenation of CO molecules at temperatures of ~ 10 K (e.g. Fuchs et al. 2009). As the young protostellar object evolves and warms up its environment the CH₃OH molecules sublime from the dust grains into the gas phase at ~ 100 K (Collings et al. 2004). The CH₃OH molecule can be a great tool to explore the conditions of protostellar objects and their environments, if care is taken when selecting which transitions to study. It has closely spaced energy levels covering a wide

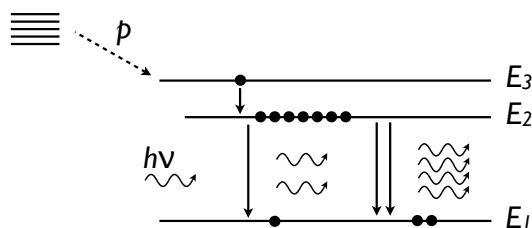


Figure 1.3: Schematic view of how maser emission occur. A pumping mechanism (p) supply the excitation to an energy state E_3 and the molecule then relaxes into the E_2 state. A photon with the correct energy can then stimulate the emission of a second identical photon.

range of excitation temperatures, Fig. 1.2. Due to its slight asymmetry it can serve as a probe of both the temperature and the density of the environment (Leurini et al. 2004). There are two distinct species of CH_3OH , A- and E type, determined by the symmetry of the molecule. Conversion between these two symmetry states is slow and for radiative transfer applications the two species can be treated as two separate molecules.

1.3 Masers

Microwave amplification by stimulated emission of radiation, or maser in short, is the equivalent of the laser for optical light, the difference being the longer wavelength of the microwave radiation. For maser action to occur in space requires at least three conditions to be met: the gas must be out of thermal equilibrium and a population inversion of the energy states must occur so that a higher energy state is over-populated, a seed photon of the wavelength corresponding to the maser frequency must be available, and sufficient amplification path length is needed (for a review, see Elitzur 1992). Affecting these criteria are several factors. First of all, the density must be below the critical density of the transition or the maser will be quenched by collisional de-excitation. Secondly, a pumping mechanism is required to sustain the population inversion, and depending on the type of maser, this can be either collisional or radiative pumping. To illustrate maser action consider a gas cloud made up of a molecular species with only three energy levels. In a simple three energy level system, $E_1 < E_2 < E_3$, the pumping mechanism would excite the molecules from the lower state E_1 to the higher energy state E_3 through (stimulated) absorption or collisional excitation. The molecule then relaxes into the E_2 state. Now, if the “half life” of the E_2 state is long compared to the pumping mechanism and the half life of E_3 , more and more molecules will populate the E_2 energy state. A population inversion occurs with more molecules in the E_2 state than in the E_1 state. A seed photon with an energy $h\nu = E_2 - E_1$ passing through our imaginary gas cloud can then interact with a molecule in the excited E_2 state and stimulate the emission of a second photon. This second photon will be coherent to the first photon, meaning that it will have the same

frequency, travel on the same direction and also have the same phase. These two photons can then stimulate the emission of two more photons and so on. The result is a shower of photons, coherent emission with the same direction, frequency, phase, and polarisation as the original seed photon. Another way to look at this is through the same analogy as with the optical depth above, but in this case a negative optical depth. So, when a photon of the energy $h\nu = E_2 - E_1$ interacts with a molecule in the excited E_2 state it is not absorbed but rather stimulates the emission of a second coherent photon. Maser emission is then the result of an exponential growth of interactions with molecules in the excited state.

Astronomical masers are made up of a large number of “individual” coherent masers and what we observe with our radio telescope is the emission resulting from an ensemble of masers, and therefore not necessarily coherent emission. Another consequence of the multiple masers is that they compete for the molecules in the excited state. So, if there is a preferred direction, such as a longer path length and/or a source of seed photons the individual masers along this direction will be preferential and depopulate the excited energy state so that maser emission in other directions will not be possible or at least much weaker. Such emission is said to be beamed. The path length of the maser then determines the maser intensity. The path length is determined by the length along the maser path through the gas cloud with a population inversion, but also with a velocity gradient smaller than the line width of the maser. Moreover, exponential amplification can only continue as long as the pumping mechanism can sustain the population inversion, when this is no longer possible the maser becomes saturated and the intensity no longer increases exponentially, but rather linearly with the path length.

The same CH_3OH molecules, when released to the gas phase, can also support bright maser emission, especially at the low energy cm transitions. The CH_3OH masers are divided into two different classes of spectral lines dependent on the pumping mechanism. Class I CH_3OH masers are supposedly collisionally pumped (Cragg et al. 1992). They are often observed in outflows of proto-stellar objects (Menten 1991a). In contrast, the class II CH_3OH masers are supposedly pumped by IR radiation (Sobolev & Deguchi 1994, Sobolev et al. 1997, Cragg et al. 2005) and are associated with the early stages of high-mass star-formation (Menten 1991a). In particular the 6.7 GHz CH_3OH masers, discovered as late as 1991 (Menten 1991b), have been found to be only associated with high-mass star-formation (Minier et al. 2003, Xu et al. 2008). But, more than just signposts of high-mass star formation, the high brightness temperatures of (CH_3OH) masers allows detailed high angular resolution studies with VLBI techniques (e.g. Norris et al. 1998) which can be used to determine their parallax (e.g. Reid et al. 2009a), internal motions, velocity fields, and even magnetic fields (Vlemmings et al. 2010). There is a still ongoing debate as to what physical structures the CH_3OH maser emission is associated with, in particular outflows and circumstellar disks are two of the main candidates (e.g. Minier et al. 2000, De Buizer 2003). A recent high-resolution study of 30 sources has revealed that $\sim 30\%$ have an elliptical distribution, suggesting a driving source in the centre (Bartkiewicz et al. 2009).

1.4 Radio interferometry

The resolution of a single dish telescope is limited to $1.2 \times \lambda/D$ radians, where λ is the wavelength, and D the diameter of the telescope. For example, the resolution of a 30-m telescope at a wavelength of 3 mm is $25''$. Studying objects at much higher resolution would require the construction of antennas with diameters of several 100 m, which is impossible. An alternative way to increase the resolution of radio frequency observations is to combine the signal from several telescopes and so synthesise a much larger telescope. This technique is known as interferometry, and by combining the signals of multiple telescopes the resolution is no longer limited by the diameter of the telescopes but rather the distance or projected baseline between the telescopes. In most interferometers the signals from several telescopes are combined and the instrument then becomes sensitive to emission that occurs on size scales between that corresponding to the minimum and the maximum baselines. Emission on large size scales is filtered out by the lack of short baselines and the maximum resolving power is limited by the longest baselines. The increase in resolution does however come at a price: although the sensitivity of the individual telescopes has not changed, the size of the emitting region has been dramatically reduced as the lack of short baselines filter out emission on larger size scales, and so the equivalent brightness temperature of the object must be much greater to be detected. In particular, for Very Long Baseline Interferometry (VLBI), non-thermal emission processes are required to produce high enough brightness temperatures $>10^6$ K to be detected (Thompson et al. 2001). What an interferometer does, is to sample the Fourier transform of the sky brightness distribution at the points in the $u - v$ (spatial frequency) plane determined by the baselines between antenna pairs. Limitations in the number of antennas and the available observing time lead inevitably to gaps in the sampling of the $u - v$ plane. In reality, through clever calibration techniques and by using an iterative deconvolution algorithm in combination with other image constraints one can reconstruct a model of the sky brightness distribution from the limited data points measured by the interferometer.

1.5 This thesis

The goal of this thesis is to study the relation between the 6.7 GHz maser emission, the protostar(s) responsible for the enhanced excitation and the thermal CH_3OH emission. Specific goals are to see whether we can determine where the CH_3OH maser emission arises in relation to the protostar and what the excitation conditions of the masing gas are. To do this we study a sample of 14 CH_3OH maser sources at different wavelengths and through different emission mechanisms. The sample contains some of the most nearby high-mass star-forming regions and was originally selected based on their close distances and infrared colour. Included in the sample are also three sources selected from the Toruń blind sample (Szymczak et al. 2000) for which high-resolution VLBI observations of the CH_3OH maser emission exists.

In Chapter 2 we present the results of European VLBI network (EVN) and very long baseline array (VLBA) observations of the 6.7 and 12.2 GHz CH_3OH maser emission

towards Cepheus A HW2 (Cep A). In this chapter we also describe in some detail the calibration process used for all the VLBI data reduction. At a distance of 700 pc Cep A is the closest source in our sample, and one of the most well studied. The CH₃OH masers are distributed in a filamentary arc shape in the equatorial region of the protostar, perpendicular to the thermal jet observed at radio continuum wavelengths. The velocities of the individual maser spots suggest that infall is the dominant motion rather than rotation, although the multi-epoch observations do not show any significant motion of the maser spots. We argue that the CH₃OH masers occur close to, or in, a shock interface, between the actual accretion disk and the surrounding envelope of infalling material, a picture that fits with earlier polarisation measurements (Vlemmings et al. 2010).

The thermal CH₃OH observations of Cep A are presented in Chapter 3. The observations were performed with the HARP instrument, a heterodyne mixer with 16 pixels working at 345 GHz mounted on the 15 m James Clerk Maxwell Telescope (JCMT). We use this instrument to map the large scale distribution and excitation of the CH₃OH gas. The gas extends over 46'' (0.16 pc) and a linear velocity gradient along the major axis suggests that the gas is entrained in an outflow. The large scale CH₃OH distribution has a low excitation with only a few lines detected at our sensitivity and temperatures of ~50 K. In contrast, at the position of the HW2 protostar a second gas component is seen at a velocity similar to that of the maser emission. This second gas component is much more readily seen in the highly excited lines than in the lower excited lines. Whether this is due to optical depth effects or a population inversion, in either case it is clear that the second gas component is much more highly excited.

The same observational technique and methodology used in Chapter 3 has been applied to a sample of 13 sources associated with 6.7 GHz CH₃OH maser emission in Chapter 4. For eight of the sources in our sample (including Cep A) we characterise the thermal CH₃OH emission as compact. Four of the remaining sources have more extended thermal CH₃OH emission and more complex velocity fields, and in the last two sources the emission was too weak to be mapped. The compact sources all have a single peak in the intensity maps, close to the position of the CH₃OH maser emission. Furthermore, they have linear velocity gradients along the maser axis which we interpret as gas being entrained in an outflow. Also, in the rotation diagram analysis we find the highest rotation temperatures close to the maser emission. Although, in general, we do not detect many high- K lines, the detection of the $v_t = 1$ line towards half of the sources indicate the presence of highly excited gas. The population diagram analysis of the thermal CH₃OH emission at the position of the maser emission indicates that the optical depth of the lower- K lines is moderate. It is likely that the beam dilution is too large for the JCMT to probe the highly excited gas.

In Chapter 5, we present the results of a VLBI study of the 6.7 GHz CH₃OH maser emission towards the sources identified in Chapter 4 as having compact thermal CH₃OH emission. We have mapped the CH₃OH maser distribution towards three of the sources and include VLBI data on the maser distribution from the literature for an additional four compact sources. Although the VLBI observations typically only recover a fraction of the flux as measured by single dish observations, all spectral features in the single dish data can be recognised in the VLBI spectra. We therefore conclude that although the maser

1 Introduction

spots may be embedded in more extended emission, they still represent the entire physical structure. The maser spot distributions have extents of a few hundred to a couple of thousands of AU, in good agreement with what has been found in other studies. Furthermore, in three of the sources the masers appear to delineate, or be part of, a disk/torus in the equatorial region of the massive young stellar object (MYSO). The orientation of the disk/torus is perpendicular to the thermal CH₃OH emission observed in Chapter 4, supporting the argument that the thermal emission is entrained in an outflow. With the advent of ALMA it will be possible to probe the thermal gas on size scales similar to the maser emission for statistically significant samples of high-mass star-forming objects.

1.6 Main conclusions

We have found that for a fair fraction of the sources the methanol masers appear on size scales of ca. 1000 AU, in the equatorial region of the massive protostar. It appears that infall, rather than rotation, is the dominant motion. We propose that the maser emission occur close to or in a shock interface, possibly related to the accretion flow of the more extended gas in the protostellar envelope onto an accretion disk. The morphology and kinematics of the thermal CH₃OH gas support the hypothesis that the maser region is also the region where the CH₃OH molecules are released from the icy mantles of the dust grains. We have also estimated the temperature and column density of the CH₃OH gas in the outflows and find evidence for radiative excitation of the CH₃OH gas at the location of the maser emission. Our main findings are listed below.

- We detect thermal CH₃OH emission in all 6.7 GHz CH₃OH maser sources observed with the JCMT and in all but two of the sources we have been able to map the CH₃OH gas distribution and excitation.
- Half of the 6.7 GHz CH₃OH maser sources have compact thermal CH₃OH emission with a single peak in the integrated line flux maps. In these sources the thermal CH₃OH emission is centred close to the position of the CH₃OH maser emission.
- Several of the sources appear to have linear velocity gradients along the major axis of the CH₃OH emission suggesting that the CH₃OH gas is entrained in an outflow.
- The 6.7 GHz CH₃OH maser emission in half of the eight imaged sources is distributed in a disk/torus interface in the equatorial region of the massive protostars. The velocity field suggests that infall rather than rotation is the dominant motion.
- The disk/torus interface delineated by the maser emission appears to be oriented roughly perpendicular to the larger scale thermal CH₃OH emission of the envelope, supporting our argument that the thermal gas is entrained in an outflow.
- The detection of the CH₃OH $J = 7 - 6 \nu_1 = 1$ line at 337.9 GHz in seven of the 14 sources indicates that radiative excitation is important at least in these sources.

However, the general lack of detection of high- K lines and consequently low rotation temperatures may be due to beam dilution if the region of highly excited gas is of comparable size as that of the maser emitting region, a few hundred to a couple of thousand AU.

1.7 Future prospects and outlook

The 6.7 GHz CH_3OH maser is an excellent signpost of the early stages of high-mass star-formation. Moreover the CH_3OH masers can be used to study these environments at very high angular resolution. Also, the specific conditions required for maser emission should tell us something about the physics of these sources. With this thesis we have a working hypothesis for a fraction of the maser sources. However, we still do not understand exactly which physical structures the maser emission trace in the remaining sources. It is also unclear whether the masers trace a mass range, a specific evolutionary stage or possibly both. There are several pathways to explore why, how and where maser emission occurs. In the following we will outline a few routes that seem particularly interesting given the recent upgrade and construction of new instruments with unique capabilities.

The 6.7 GHz CH_3OH maser does not seem to be associated with ultra-compact HII (UCHII) regions in general, as in most cases no radio continuum arising from free-free emission is detected towards the sources associated with masers. However, there may exist an earlier stage, a so called hyper-compact HII region in which the HII region is gravitationally trapped and the free-free emission optically thick also at millimetre wavelengths (Keto 2003). An optically thick HII region has a rising spectrum $S_\nu \propto \nu^2$ up to the turn-over frequency at which the region becomes optically thin. Because of the rising spectrum these regions are more readily detectable at higher frequencies (20-40 GHz). With the recent bandwidth upgrade of the eVLA from 172 MHz to 8 GHz the instrument has become seven times more sensitive and observations of large samples of CH_3OH masers are now possible. High resolution and astrometric accurate positions of the radio continuum is important to determine where the CH_3OH maser occurs in relation to the protostar(s) that are forming. Also, in the next few years, the SKA pathfinder MeerKAT promises to be a valuable tool to determine the association of HCHII regions and CH_3OH (12 GHz) masers in the southern hemisphere .

Mapping the thermal emission of molecular lines at high resolution towards more than a small handful of high-mass star-forming regions has up to now been impossible. The instruments capable of such observations such as the SMA and PdBI have not had the sensitivity to afford us to map larger samples of sources. With the advent of ALMA, a 66 dish interferometer built in the Atacama desert (Chile) at 5000 m altitude, this is changing dramatically. The high sensitivity combined with the high resolution capability of ALMA means that the thermal molecular line emission can be mapped on size scales comparable to that of the CH_3OH maser emission for statistically significant samples. If the CH_3OH maser emission arises in a disk or torus interface it will be possible to map and determine the excitation of the gas associated with the maser emission, and how it compares to the gas in the outflows and envelope.

1 Introduction

Also, with continuing efforts of VLBI observations of CH₃OH masers of larger samples much can still be learned. Polarimetry allows us to probe the magnetic field on small scales close to the protostar but has only been done towards a couple of sources. With temporal monitoring and simultaneous observations of the radio continuum much more can be learned about the maser variability and apparent periodicity observed in some sources (Szymczak et al. 2011), in particular whether it is due to changes in the pumping of the maser or to intrinsic variability of the background source. Finally, through ongoing VLBI monitoring programmes, the parallax towards a significant number of high-mass star-forming regions have been measured. Not only does this provide an important independent distance determination to these regions, but it also gives important insights into the systematic motions within our Galaxy.

Dynamics of the 6.7 and 12.2 GHz methanol masers around Cepheus A HW2¹

Abstract

The 6.7 GHz methanol maser is exclusively associated with high-mass star formation. However, it remains unclear what structures harbour the methanol masers. Cepheus A is one of the closest regions of massive star formation, making it an excellent candidate for detailed studies. We determine the dynamics of maser spots in the high-mass star-forming region Cepheus A in order to infer where and when the maser emission occurs. Very long baseline interferometry (VLBI) observations of the 6.7 and 12.2 GHz methanol masers allows for mapping their spatial and velocity distribution. Phase-referencing is used to determine the astrometric positions of the maser emission, and multi-epoch observations can reveal 3D motions. The 6.7 GHz methanol masers are found in a filamentary structure over ~ 1350 AU, straddling the waist of the radio jet HW2. The positions agree well with previous observations of both the 6.7 and 12.2 GHz methanol masers. The velocity field of the maser spots does not show any sign of rotation, but is instead consistent with an infall signature. The 12.2 GHz methanol masers are closely associated with the 6.7 GHz methanol masers, and the parallax that we derive confirms previous measurements. We show that the methanol maser emission very likely arises in a shock interface in the equatorial region of Cepheus A HW2 and presents a model in which the maser emission occurs between the infalling gas and the accretion disk/process.

¹Based on: Karl J. E. Torstensson, Huib Jan van Langevelde, Wouter H. T. Vlemmings, Stephen Bourke, 2011, A&A, 526, 38

2.1 Introduction

Methanol masers are signposts of high-mass star formation. Continuum emission of warm dust at sub-millimetre wavelengths has been detected at well over 95% of the observed 6.7 GHz methanol maser sites (Hill et al. 2005), even though only some of the masers are associated with detectable ultra-compact (UC) H_{II} regions. This seems to indicate that the methanol masers probe a range of early phases of massive star formation and that they disappear as the UC H_{II} region evolves (Walsh et al. 1998). More than just signposts, masers are tracers of the geometry and small-scale dynamics in these regions. Much effort has focused on studying the kinematics, and several claims of circumstellar disks, expanding spherical shells, and jets have been made (e.g. Norris et al. 1998, Pestalozzi et al. 2004, Minier et al. 2002, Bartkiewicz et al. 2005b). The evidence suggests that masers trace an evolutionary sequence or possibly a mass range in the formation process, or perhaps even both (Walsh et al. 2001).

The star-forming region Cepheus A East (hereafter Cep A) is one of the closest high-mass star-forming regions at a distance of 700 pc, as determined by parallax measurements of methanol masers (Moscadelli et al. 2009, hereafter Mos09). The region has a total bolometric luminosity of $2.5 \times 10^4 L_{\odot}$ (Evans et al. 1981), and its appearance in the radio is dominated by the thermal jet Cep A HW2 (Hughes & Wouterloot 1984). A central object has been identified that is believed to be the source driving the jet. On small scales ($\sim 1''$), the thermal jet shows outflow velocities in excess of 500 km s^{-1} (Curiel et al. 2006). Also on larger scales ($\sim 1'$), a bipolar molecular outflow with blueshifted gas in the NE and redshifted gas in the SW is seen in HCO⁺ (Gómez et al. 1999). Recent sub-millimetre observations have shown an elongated disk structure (Patel et al. 2005, Torrelles et al. 2007) at the position of the 7 mm continuum object identified by Curiel et al. (2006). Although there are multiple sources within the inner $1''$, the central object (HW2) with a mass of $\sim 18 M_{\odot}$ is believed to be the main driving source in the region (Jiménez-Serra et al. 2009).

Maser observations of HW2 have shown a complex structure in hydroxyl (Bartkiewicz et al. 2005a), water (Vlemmings et al. 2006), and 12 GHz methanol masers (Minier et al. 2001, hereafter Min01). Recent multi-epoch observations of water masers in the region indicate the presence of a slower wide-angle outflow in addition to the high-velocity collimated jet observed in radio continuum (Torrelles et al. 2010). Sugiyama et al. (2008b) find the 6.7 GHz methanol maser emission to be constrained to two individual clumps with blueshifted masers to the east and redshifted masers in a linear configuration to the west. Moreover, single-dish monitoring of the 6.7 GHz methanol masers has shown the variation in the maser emission in the blueshifted and redshifted cluster to be synchronised and anti-correlated (Sugiyama et al. 2008a). Maser polarisation observations indicate a strong ($|B| \sim 23 \text{ mG}$) magnetic field in the 6.7 GHz methanol maser region that is aligned with the thermal jet of the protostar HW2 (Vlemmings 2008, Vlemmings et al. 2010). Similarly to the molecular and dust disk, the methanol masers are aligned perpendicular to the thermal jet and magnetic field although at a larger radius. The inferred high accretion rate (McKee & Tan 2003) is likely regulated and sustained by the large-scale magnetic field.

We carried out large field of view European VLBI Network¹ (EVN) observations of the 6.7 GHz and Very Long Baseline Array (VLBA), operated by the National Radio Astronomy Observatory² (NRAO), observations of the 12.2 GHz methanol masers in Cep A East to determine the morphology and relationship between the 6.7 GHz and 12.2 GHz methanol masers. In Sec. 2.2 the observations and data reduction process is described. We report our results in Sec. 2.3, and extend the analysis to a simple geometric model in Sec. 2.4. The implications of our model and how it can be tested are discussed in Sec. 2.5, and finally our conclusions are presented in Sec. 2.6.

2.2 Observations and data reduction

2.2.1 6.7 GHz data

The 6.7 GHz methanol maser observations of Cep A were carried out with the EVN in November 2004 as a part of a larger project (EL032) with 12 sources in total. The eight telescopes of the EVN participating in the experiment were Medicina, Onsala, Toruń, Cambridge, Darnhall, Noto, Effelsberg and Westerbork. In order to achieve astrometric positions all the observations were done in phase referenced mode. For Cep A the calibrator J2302+6405 (with a separation of $\sim 2.2^\circ$) was used as the phase reference source. Cep A was observed for a total of ~ 2 h including the phase calibrator and four scans on the amplitude and bandpass calibrators 3C345 and DA193. In Table 2.1 we list the coordinates used for the calibrators and the phase centre of the observations. In order to improve the uv-coverage the observation was split into two ~ 1 h blocks. Unfortunately, due to scheduling constraints, these two blocks are for Cep A separated by ~ 12 h, resulting in a less than ideal uv-coverage. The experiment was set up at a rest frequency of 6668.5142 MHz, with 1024 channels and with RCP and LCP recorded separately. The total bandwidth was 2 MHz, resulting in a velocity resolution of 0.088 km s^{-1} , and a total velocity coverage of 90 km s^{-1} centred at LSR -3 km s^{-1} .

The data was correlated on the EVN correlator at JIVE with an integration time of 0.25 s. The short integration time was chosen to maximise the field of view (FOV) of the observations to enable a search for maser emission in a large field.

Several telescopes show internally generated RFI in the auto-correlated data. The strongest of these components exhibit Gibb's ringing, indicating that it is a very narrow-band signal. None of this internally generated RFI does however show in the cross-correlated data and is therefore not cause for any concern in the cross-correlation calibration.

All editing, calibration and imaging was done in AIPS³. The calibrators 3C345 and DA193, observed at the beginning and end of each 1 h block, were used for amplitude

¹The European VLBI Network is a joint facility of European, Chinese, South African and other radio astronomy institutes funded by their national research councils.

²The National Radio Astronomy Observatory is a facility of the National Science Foundation operated under cooperative agreement by Associated Universities, Inc.

³Astronomical Image Processing System, developed and maintained by the NRAO.

2 Dynamics of the methanol masers around Cepheus A HW2

Table 2.1: Coordinates of science target and calibrators for the 6.7 GHz (EVN) and 12.2 GHz (VLBA) observations.

Source	RA(J2000)	Dec(J2000)
Cep A (HW2)	22 56 17.9000	+62 01 50.000
J2302+6405	23 02 41.315001	+64 05 52.84853
3C345	16 42 58.809968	+39 48 36.99400
DA193	05 55 30.805614	+39 48 49.1650
Cep A (HW2)	22 56 18.104	+62 01 49.419
J2232+6249	22 32 22.8655	+62 49 36.436
J2302+6405	23 02 41.315001	+64 05 52.84853
J2202+4216	22 02 43.291372	+42 16 39.97992

Notes: The top panel shows the calibrators and coordinates used for the 6.7 GHz observations conducted on Nov 6, 2004 with the EVN. The bottom panel displays the calibrators and coordinates of the 12.2 GHz observations carried out on 2006 March 3, June 2 and September 13, and 2007 January 28 with the VLBA.

and bandpass calibration of each respective block. RCP and LCP data was edited and calibrated separately before combining them in the final image cube. During each 1 h block, eight cycles of Cep A and J2302+6405 were observed with an integration time of 3 and 2 min, respectively. After initial self calibration on J2302+6405 the phase solutions were transferred to the Cep A data. The brightest maser feature was subsequently imaged to determine its absolute position after which it was used for further self calibration. After the final calibration had been applied a cleaned image cube was created for the central 64 channels for which maser emission could be seen in the channel spectra. The final images with a size of $2'' \times 2''$ and a pixel size 1 mas have an rms of 7 mJy beam^{-1} in the line-free channels and 60 mJy beam^{-1} in the channels with the brightest maser emission.

In our analysis we are mostly interested in the relative astrometry with respect to the nearby (2.2°) phase calibrator. The accuracy of this will be limited mostly by the signal-to-noise of the maser and the atmospheric conditions, for which we have not done any specific calibration. Based on the analysis by Rygl et al. (2010) we estimate the accuracy to be 0.3 mas in right ascension and somewhat worse in declination. The absolute astrometry has an additional component from the accuracy of the calibrator position and may be slightly larger than 1 mas. The amplitude calibration we estimate to be accurate to $\sim 30\%$ and the final image has a dynamic range of ~ 1200 in the channel with the brightest emission.

Additionally, we searched a much larger area for new methanol masers. The large field search was implemented using ParstelTongue (Kettenis et al. 2006) in which the field was split up in facets (Bourke et al. 2006). Each of the 4669 boxes corresponds to a data cube of dimensions 2048×2048 cells with a pixel size of 1 mas and 1024 frequency channels giving a total image size of over 18 terapixels (~ 2.5 arcmin diameter). This covers the half power beam width (HPBW) of baselines consisting of Effelsberg and one of the 32m

dishes. The correlation parameters allow for imaging an area three times the beam size but sensitivity drops substantially as Effelsberg’s contribution reduces.

2.2.2 12.2 GHz data

The multi-epoch VLBA observations of the 12.2 GHz methanol masers were performed on the dates as listed in Table 2.1 (project BV059 A, B, C, D). All ten antennas of the VLBA participated in all epochs of the experiment. Each epoch consisted of a total of 5 h observing time. The receivers were setup to record two 0.5 MHz bands with 128 channels each, centred on the rest frequency of the maser line (12178.595 MHz), and one 4 MHz band on either side for the wide-band calibration. For each epoch the observing time was split up in two blocks in which during the first ~ 1.5 h fast switching was done between Cep A and two phase reference sources to ensure accurate astrometric positions. The two sources used for phase referencing were J2232+6249 (2.9° East) and J2302+6405 (2.2° North) of Cep A and the switching sequence used was J2232+6249 - Cep A - J2302+6405 with 40 s spent on each source. During the second block Cep A was observed in four 31 min “stares”, with each stare preceded by a 9 min observation of the bright calibrator J2202+4216 (BL Lac). The channel separation of 3.91 kHz for the narrow band data results in a velocity resolution of 0.96 km s^{-1} . Both RCP and LCP were recorded. The data were correlated at the VLBA correlator in Socorro with an integration time of 2 s.

The initial calibration of amplitude, bandpass and delay was done on J2202+4216 using standard AIPS procedures. The phase calibrators J2232+6249 and J2302+6405 were not bright enough to image directly and therefore reverse phase referencing was done on the brightest maser channel. Because the data was taken in a mixed bandwidth setup and full polarisation, a complex phase transfer scheme was implemented in ParselTongue (Kettenis et al. 2006) that extrapolates the phase and phase rate solutions from the maser channels to the bracketing continuum bands. This way both calibrators could be mapped in all epochs. The offset of the two phase reference sources was determined and applied to the Cep A results. Average offsets were $\Delta\alpha = 34.48 \text{ mas}$ and $\Delta\delta = 67.87 \text{ mas}$ for J2232+6249, and $\Delta\alpha = 49.52 \text{ mas}$ and $\Delta\delta = 23.25 \text{ mas}$ for J2302+6405. The brightest maser features were fitted with a beam size of $3.5 \times 1.5 \text{ mas}$. Typical jmfitt errors are 0.15 mas in right ascension and 0.1 mas in declination. However, the maser sources are quite elongated in right ascension (6 mas half power beam width vs 2.5 in declination) and taking into account the signal-to-noise of the calibrators and phase transfer effects we estimate the positional uncertainty relative to the calibrator to be $\sim 1 \text{ mas}$ in right ascension and $\sim 0.2 \text{ mas}$ in declination.

2.3 Results

2.3.1 6.7 GHz results

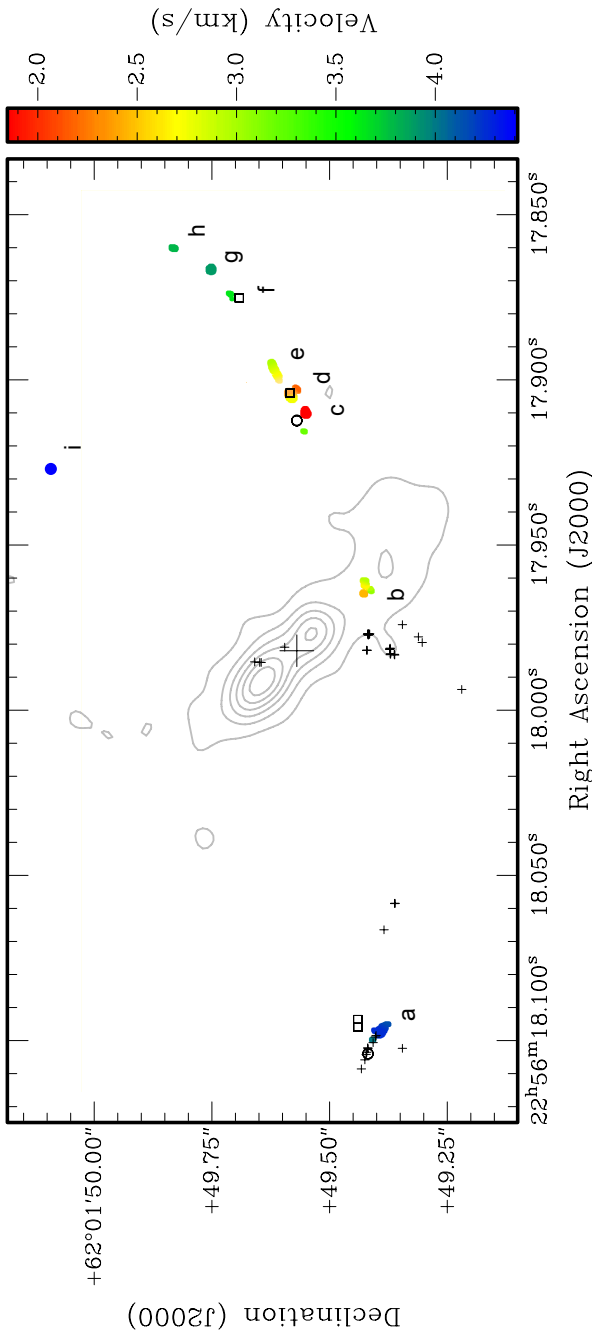


Figure 2.1: The velocity field of the 6.7 GHz methanol masers as obtained from a first moment map of the bright methanol emission (colour) with labels *a-i* overlaid on K band continuum (contours) (Torrelles et al. 1998). The point indicating the weak feature *i* has been added to the moment map manually based on the results of detailed fitting of each channel. Also shown are the 12.2 GHz methanol masers (circles) in this chapter and (boxes) Min01, and 22 GHz water masers (small pluses) (Vlemmings et al. 2006). The position of the protostar is indicated by the large plus sign (Curiel et al. 2006).

The 6.7 GHz methanol maser emission in Cep A originates in an extended $\sim 1.9''$ (1350 AU) filamentary, arc-like structure, straddling the waist of the radio-jet HW2 (Fig. 2.1). No other emission regions were found in the larger search.

The maser emission arises in nine elongated maser clumps separated spatially and/or in velocity. Their coordinates and LSR velocities are presented in Table 2.2 (individual maser spots are listed in Table 2.3). The individual maser features are elongated in the direction of the overall structure, strongly suggesting that the methanol maser in Cep A is originating in one large scale structure.

There is a small velocity gradient of $\sim 2.5 \times 10^{-3} \text{ km s}^{-1} \text{ AU}^{-1}$ across the whole structure with higher velocities towards the centre. One maser feature (resolved into a few small spots) appears projected against the thermal jet seen in the radio continuum, see Fig. 2.1. Its position is not coincident with the 7 mm continuum object identified by Curiel et al. (2006), who claim this to be the driving source in HW2. Rather, the maser feature is seen further to the SW along the axis of the jet. In Fig. 2.2 we show the total measured 6.7 GHz methanol maser spectrum and the measured MERLIN spectrum scaled down by a factor of five (Vlemmings et al. 2010), also indicated are the individual spectra of the eight identified maser features. The emission is constrained to the velocity interval -1.5 km s^{-1} and -4.5 km s^{-1} . The morphology and velocity field that we find of the 6.7 GHz methanol masers agree well with previous measurements using different telescopes: Vlemmings et al. (2010) (MERLIN); Sugiyama et al. (2007, 2008b,a) (VERA). One notable difference between our spectrum and earlier measurements is the lack of a feature at $\sim -4.6 \text{ km s}^{-1}$ as seen by both Vlemmings et al. (2010) and Sugiyama et al. (2008a). The missing feature corresponds to a clump of masers to the NNE of the brightest maser feature (*d*). The missing maser spots are not bright enough to be seen in the spectrum or directly in the moment map. However, when imaging the cube channel by channel we were able to detect the faint emission and have included the feature *i* in Fig. 2.1. In Fig. 2.4 these spots are more clearly visible.

Table 2.2: The absolute positions and LSR velocities of the centroids of the brightest 6.7 GHz methanol maser features measured using EVN.

ID	RA (J2000) 22:56:	Dec (J2000) 62:01:	v_{LSR} [km s^{-1}]	Min01 designation
a	18.09648	49.4049	-4.14	A
b	17.96204	49.4369	-2.56	
c	17.91032	49.5553	-1.68	
d	17.90515	49.5843	-2.47	B
e	17.89870	49.6124	-2.56	
f	17.87421	49.7063	-3.44	C
g	17.86687	49.7442	-3.70	
h	17.86038	49.8191	-3.61	
i	17.92729	50.0863	-4.58	

2 Dynamics of the methanol masers around Cepheus A HW2

Table 2.3: The absolute positions, LSR velocities, and fluxes of the centroids of all 6.7 GHz methanol maser spots measured using EVN.

RA (J2000)	DEC (J2000)	v_{LSR} [km s^{-1}]	I_{peak} [Jy beam^{-1}]	F [Jy]
22:56:17.91048	62:01:49.5551	-1.51	0.5	0.9
22:56:17.91041	62:01:49.5552	-1.60	3.2	5.9
22:56:17.91032	62:01:49.5553	-1.68	6.6	12.8
22:56:17.91022	62:01:49.5552	-1.77	5.9	12.8
22:56:17.91009	62:01:49.5551	-1.86	2.6	6.4
22:56:17.96341	62:01:49.4451	-1.95	0.3	0.4
22:56:17.90334	62:01:49.5723	-1.95	0.6	1.3
22:56:17.91007	62:01:49.5546	-1.95	0.5	0.9
22:56:17.90439	62:01:49.5862	-2.03	2.6	4.1
22:56:17.96453	62:01:49.4402	-2.03	0.4	0.5
22:56:17.90438	62:01:49.5862	-2.03	2.6	4.1
22:56:17.96457	62:01:49.4401	-2.12	0.8	0.8
22:56:17.90441	62:01:49.5867	-2.12	8.7	14.7
22:56:17.96460	62:01:49.4400	-2.21	1.2	1.4
22:56:17.90447	62:01:49.5867	-2.21	16.1	26.4
22:56:17.96462	62:01:49.4398	-2.30	1.9	2.2
22:56:17.90457	62:01:49.5865	-2.30	19.5	31.3
22:56:17.96464	62:01:49.4397	-2.39	2.0	2.1
22:56:17.90485	62:01:49.5854	-2.39	20.4	35.4
22:56:17.96210	62:01:49.4376	-2.47	1.7	2.3
22:56:17.89923	62:01:49.6113	-2.47	1.4	5.8
22:56:17.90515	62:01:49.5843	-2.47	28.9	44.0
22:56:17.96204	62:01:49.4369	-2.56	2.5	3.8
22:56:17.89716	62:01:49.6178	-2.56	2.5	5.7
22:56:17.89870	62:01:49.6124	-2.56	3.8	9.8
22:56:17.90530	62:01:49.5840	-2.56	27.6	39.4
22:56:17.96174	62:01:49.4369	-2.65	1.3	4.7
22:56:17.90541	62:01:49.5839	-2.65	13.3	18.6
22:56:17.89862	62:01:49.6124	-2.65	3.0	6.3
22:56:17.89690	62:01:49.6186	-2.65	3.4	12.0
22:56:17.96084	62:01:49.4379	-2.74	2.2	2.8
22:56:17.90552	62:01:49.5839	-2.74	3.2	4.5
22:56:17.89637	62:01:49.6200	-2.74	2.4	10.7
22:56:17.96348	62:01:49.4266	-2.82	0.8	2.4
22:56:17.96083	62:01:49.4371	-2.82	2.0	2.6
22:56:17.90566	62:01:49.5838	-2.82	0.6	0.9
22:56:17.89593	62:01:49.6215	-2.82	1.1	4.8
22:56:17.89533	62:01:49.6224	-2.82	1.4	3.7

Table 2.3: Continued.

RA (J2000)	DEC (J2000)	v_{LSR} [km s $^{-1}$]	I_{peak} [Jy beam $^{-1}$]	F [Jy]
22:56:17.96363	62:01:49.4259	-2.91	1.1	2.5
22:56:17.96082	62:01:49.4364	-2.91	0.9	1.1
22:56:17.91577	62:01:49.5567	-2.91	0.2	0.4
22:56:17.89509	62:01:49.6233	-2.91	0.5	1.3
22:56:17.96364	62:01:49.4260	-3.00	0.8	1.4
22:56:17.91569	62:01:49.5581	-3.00	0.7	1.2
22:56:17.96362	62:01:49.4263	-3.09	0.3	0.4
22:56:17.91564	62:01:49.5588	-3.09	0.8	1.3
22:56:17.96988	62:01:49.4386	-3.18	0.2	0.2
22:56:17.91560	62:01:49.5592	-3.18	0.4	0.6
22:56:17.96988	62:01:49.4387	-3.26	0.3	0.4
22:56:17.87414	62:01:49.7124	-3.26	0.2	1.2
22:56:17.96987	62:01:49.4387	-3.35	0.3	0.3
22:56:17.87506	62:01:49.7049	-3.35	0.4	2.1
22:56:17.87396	62:01:49.7105	-3.35	0.6	2.0
22:56:17.96982	62:01:49.4387	-3.44	0.2	0.2
22:56:17.87555	62:01:49.7023	-3.44	0.7	1.4
22:56:17.87421	62:01:49.7063	-3.44	0.9	2.4
22:56:17.87248	62:01:49.7294	-3.44	0.2	0.2
22:56:17.87433	62:01:49.7038	-3.53	0.8	1.3
22:56:17.86686	62:01:49.7460	-3.53	0.8	1.5
22:56:17.86047	62:01:49.8186	-3.53	1.2	1.8
22:56:17.87135	62:01:49.9011	-3.53	0.2	0.3
22:56:17.86688	62:01:49.7449	-3.61	2.8	6.2
22:56:17.86038	62:01:49.8191	-3.61	2.5	3.6
22:56:17.86265	62:01:49.8313	-3.61	0.5	0.8
22:56:17.87133	62:01:49.9007	-3.61	0.4	0.8
22:56:17.87820	62:01:49.9047	-3.61	0.2	0.4
22:56:17.86687	62:01:49.7442	-3.70	3.8	9.3
22:56:17.86026	62:01:49.8200	-3.70	1.6	2.1
22:56:18.09933	62:01:49.4214	-3.79	0.7	1.6
22:56:17.86586	62:01:49.7630	-3.79	0.7	2.0
22:56:17.86687	62:01:49.7431	-3.79	2.4	5.8
22:56:18.09493	62:01:49.3971	-3.88	0.9	3.3
22:56:18.09913	62:01:49.4211	-3.88	0.8	1.6
22:56:17.86692	62:01:49.7423	-3.88	1.1	2.9
22:56:18.09559	62:01:49.4004	-3.97	3.1	9.8
22:56:17.86710	62:01:49.7417	-3.97	0.3	0.7
22:56:17.85946	62:01:49.7724	-3.97	0.3	0.9
22:56:18.09627	62:01:49.4033	-4.05	5.6	21.7

Table 2.3: Continued.

RA (J2000)	DEC (J2000)	v_{LSR} [km s^{-1}]	I_{peak} [Jy beam^{-1}]	F [Jy]
22:56:18.09648	62:01:49.4049	-4.14	9.5	20.2
22:56:18.09652	62:01:49.4054	-4.23	8.3	12.3
22:56:17.92613	62:01:50.2357	-4.32	0.2	1.5
22:56:18.09651	62:01:49.4055	-4.32	2.7	3.5
22:56:17.92598	62:01:50.2361	-4.40	0.3	1.7
22:56:17.92753	62:01:50.0846	-4.49	0.4	1.4
22:56:17.92729	62:01:50.0863	-4.58	0.6	2.1
22:56:17.92688	62:01:50.0894	-4.67	0.3	0.7
22:56:17.92290	62:01:50.1160	-4.76	0.2	0.8

2.3.2 12.2 GHz results

The 12.2 GHz methanol maser emission is grouped in two distinct clumps detected in all four epochs, a spectra of one epoch is shown in Fig. 2.2. The two 12.2 GHz maser clumps are associated with the 6.7 GHz maser clumps *a* and *c* in the 6.7 GHz maser map (Fig. 2.1) and their absolute positions are reported in Table 2.4. The first two of our epochs are separated by only 20 days to those of Mos09 and for these our absolute positions agree with only a small ~ 1.6 mas offset in declination. This offset is probably due to different calibration strategies, in particular we do not include the rigorous tropospheric corrections of Mos09. The absolute astrometry of Min01 (30 mas accuracy) is not quite good enough for a comparison on the mas level, and although their 12.2 GHz maser feature seems to be associated with a different 6.7 GHz feature (*d*), the general morphology and velocity field look very similar.

The separation of the 12.2 GHz maser clumps for the four epochs of our observations, the five epochs of Mos09, and the epoch of Min01 is shown in Fig. 2.3. The measured separation of the two clumps ($\sim 1.357''$) agrees well with those of Mos09. The measurement by Min01 shows a separation of ~ 6 mas less, though due to the large separation in time we cannot be certain that it is the same parcel of gas. By fitting a straight line to the data points (with the exception of the Min01 data point which is only shown for completeness) we find the separation to be increasing by $0.87 \pm 1.72 \text{ km s}^{-1}$ ($0.26 \pm 0.52 \text{ mas year}^{-1}$). Mos09 found the separation to be increasing by 6.3 km s^{-1} , and by looking at Fig. 2.3, it is clear that this value is largely determined by the separation derived from his last epoch which is inconsistent with our measurements. In conclusion, taking into consideration the error bars of our measurements, we do not see any significant change in the separation over the time period (~ 16.5 months) spanned by Mos09 and our observations.

Although taken at ~ 1.5 year separated epochs, the 12.2 GHz masers are closely (20 – 40 mas) associated with the 6.7 GHz methanol masers and show the same velocity field.

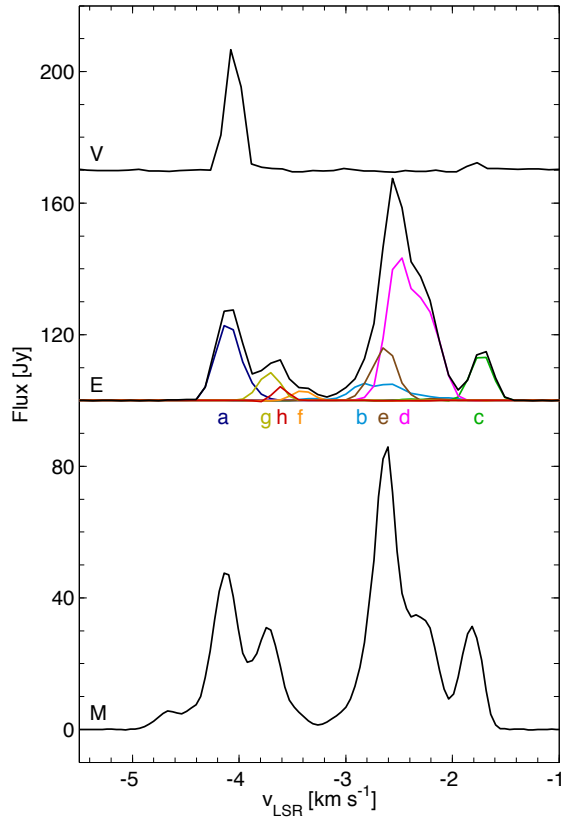


Figure 2.2: *Bottom:* (M) Merlin 6.7 GHz maser spectrum scaled down by a factor of 5 (Vlemmings et al. 2010). *Middle:* (E) Our 6.7 GHz total maser spectrum (black line) and individual spectra of maser clumps, from East (a) to West (h) as measured by the EVN. *Top:* (V) A representative 12.2 GHz maser spectra measured with the VLBA scaled up by factor of 5.

2 Dynamics of the methanol masers around Cepheus A HW2

However, if the emission was arising from the same gas, the observed offset would imply velocities between 50 and 100 km s⁻¹. Such high velocities should result in measurable proper motions over the time span covered by our observations and we therefore believe that the separation is due to either variability, or more likely, that the 6.7 and 12.2 GHz maser emission do not exactly arise in the same gas.

We compared whether there was any association between the methanol masers and any other masing species (water or hydroxyl) in Cep A. Only in one position, namely in the elongated structure to the East did we find a close association with water masers. The methanol maser emission is spatially coincident < 5 mas to the 22 GHz water masers observed by Vlemmings et al. (2006), Torrelles et al. (2010). The 6.7 and 12.2 GHz methanol masers are centred at -4.2 km s⁻¹, in contrast, the 22 GHz water masers are observed at ~ -14 km s⁻¹. This velocity offset will be further discussed in Sec. 2.5.

Table 2.4: The absolute positions and LSR velocities of 12.2 GHz methanol maser clumps measured using VLBA for the four different epochs (I – IV).

Epoch	RA (J2000) 22:56:	Dec (J2000) 62:01:	Velocity [km s ⁻¹]
I	18.097074	49.39635	-4.1
	17.905360	49.54696	-1.8
II	18.097174	49.39681	-4.1
	17.905432	49.54742	-1.8
III	18.096963	49.39687	-4.1
	17.905200	49.54781	-1.8
IV	18.096775	49.39301	-4.1
	17.905086	49.54415	-1.8

2.4 Analysis

2.4.1 Ring model

The methanol maser emission seems to arise in a large-scale, ring-like structure close to or in the equatorial region of the high-mass object driving the HW2 jet. Such elliptical structures have recently been discovered in a substantial fraction of methanol masers studied in detail with VLBI (Bartkiewicz et al. 2005b, 2009). To model our data we have done a least square fit of an ellipse to the positions of our 6.7 GHz methanol maser spots. We solve for the ellipse’s semi-major and semi-minor axes, the position angle and for the position offset with respect to the 7 mm continuum object identified by Curiel et al. (2006). Furthermore, assuming that the maser emission is arising in a circular ring structure, we convert the fitted ellipse to a position angle of the minor axis, a radius and an inclination of the ring.

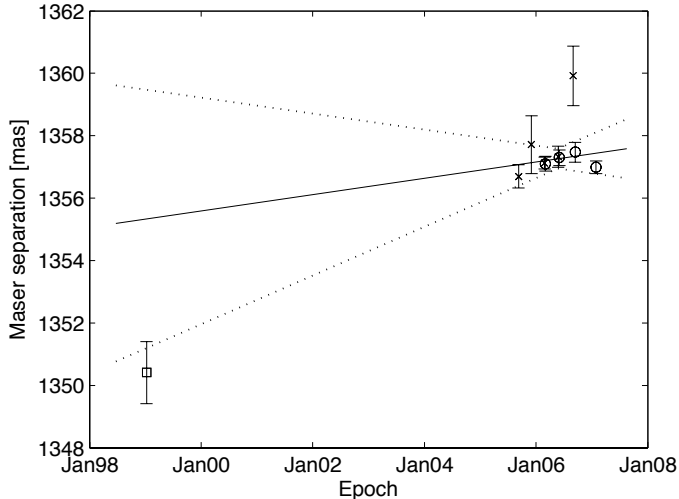


Figure 2.3: Separation of the 12.2 GHz maser clumps in mas. Our four epochs are marked as circles, also shown are previous measurements by Min01 (square) and Mos09 (crosses). The solid line indicates our best fit and the dotted lines the errors of the fit.

The best fit and model results are presented in Fig. 2.4, with offsets relative to the phase centre (Table 2.1). As one can clearly see the maser spots are consistent with an ellipse only slightly offset from the 7 mm continuum object ($\Delta\alpha = -106$ mas, $\Delta\delta = 197$ mas). The semi-major axis of the fitted ellipse is 968 mas (678 AU), and the semi-minor axis 371 mas (260 AU). We find the position angle of the minor axis to be 9.3° . The radio jet and the large scale molecular outflow have a position angle of 45° and given that these are completely different structures we note that they seem to be pointing in the same general direction. Assuming the masers are in an inclined ring we find an inclination of 67.5° , which is slightly larger than the best fit of 62° that was found for the dust and molecular disk (Patel et al. 2005). Both the position angle and the inclination of the ring are in good agreement with the MERLIN 6.7 GHz maser observations ($i=71^\circ$, $pa=12^\circ$) by Vlemmings et al. (2010).

The ring model fitted to the methanol maser positions is used to compare two simple models that have different kinematic signatures: radial velocities ($v(PA) = v_{\text{sys}} + v_{\text{rad}} \times \sin(i) \sin(PA)$) and Keplerian rotation ($v(PA) = v_{\text{sys}} + v_{\text{rot}} \times \sin(i) \cos(PA)$), Fig. 2.4. For the radial velocity model we find a system velocity of $v_{\text{sys}} = -3.8 \text{ km s}^{-1}$ and a radial velocity $v_{\text{rad}} = -1.3 \text{ km s}^{-1}$. For the rotation model we find a $v_{\text{sys}} = -3.1 \text{ km s}^{-1}$ and a rotation velocity, $v_{\text{rot}} = 0.2 \text{ km s}^{-1}$. Assuming Keplerian rotation this would correspond to a mass of $\sim 0.04 M_{\odot}$, which is much too low for any reasonable model of the mass enclosed, we therefore rule out this possibility. Moreover, the rotation model does not fit. In Fig. 2.1 the maser regions to the East and West show similar velocities and the high velocity is seen towards the centre, this is a sign of radial motions, not of rotation.

2 Dynamics of the methanol masers around Cepheus A HW2

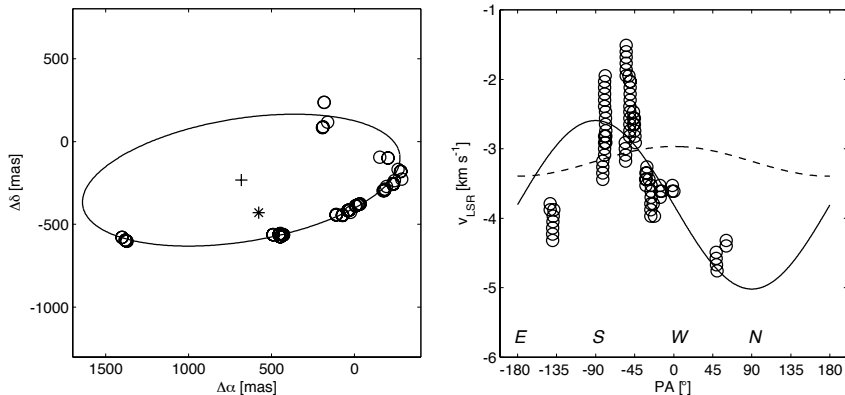


Figure 2.4: Fit of the ring model: Left panel shows the maser positions in circles and the fitted ellipse, with the + sign designating the centre of the ellipse. The star indicates the position of the 7 mm continuum object identified by Curiel et al. (2006). Right panel shows in the measured velocities (circles) as a function of the position angle (PA) in our ring model. The solid line shows the fit to a radial velocity model and the dashed line shows the result of a Keplerian velocity model.

Whether the radial motions can be attributed to infall or outflow, depends on the sign of the inclination; if the half-ellipse from which we see the maser emission is the front-side, the signature is that of infall. In Sect. 2.5 we argue that most observed effects are indeed consistent with this. With the long baselines of the EVN the maser emission is broken up in many individual spots, it is however clear we see the same structure as observed with the MERLIN (Vlemmings et al. 2010).

2.4.2 Parallax - distance

As we have independent measurements of the absolute positions of the 12.2 GHz maser clumps, we can verify the important findings of Mos09 on the distance to Cep A. A significant difference with their processing setup is that we have not included an estimate of the tropospheric errors (Reid et al. 2009a), probably resulting in the 1.6 mas offset in declination. Moreover, we have only one of the two calibrators in common. Otherwise the data is of very similar quality and we can fit our observations with the same parameters for proper motion and parallax. As was the case for Mos09 the right ascension data is very inconclusive, but the declination data result in an unambiguous determination of the parallax. Combining the measurements, taking out the aforementioned 1.6 mas offset, we can find a consistent result, $\pi = 1.567 \pm 0.087$ mas ($0.64^{+0.04}_{-0.03}$ kpc). However, we think the Mos09 value of $0.70^{+0.04}_{-0.04}$ kpc is probably still preferred because of a more thorough treatment of systematic errors.

2.5 Discussion

Although individual maser spots are small scale signposts of specific excitation conditions, the morphology and velocity field of the maser emission show that they occur within a single large scale (~ 1350 AU) ring structure around the high mass protostar HW2. Such structures have recently been found in a large number of methanol maser sources (Bartkiewicz et al. 2009), indicating that at least a fraction of the methanol masers are associated with specific conditions at a few hundred AU from the central source. Cep A HW2 is unique in that we can determine both the inclination of the ring as seen in methanol masers and the outflow direction as seen in radio continuum. This allows us, together with the large scale ($\sim 1'$) molecular outflow, to constrain the geometry of the system. The molecular outflow to the NE is blueshifted, pointing towards us and the outflow to the SW is redshifted, pointing away from us (Gómez et al. 1999). The orientation of the ring and its location suggest that the main part of the methanol maser emission (the large arc) arises on the near side of the jet, and the maser emission in the centre is seen in projection against the south western radio lobe. The maser emission to NNE of the centre of the ring (from the presumed far side) are only just detected with the EVN.

We can consider a few causes for the lesser brightness of the maser emission from the presumed far side of the ring. Assuming optically thin emission at 7 mm, Curiel et al. (2006) found an electron density of $(1-5)\times 10^4$ cm^{-3} in the radio jet, not enough for the emission to be optically thick at 6.7 GHz. For an optical depth of $\tau = 1$ at 6.7 GHz an emission measure of $> 1.7 \times 10^8$ cm^{-6} pc^{-1} is required, assuming an electron temperature of 10^4 K. This corresponds to an electron density $> 1.5 \times 10^5$ cm^{-3} within the ring, a few times higher than the value found by Curiel et al. (2006). However, the rising spectra from 3.6 cm to 7 mm suggest that the optical depth is significant at 6.7 GHz, and it is therefore reasonable that optical depth effects play some role in at least part of the ring. A second cause for the maser emission from the near side of the ring to be brighter than the far side is the background radiation from the central object enhancing the outward radial maser brightness. This is supported by the lower brightness/larger scale maser emission arising from the far side of the ring and observed with MERLIN (Vlemmings et al. 2010) which may to a high degree be filtered out on the much longer EVN baselines. For the remainder of the discussion we assume that the maser emission delineating the arc arises on the near side of the jet.

Then, the velocity field of the masers, with the blueshifted masers towards the sides (tangents) and the more redshifted masers towards the centre indicates an infall signature. No clear signs of rotation are seen. We note that similar velocity “spurs” as seen in Fig. 2.4 have been seen in other maser sources (Bartkiewicz et al. 2009) and seem inherent to the clumpy maser emission. In fact, the velocity gradient in individual maser features could be the result of gas starting to be entrained in the rotation of the accretion disk. The low velocity maser emission (~ -4.6 km s^{-1}) that we just detect and that is seen at shorter baselines falls within the third quarter of the velocity diagram of Fig. 2.4 where we expect velocities between -4.2 and -5.9 km s^{-1} . Although we cannot completely rule out that the 6.7 and 12.2 GHz methanol maser emission do not arise from within the same parcels of gas, the close association and similar velocities indicate that at least they occur in the

2 Dynamics of the methanol masers around Cepheus A HW2

same large scale structure in the equatorial region of HW2. The velocity field of the masers suggests a modest infall, although the fact that we do not measure any significant change in the separation between the 12.2 GHz clumps, seems to indicate that they do not move relative to each other. We tentatively identify this ring structure as the interface between the larger scale accretion flow and a circumstellar disk. This scenario is further supported by the large scale magnetic field perpendicular to the ring structure (Vlemmings et al. 2010).

Recent observations of the 22 GHz water masers in the region of Cep A HW2 show that the water masers trace a relatively slow, wide-angle (102°) outflow to the NE, present at the same time and on similar spatial scales ($\sim 1''$) as the highly collimated jet seen in radio continuum with outflow velocities in excess of 500 km s^{-1} (Torrelles et al. 2010). In the East the methanol masers are closely associated with these water masers. However, the proper motions and velocity fields of the methanol masers show that they do not trace the same part of the structure. A similar close association between water and methanol masers with a different velocity field has previously been seen in at least one other source (AFGL 5142). The results by Goddi et al. (2007) indicate that the water masers trace expansion, possibly related to the disk-wind interface, whereas the methanol masers seem to trace an infall. This could be understood from the different conditions required; models of maser excitation show that water masers requires a denser ($n > 10^9 \text{ cm}^{-3}$) and warmer medium in which the methanol masers are quenched (Elitzur et al. 1989, Cragg et al. 2005). In Cep A, the previously noted velocity offset of $\sim 10 \text{ km s}^{-1}$ between the two maser species suggest a shock front in which the methanol masers occur outside (upstream) of the shock interface, in the infalling gas, and the water masers occur further downstream or behind the shock front, where conditions are more favourable for water maser excitation.

Monitoring of the 6.7 GHz methanol masers have shown the maser emission to be not only variable but also that the variability is synchronised and anti-correlated between different sections of the ring (Sugiyama et al. 2008a). As the intensity in the blueshifted masers to the East and West decreases the intensity of the redshifted masers towards the centre increases. The authors ascribe the variability to changes to the excitation conditions in the environment in which the maser emission occur, and that the masers towards the centre are closer to the central object than the blueshifted masers. The variability could also be consistent with a model in which amplification of the HW2 radio continuum is important. In this scenario the radial amplification will be enhanced as the intensity of the central object increases. The increase in radial amplification would enhance the beaming, and consequently decrease the tangential amplification. This explanation could be tested by simultaneously monitoring the maser and the radio continuum emission (with for example the e-VLA or e-MERLIN).

2.6 Conclusions

We find the methanol maser emission in Cep A to arise in a large scale ring structure straddling the waist of the thermal jet HW2. We find the ring to have a radius of 678 AU centred close to the previously identified central object driving the HW2 radio jet. Fur-

ther, the minor axis of the ring is in the general direction of the radio jet, the large scale molecular outflow, and the large scale magnetic field. The geometry suggests that the ring is inclined with the NE part towards us and the maser emission arises on the near side of the ring. This leads us to interpret the velocity field of the methanol masers as showing signs of modest infall although we do not see any change in the separation of the maser clumps. Based on the geometry, velocity field, and large velocity offset from the water masers we propose that the methanol masers occur in a shock interface of the infalling gas, on the interface with the accretion disk. We also suggest that amplification of background radio continuum is important in the appearance and variability of the methanol maser emission. Our independent fit of the parallax to Cep A HW2 confirms the previously measured parallax of Mos09.

Acknowledgements

This research was supported by the EU Framework 6 Marie Curie Early Stage Training programme under contract number MEST-CT-2005-19669 “ESTRELA”. WV acknowledges support by the *Deutsche Forschungsgemeinschaft* through the Emmy Noether Research grant VL 61/3-1. We are grateful to Luca Moscadelli and collaborators for kindly sharing their results (Mos09) in digital form with us.

Distribution and excitation of thermal methanol in 6.7 GHz maser bearing star-forming regions

I. The nearby source Cepheus A¹

Abstract

Candidate high-mass star-forming regions can be identified through the occurrence of 6.7 GHz methanol masers. In these sources the methanol abundance of the gas must be enhanced, because the masers require a considerable methanol path length. The place and time of origin of this enhancement is not well known. Similarly, it is debated in which of the physical components of the high-mass star-forming region the masers are located. The aim of this study is to investigate the distribution and excitation of the methanol gas around Cep A and to describe the physical conditions of the region. In addition the large-scale abundance distribution is determined in order to understand the morphology and kinematics of star-forming regions in which methanol masers occur. The spatial distribution of methanol is studied by mapping the line emission, as well as the column density and excitation temperature, which are estimated using rotation diagrams. For a limited number of positions the parameters are checked with non-LTE models. Furthermore, the distribution of the methanol abundance is derived in comparison with archival dust continuum maps. Methanol is detected over a 0.3×0.15 pc area centred on the Cep A HW2 source and shows an outflow signature. Most of the gas can be characterised by a moderately warm rotation temperature (30–60 K). At the central position two velocity components are detected with different excitation characteristics, the first related to the large-scale outflow. The second component, uniquely detected at the central location, is probably associated with the maser emission on much smaller scales of $2''$. A detailed analysis reveals that the highest densities and temperatures occur for these inner components. In the inner region the dust and gas are shown to have different physical parameters.

¹Based on: Karl J. E. Torstensson, Floris F. S. van der Tak, Huib Jan van Langevelde, Lars E. Kristensen, Wouter H. T. Vlemmings, 2011, A&A, 529, 32

3 Distribution and excitation of thermal methanol in Cepheus A

Abundances of methanol in the range $10^{-9} - 10^{-7}$ are inferred, with the abundance peaking at the maser position. The geometry of the large-scale methanol is in accordance with previous determinations of the Cep A geometry, in particular those from methanol masers. The dynamical and chemical time-scales are consistent with a scenario where the methanol originates in a single driving source associated with the HW2 object and the masers in its equatorial region.

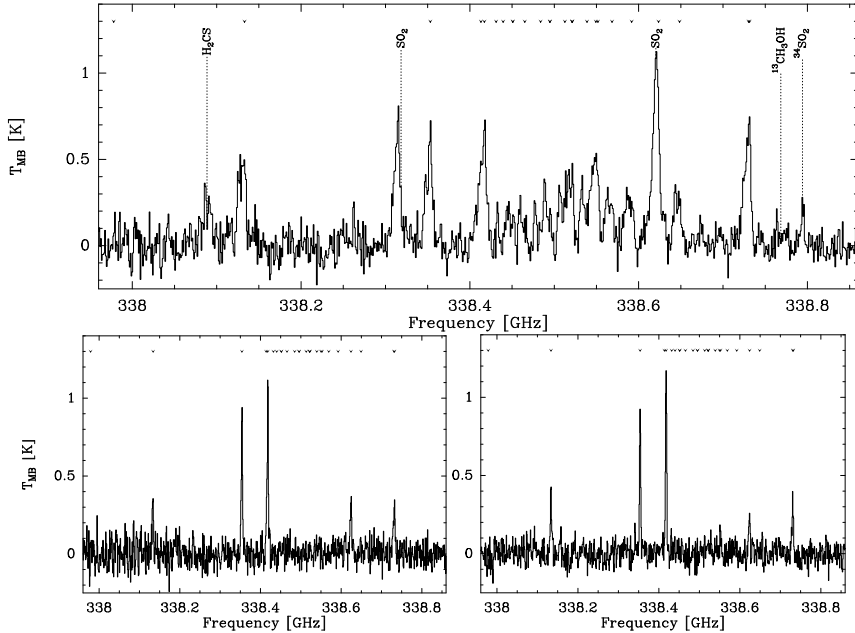


Figure 3.1: Sample spectra from the 3 positions identified in Sec. 3.3.2. *Top* spectrum at the "Centre" position, coincident with the HW2 object. *Bottom Left* at the position of "NE Outflow" and *Bottom Right* "Envelope". The small symbols at the top indicate the frequencies of methanol transitions in this band.

3.1 Introduction

While massive stars ($\geq 10 M_{\odot}$) have an enormous impact on the evolution of the Galaxy during their life and death, their birth process is still shrouded in mystery (e.g. Kurtz 2005). To a large extent this is because of the environment in which the high-mass stars form. Most high-mass stars are observed at large distances (compared to low-mass stars), evolve rapidly, and form deeply embedded in their molecular clouds. Additionally, they typically form in clusters. Thus, very high-resolution data are needed to resolve them and the disruptive influence they have on their direct environments (e.g. Martín-Pintado et al. 2005).

Methanol maser sources are exciting targets for the detailed study of high-mass star-formation. Continuum emission of warm dust at sub-millimetre wavelengths has been detected at well over 95% of the observed 6.7 GHz methanol maser sites (Hill et al. 2005), while 25% of the same masers are associated with a detectable ultra-compact (UC) HII region (Walsh et al. 1998). This seems to indicate that the masers probe a range of early phases of massive star-formation and that the methanol maser emission disappears when the UC HII region is created (Walsh et al. 1998). The maser sources require high methanol

3 Distribution and excitation of thermal methanol in Cepheus A

abundance for their excitation, which points to a recent release of methanol into the gas phase (van der Tak et al. 2000a). We can thus expect to observe the thermal methanol lines in these sources, which will then yield diagnostics for the large-scale kinematics and excitation. Besides being signposts, masers are excellent tracers of the geometry and small-scale dynamics of these regions. Much effort has focused on studying the kinematics, and several claims of circumstellar disks, expanding spherical shells, and jets have been presented (e.g. Pestalozzi et al. 2004, Minier et al. 2002, Bartkiewicz et al. 2005b, 2009). The evidence suggests that masers trace an evolutionary sequence or possibly a mass range in the formation process, or even both (e.g. Breen et al. 2010). However, it is not clear exactly with which of the physical structure(s) of the complex surroundings of young massive stars they are associated. By trying to make a link between the maser distribution and the large-scale methanol kinematics and excitation, one can attempt to reach a better understanding of the physical and chemical state of the gas of the regions in which masers occur.

To carry out such a study, we have observed thermal methanol gas towards a sample of 15 high-mass star-forming regions for which we have very long baseline interferometry (VLBI) data of the 6.7 GHz methanol maser. The observations yield maps of the distribution and physical condition of the methanol gas in relation to the methanol maser. These observations of methanol allow one to probe a reasonably wide range of temperature and density, because of its closely spaced $\Delta K = 0$ ($\Delta J = 1$) transitions with a wide range in excitation energies and critical densities (Leurini et al. 2004). Moreover, we can measure the methanol abundance and velocity field. Clearly, the methanol abundance needs to be significant in these regions ($> 10^{-7}$, Sobolev et al. 1997); evaporation of CH_3OH from the dust grains in these regions, at temperatures ~ 100 K is thought to be responsible for this. This specific enhancement is supposed to be so short-lived that it can be used as a chemical clock of the region (van der Tak et al. 2000a). The enhancement can be used to determine the age of these regions and thus the evolutionary stage of the star-formation process.

In this chapter, we describe the observations and the procedure we used to analyse the data. Because of its proximity and because a wealth of data exists on this source, we will focus on Cepheus A East as a first example. The other sources are presented in Chapter 4.

At a distance of 700 pc (Moscadelli et al. 2009), Cepheus A East is one of the closest high-mass star-forming regions. The region has a luminosity of $2.3 \times 10^4 L_{\odot}$ (Evans et al. 1981) (scaled to the distance of 700 pc), out of which half is thought to come from the well-studied object HW2 (Garay et al. 1996), which is also the site of the 6.7 GHz methanol maser emission. The object shows both large-scale molecular outflows over $\sim 1'$ (Gómez et al. 1999) and signs of collapse over a similar extent (Bottinelli & Williams 2004, Sun & Gao 2009). At the core of HW2, a thermal jet extends over $\sim 2''$ and proper motion outflow velocities of ~ 500 kms have been measured in the radio (Hughes & Wouterloot 1984, Curiel et al. 2006). Although a superposition of gas components at different positions cannot be completely ruled out (Brogan et al. 2007, Comito et al. 2007), the evidence is building that there is a disk at the centre of the jet, which is observable in both molecular gas and dust (Patel et al. 2005, Torrelles et al. 2007, Jiménez-Serra et al. 2007), as argued in detail in Jiménez-Serra et al. (2009). VLBI observations of the

6.7 GHz methanol maser suggest that the methanol masers originate in a ring-like structure that extends over $\sim 2''$ and straddles the waist of HW2, see Chapter 2 (Sugiyama et al. 2008b, Vlemmings et al. 2010, Torstensson et al. 2011).

In Sec. 3.2 we describe the observations and calibration methods. The results are presented in Sec. 3.3 in the form of a number of sample spectra and maps of integrated line strength and velocity. To study the large-scale methanol excitation we construct rotation diagrams and produce maps of the derived physical quantities in Sec. 3.4. We present non-LTE calculations for a number of positions to evaluate the limitations of the diagram analysis in Sec. 3.4.4. Subsequently we discuss estimates of the hydrogen column density before we present the methanol abundance in Sec. 3.4.6. The relation of our findings to the Cep A star-forming process and in particular the occurrence of the methanol maser are discussed in Sec. 3.5.

3.2 Observations and data reduction

The JCMT¹ observations of Cep A East (HW2) ($22^h56^m17.9^s +62^\circ01'49''$ (J2000)) were performed on June 2 and June 17, 2007. We used the array receiver HARP, which has 16 receptors with a spacing of $\sim 30''$ in a 4×4 grid, resulting in a footprint of $\sim 2'$. The receptors are single sideband receivers with a sideband rejection of >10 dB. We used the observing mode HARP5, a type of beam-switching (jiggle-chop) mode where several short scans at different positions of the target source (10 s per jiggle position) are observed before switching to the off-position. As a result, several on-source observations share the same off-source observation, which minimises the overhead while still providing good baselines. The observing mode results in a map of 20×20 pixels covering $2' \times 2'$, thus each pixel is $6'' \times 6''$. This ensures proper Nyquist sampling of the $14''$ telescope beam at 338 GHz.

The ACSIS correlator backend was set up with a 1 GHz (880 kms) bandwidth and 2048 channels centred on the methanol $7_0 \rightarrow 6_0$ A⁺ line at 338.41 GHz. The frequency set-up allowed us to cover 25 CH₃OH lines (Table 3.1) with a velocity resolution of ~ 0.43 kms (488 kHz). In total we have an effective (on source) integration time of ~ 5 min per pixel with a typical system temperature (T_{sys}) of ~ 280 K. For our analysis we adopted a main-beam efficiency (η_{mb}) of 0.6. Regular pointings were made of the normal calibrators, and we estimate to have an absolute pointing accuracy of $\approx 1''$.

We used the Starlink package (Gaia and Splat) for an initial inspection of the data. It was found that receptor R06 suffered from bad baselines (large ripples in some scans). For that receptor only these poor scans were removed, after which the scans were combined. The data were then converted into the GILDAS/CLASS format, and the remaining data reduction and analysis was performed in CLASS. A linear baseline was fitted to several spectral regions without any line emission and subtracted from the spectra. Then the data

¹The James Clerk Maxwell Telescope is operated by the Joint Astronomy Centre on behalf of the Science and Technology Facilities Council of the United Kingdom, the Netherlands Organisation for Scientific Research, and the National Research Council of Canada.

3 Distribution and excitation of thermal methanol in Cepheus A

Table 3.1: CH₃OH line data for the observed transitions, adopted from the CDMS (Cologne Database of Molecular Spectroscopy, Müller et al. (2005)). All lines are from the $J = 7 \rightarrow 6$ band, and throughout the chapter a notation like “-6 E” refers to the $J = 7_{-6} \rightarrow 6_{-6}$ E transition. Blended lines are indicated by a *.

Frequency MHz	$\mu_g^2 S_g$ D ²	E_u K	Transition K type
337969.414	5.55	390.1	-1 A $\nu_t=1$
338124.502	5.65	78.1	0 E
338344.628	5.55	70.6	-1 E
338404.580	1.49	243.8	+6 E
338408.681	5.66	65.0	0 A
338430.933	1.50	253.9	-6 E
338442.344*	1.49	258.7	+6 A
338442.344*	1.49	258.7	-6 A
338456.499	2.76	189.0	-5 E
338475.290	2.76	201.1	+5 E
338486.337*	2.77	202.9	+5 A
338486.337*	2.77	202.9	-5 A
338504.099	3.80	152.9	-4 E
338512.627*	3.81	145.3	-4 A
338512.639*	3.81	145.3	+4 A
338512.856*	5.23	102.7	-2 A
338530.249	3.82	161.0	+4 E
338540.795*	4.60	114.8	+3 A
338543.204*	4.60	114.8	-3 A
338559.928	4.64	127.7	-3 E
338583.195	4.62	112.7	+3 E
338614.999	5.68	86.1	+1 E
338639.939	5.23	102.7	+2 A
338721.630	5.14	87.3	+2 E
338722.940	5.20	90.9	-2 E

were smoothed in the spectral domain to improve the signal-to-noise ratio, which resulted in a velocity resolution of 0.87 kms and an rms of ~ 65 mK.

The analysis was performed on a pixel-by-pixel basis by first fitting a Gaussian to the strongest unblended line ($7_{-1} \rightarrow 6_{-1}$ E) in the spectra. The measured velocity and width of this line were then used to place windows around all other features in the spectra for which the emission was integrated. Owing to some overlap between different lines, only lines with a $>5\sigma$ (~ 0.6 K km s $^{-1}$) detection are included in the subsequent analysis. In the centre area, at the position of HW2, a second velocity component can be distinguished. Where we were able to separate the two velocity components, we performed a manual analysis by fitting individual Gaussians to the lines.

3.3 Results

3.3.1 Methanol lines

In the following we refer to each pixel in the map with its respective offset coordinates ($\Delta\alpha$, $\Delta\delta$), measured in arc seconds, with respect to the centre of the map (J2000 $22^h56^m17.88^s +62^\circ01'49.2''$). Fig. 3.1 shows the observed spectrum at three positions: (+3'',3'') ‘‘Centre’’, (+27'',+9'') ‘‘NE outflow’’, (+21'',-3'') ‘‘Envelope’’, where the designations can be understood from the subsequent discussion in Sec. 3.3.2. Focusing at the centre spectrum, all but four of the detected lines are originating from methanol (indicated by ticks at the top); the others are identified as SO $_2$, 34 SO $_2$, and H $_2$ CS. The CH $_3$ OH $K=+1$ E line is a blend with another SO $_2$ line, which is also indicated in the figure.

In the centre spectrum, two gas components are observed: the main component with $v_{\text{lsr}} = -10.5$ km s $^{-1}$ and a secondary red shifted at -5.2 km s $^{-1}$, as can be seen in the profile of the -1 E transition (Fig. 3.2). We note that the red-shifted velocity profile is overlapping with the range spanned by the methanol masers, which are observed with velocities between $v_{\text{lsr}} = -4.6$ and -1.5 km s $^{-1}$ (Chapter 2). The redshifted component is most readily identified in the higher K transitions. While the first component is brightest in the low K transitions and not detected in the higher K lines, the -5.2 km s $^{-1}$ component is brighter in the higher K lines and less bright in the lower K lines. For the $K=3$ transitions, the two components are of similar strength. There is a weak detection of the methanol isotopologue $^{13}\text{CH}_3\text{OH } J=13 \rightarrow 12, \Delta K = +1$ in this component, which indicates that optical depth effects may be important for this. Moreover, a careful analysis, which includes averaging over a few pixels, shows that the torsionally excited -1 A $v_t=1$ line at 337.969 GHz is detected in the ‘‘Centre’’ region in the -5.2 km s $^{-1}$ velocity component.

Otherwise the observed line profile appears Gaussian in all components and does not show evidence of blue/redshifted wings. However, a modest velocity shift of the line is observed across the source with lower velocities to the NE and higher velocities to the SW (Fig. 3.2).

To begin a consistent analysis of all methanol line emission in our data cube, we extracted the integrated line flux from each line as described above (Sec. 3.2). To illustrate our procedure, we list the integrated line emission of the spectral features for the main

3 Distribution and excitation of thermal methanol in Cepheus A

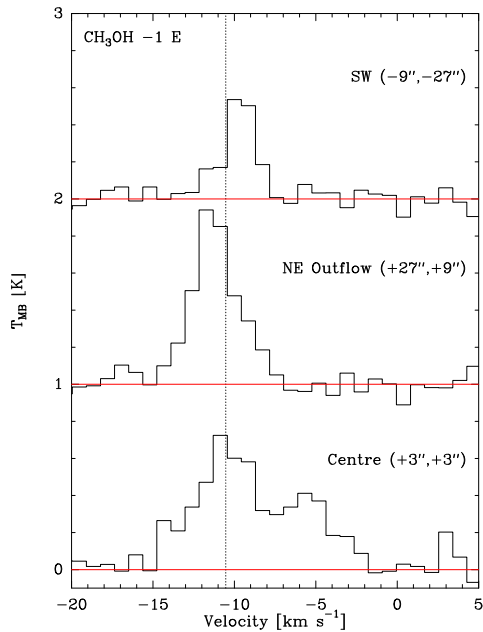


Figure 3.2: Velocity profiles of the -1 E line at three positions. Although the profiles are Gaussian in the outflow, there is a clear shift in the velocity. At the “Centre” position there are clearly two velocity components. The dotted line is taken to be the system velocity, corresponding to the velocity of the dominant component at the “Centre” position.

Table 3.2: Line parameters for the main velocity component measured at the position of HW2 (+3'',+3'')

Line K , type ¹	Flux K km s^{-1}	Width km s^{-1}
0 E	2.16	4.21
-1 E	3.30	4.79
0 A	3.60	4.79
-6 E	0.03	1.74
+6 A	0.29	3.80
-6 A	0.29	3.80
-5 E	0.61	4.81
+5 E	0.31	3.15
+5 A	0.36	4.18
-5 A ²	0.36	4.18
-4 E	1.05	4.79
-2 A ³	2.00	4.79
+4 E	1.12	4.79
+3 A	1.37	4.79
-3 A ⁴	1.37	4.79
-3 E	0.93	4.07
+3 E	0.94	4.97
+2 A	1.42	5.38
+2 E	1.55	4.38
-2 E ⁵	1.55	4.38

^aSee Table 1 for transition details^bBlend with +5 A^cBlend with ± 4 A^dBlend with +3 A^eBlend with +2 E

velocity component at the ‘‘Centre’’ position from Fig. 3.1 in Table 3.2. For lines that are blended we chose a simple strategy. If the strengths ($S_g \mu_g^2$) of the lines are similar and they have comparable upper energy levels, we splitted the measured flux between the two lines. If, however, one line has a significantly higher line strength and lower upper energy level, we attribute the entire emission to the strong line. For the blend between the $K=-2$ A and $K=\pm 4$ A, where the lines have comparable line strengths and energy levels, we assume the total measured flux as an upper limit to all lines.

3.3.2 Spatial distribution of methanol

Fig. 3.3 shows the spatial distribution of the flux, the central velocity, and the width of the methanol $7_{-1} \rightarrow 6_{-1}$ E line, which is the brightest unblended feature in the spectra. The

3 Distribution and excitation of thermal methanol in Cepheus A

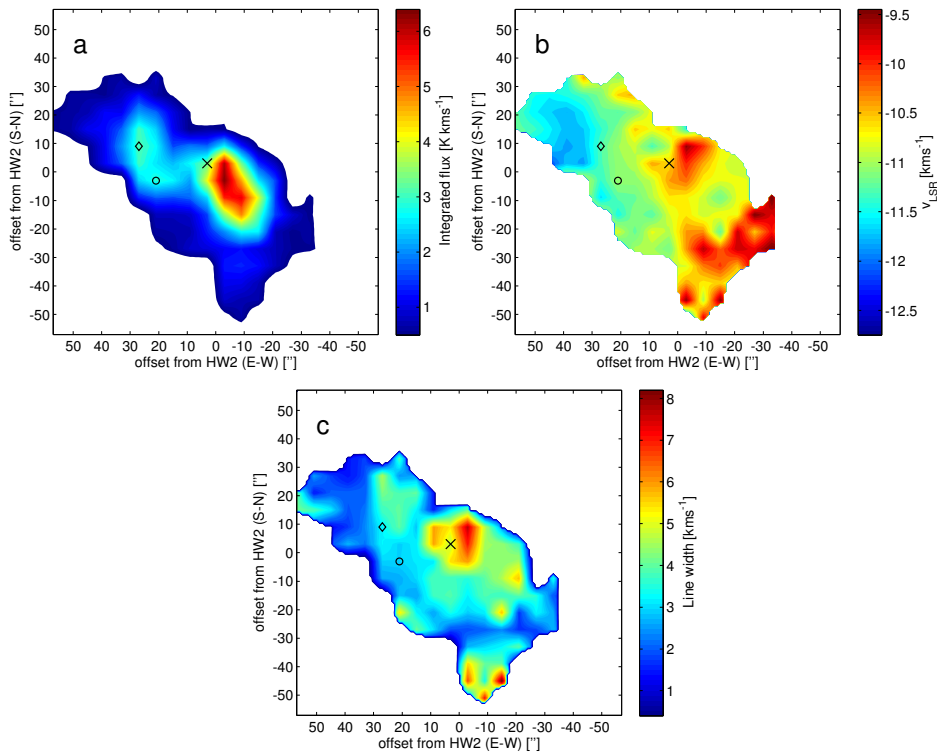


Figure 3.3: From top to bottom (a-c) the integrated flux, the velocity field, and the line width of the methanol $7_{-1} \rightarrow 6_{-1}$ E-type transition, the strongest unblended line in the observed spectra. In all maps the cross marks the “Centre” position, the diamond “NE Outflow” and the circle indicates the position where the “Envelope” spectra are evaluated.

methanol maser emission arises just to the NE of the centre of the map ($+0.7''$, $+0.4''$) and is indicated with a cross in all figures. The white area in the maps represents regions where the line flux is less than our 5σ detection limit of 0.6 K km s^{-1} .

The line emission is constrained to an area that is measured from the points that are farthest apart from each other in the intensity map (Fig. 3.3a), with an extent of $\sim 85''$ by $43''$ ($\sim 0.29 \text{ pc}$ by $\sim 0.15 \text{ pc}$), and is orientated in the NE-SW direction. The velocity map (Fig. 3.3b) shows that the methanol gas is entrained in an outflow with the blueshifted emission to the NE and the redshifted emission to the SW. Measured between the highest and lowest velocities in the map, the outflow has a modest velocity gradient of $\sim 3.1 \text{ km s}^{-1}$ over $\sim 0.20 \text{ pc}$. The integrated line flux peaks in the centre of the map at $\sim 5.2 \text{ K km s}^{-1}$, with a bright extension to the SW over $\sim 13''$ ($\sim 0.044 \text{ pc}$), which is associated with the red-shifted emission. Both the velocity field and line width maps (Figs. 3.3b and c) show a maximum in the centre of the map to the N of HW2. This is because of a blending

of the two velocity components that we are unable to decompose. A second maximum in the integrated line flux is observed $\sim 28''$ (~ 0.095 pc) to the NE of the centre, which is associated with the blueshifted part of the emission and a secondary peak in the line width map. Throughout the chapter we will refer to this position as the “NE outflow”. The quiescent methanol emission that is not associated with the outflows and does not show any peak in the integrated line flux map we will refer to as the “Envelope”.

3.4 Analysis

3.4.1 Rotation diagrams

From the above spectral cuts in three positions and the brightness distribution of one of the lines, it is clear that the observations trace a complex region in which the dynamic and excitation characteristics change, at least on the scales represented by the beam size of the telescope. To make a representation of the large-scale distribution and excitation of methanol, we created rotation diagrams (Boltzmann plots) at every pixel to be able to study the characteristics of the excitation distribution. Inherent to the method are a number of assumptions, namely that the gas at each velocity and spatial resolution element can be described by a single excitation temperature ($T_{\text{rot}} \equiv T_{\text{ex}}$), that all the lines are optically thin, i.e. $\tau \ll 1$, and that the size of the emitting region is the same for all lines. Although not all these assumptions may hold for all positions, the strength of the method is that it shows general trends on the relevant scales of our observations. In Sec. 3.4.4 we will test the validity of these assumptions.

For each pixel at which we measured at least three methanol transitions with $S/N > 5$, we plotted the upper energy level E_u [K] of the transitions on the x-axis versus the logarithm of the column density in the upper energy state divided by the statistical weight of that upper level $\log(N_u/g_u)$ on the y-axis. The weighted column density (N_u/g_u) can be calculated with Eq. 3.1 (Helmich et al. 1994) and the appropriate coefficients in Table 3.1. In the equation $Q(T_{\text{rot}})$ is the partition function, μ the permanent dipole moment [Debye], S_g the line strength value from (Blake et al. 1987), and T_{MB} the main beam temperature is the antenna temperature scaled by the main beam efficiency.

$$\frac{N_u}{g_u} = \frac{N_M}{Q(T_{\text{rot}})} e^{-E_u/T_{\text{rot}}} \approx \frac{1.67 \cdot 10^{14}}{\nu \mu_g^2 S_g} \int T_{\text{MB}} dv \quad (3.1)$$

By fitting a straight line through these data points we determine the rotation temperature T_{rot} [K] and column density N_M [cm^{-2}] of the methanol gas. The rotation temperature is the negative inverse of the slope of the fitted line and the total column density is where the extrapolated line crosses the y-axis.

Fig. 3.4 shows the resulting rotation diagrams of the “Envelope” (the lower temperature quiescent gas), the “NE outflow”, and of the first velocity component at the “Centre” position of HW2. For the two positions in the outflow and envelope a single gas component provides a good fit to the data points with a rotation temperature of 30 K to 35 K and

3 Distribution and excitation of thermal methanol in Cepheus A

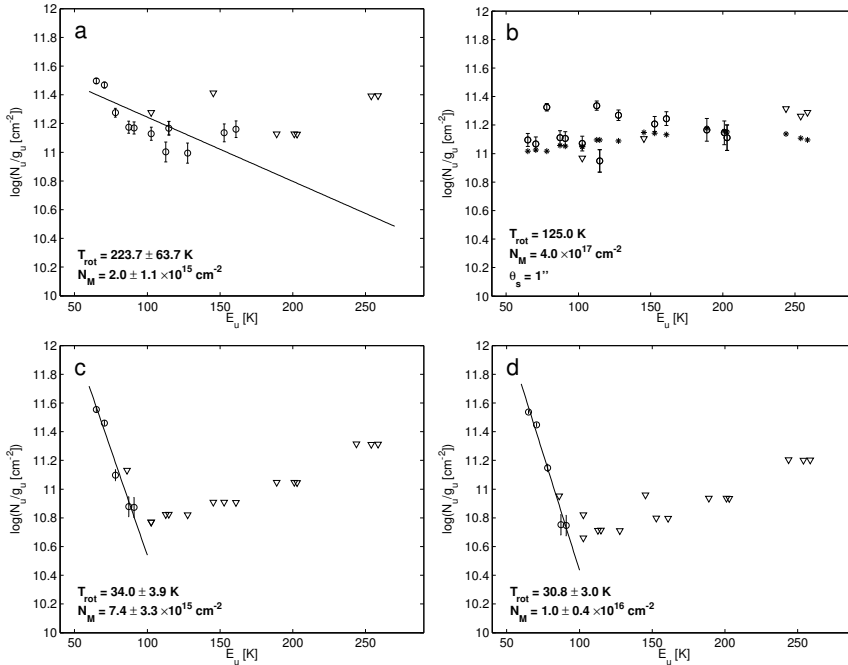


Figure 3.4: Rotation diagrams for three specific components and a population diagram for the fourth component identified in Sec. 3.3.2. Triangles indicate upper limits and error bars the 1σ standard deviation in the flux determination. The diagrams displayed are *a*: rotation diagram for the main, -10.5 km s^{-1} velocity component at the "Centre" position ($+3'', +3''$), *b*: population diagram for the redshifted, -5.2 km s^{-1} velocity component at the "Centre" position ($+3'', +3''$); for this model asterisks indicate a best fit that includes optical depth effects and beam dilution (see Sec. 3.4.2), *c*: rotation diagram for the "NE Outflow" ($+27'', +9''$), *d*: rotation diagram for "Envelope" ($+21'', -3''$).

a column density of 10^{16} cm^{-2} . However, in the centre region things are more complex. The velocity component at -10.5 km s^{-1} can be fitted by a straight line, which yields a rotation temperature of 224 K and a column density of $2 \times 10^{15} \text{ cm}^{-2}$. For the -5.2 km s^{-1} velocity component, the points lie nearly horizontal in the diagram and we were only able to put a lower limit of $>300 \text{ K}$ on the rotation temperature with the simple fit.

3.4.2 Population diagram modelling

Clearly the basic assumptions going into the rotation diagram analysis are violated for the ‘‘Centre’’ position, and a successful explanation must accommodate both an apparently negative rotation temperature and the relative weakness of the low K lines for the redshifted component. Non-LTE conditions, optical depth and beam-dilution effects can all play a role here. To investigate the effect of the line optical depth on the above results, we adopted, as a first step, the method of Goldsmith & Langer (1999), which includes the source size (θ_s) as a free parameter and allows for optical depth effects. We performed a χ^2 analysis for $10 < T_{\text{rot}} < 500 \text{ K}$, $10^{14} < N_M < 10^{18} \text{ cm}^{-2}$, and $1'' \leq \theta_s \leq 14''$, i.e. a beam dilution factor between 200 and 1. For the redshifted component, we find the best fit to be for a rotation temperature of 125 K, a column density of $4 \times 10^{17} \text{ cm}^{-2}$, and $\theta_s = 1''$, which is much smaller than the beam. The merit of this model can be seen in panel Fig. 3.4b. In this specific case the maximum optical depth encountered was $\tau = 6.8$. Because this seems to be the component with the highest column density, it is not surprising that $^{13}\text{CH}_3\text{OH}$ is detected in this component. Clearly, the highly excited K lines lead the model towards a high column density, but at the same time, the only way for the model to accommodate the lower K lines by increasing the optical depth is to decrease the source size. It should be noted, however, that this analysis assumes a single excitation temperature. We will discuss non-LTE modelling in Sec. 3.4.4.

3.4.3 Spatial distribution of the excitation

Maps of the derived rotation temperatures and column densities are presented in Figs. 3.5 and 3.6. In the maps we excluded the results of the -5.2 km s^{-1} velocity component seen at the position of HW2. The methanol rotation temperature ranges from $\sim 20 \text{ K}$ to $\sim 100 \text{ K}$ over most of the map, but shows a pronounced peak of $\geq 200 \text{ K}$ close to the HW2 position. We find column densities between 10^{15} cm^{-2} and $3 \times 10^{16} \text{ cm}^{-2}$. Overall, the methanol column density distribution is quite smooth and shows a minimum towards the centre position. In Sec. 3.4.4 we will investigate whether this minimum is an artefact of the rotation diagram method. Additionally, some care must be taken when analysing the results in the centre region. Only at the position of HW2 are we able to separate the two velocity components of the gas. In the neighbouring pixels the integrated line fluxes are therefore overestimated due to blending.

3 Distribution and excitation of thermal methanol in Cepheus A

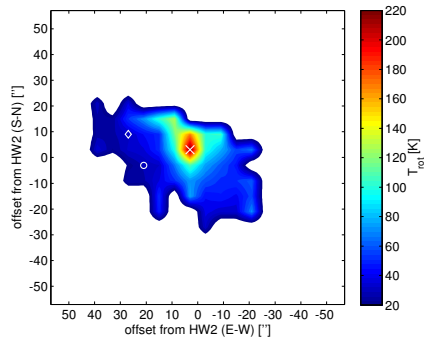


Figure 3.5: Map of derived rotation temperatures. Symbols are as in Fig. 3.3.

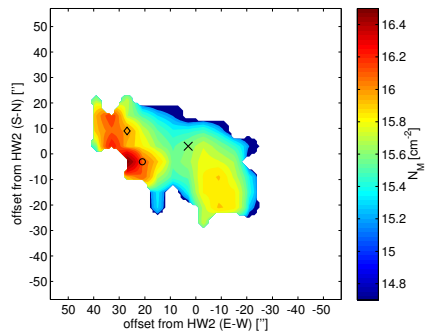


Figure 3.6: Map of derived column densities. Symbols are as in Fig. 3.3.

3.4.4 Non-LTE analysis

Method

To check the validity of the assumptions of the rotation diagram analysis, we ran a set of non-LTE models. By comparing the resulting synthetic spectra with the observed spectra, these models also allow us to investigate the physical conditions (i.e. temperature and density) at distinct positions in the methanol-emitting region. We used the RADEX² package, which uses statistical equilibrium for the population calculations and an escape-probability method to calculate the optical depth (van der Tak et al. 2007). The main assumptions are that the medium is uniform and that the optical depth is not too high (≤ 100). The most accurate collisional rates are available for the first 100 levels of methanol (Pottage et al. 2004, Schöier et al. 2005), and we therefore restrict this part of the analysis to the 24 relevant lines from Table 3.1.

Initial runs of the non-LTE model indicated that the methanol excitation is more strongly governed by the density than by the temperature. Using a uniform sphere geometry, we considered kinetic temperatures between 30 and 300 K and H₂ densities between 10^4 and 10^7 cm⁻³. Even at the lowest temperature all lines, except the $K=\pm 5$ and $K=\pm 6$ transitions, are excited in the high-density case. On the other hand, at low-density and high-temperature, only the lowest three K levels ($K=0, \pm 1, +2$) are populated. A combination of high temperature and high density is required to excite all lines, which renders this methanol band useful as a density and temperature tracer (Leurini et al. 2004).

Starting with model values comparable to the results from Sec. 3.4.1, it is possible to model the observed line strengths of the large-scale emission with the simple assumption that the emitting region is filling the beam. For these parameters all lines are optically thin ($\tau < 0.3$), which validates the assumption made in the rotation diagram analysis for the large-scale emission.

In the above calculations the background-radiation field was represented by the cosmic microwave background with $T_{\text{bg}}=2.73$ K. Models with background-radiation temperatures in the range 3 – 300 K were run, but this has no clear impact on the lines considered here. Mostly the contrast of the lines with respect to the background was reduced without changing their relative intensities. This result can be understood from the fact that our models consider only the torsional-vibrational ground state of methanol (Leurini et al. 2007). These models are inconclusive with regard to the influence of the radiation field, which is expected to be important in the maser region.

Non-LTE results

Then we used the non-LTE calculations to fit the spectra for the four regions identified in Sec. 3.3.2 (the velocity components at “Centre”, the “NE outflow”, and the quiescent gas in the “Envelope”). In a search for minima of the reduced χ^2 we used a model grid that includes column densities from 10^{13} to 10^{19} cm⁻² at every half dec, densities from 10^4

²<http://www.strw.leidenuniv.nl/~moldata/radex.html>

3 Distribution and excitation of thermal methanol in Cepheus A

Table 3.3: Results of the non-LTE models.

Position	$\Delta\alpha^a$ "	$\Delta\delta^a$ "	$\log(N_M)$ cm^{-2}	T_{kin} K	$\log(n_{\text{H}_2})$ cm^{-3}	T_{rad} K
Centre, main	+3	+3	16.0	90	4.0	30
Centre, red-shifted ^b	+3	+3	17.0	130	7.0	100
Outflow (NE)	+27	+9	15.0	90	5.0	30
Envelope	+21	-3	15.0	90	5.0	30

^a Offset from centre of map RA 22^h56^m17.88^s, DEC +62°01'49.2".

^b This component was modeled with a beam dilution factor of 50.

up to 10^9 cm^{-3} , kinetic temperatures between 30 and 300 K, and radiation temperatures in the range 3 – 400 K. Based on our findings in Sec. 3.4.1 we adopted a beam dilution factor of 50 for the redshifted emission in the “Centre”, corresponding to the 2" extent of the region where the masers appear. It is found that the models are able to reproduce the lines at all four positions to within 5-10% accuracy. In Fig. 3.7 we plot the observed integrated flux and the synthetic integrated flux calculated with RADEX versus $7_K \rightarrow 6_K$ number. Also indicated is our 3σ detection limit.

Like before, this analysis is complicated somewhat by the blending of lines by methanol and in the case of the $K=+1$ E by blending with SO_2 . For the $K=+1$ E line we did not include it in the analysis of the centre position components because the SO_2 contributes significantly to it. For the “NE outflow” and for the “Envelope” the SO_2 does not appear to contribute significantly, because the other SO_2 line is not detected, and we included it in the analysis. At the position of HW2 the methanol gas is highly excited, the blending of methanol lines becomes more severe and confusion prevents one from detecting the higher ($K \geq 5$) lines. Also, at this position the $K=\pm 2$ lines show a substantial ($\sim 50\%$) deviation from the RADEX model. The reason for this discrepancy is yet unclear, but could be another indication that we do not treat radiative processes completely.

The results of our non-LTE analysis are summarised in Table 3.3. The coolest and most diffuse gas is found in the envelope and outflow, where one should take into account that the granularity of the model grid probably prevents the distinction of small temperature and density differences. In comparison, the gas associated with the rotation temperature peak is much denser and also warm. We find the highest density and temperature in the “Centre” HW2 position where the maser emission occurs. However, given the large beam dilution and the limited set of available levels for collisional and radiative excitation, these numbers should be treated cautiously.

The non-LTE analysis confirms that there are no steep column density gradients across the source. But although generally the values agree with our rotation diagram analysis, they differ in details. In particular, the non-LTE analysis finds local maxima of the column density in the “Centre” components. Although the rotation diagram maps show some shortcomings for the inner components, they are useful for outlining the qualitative large-

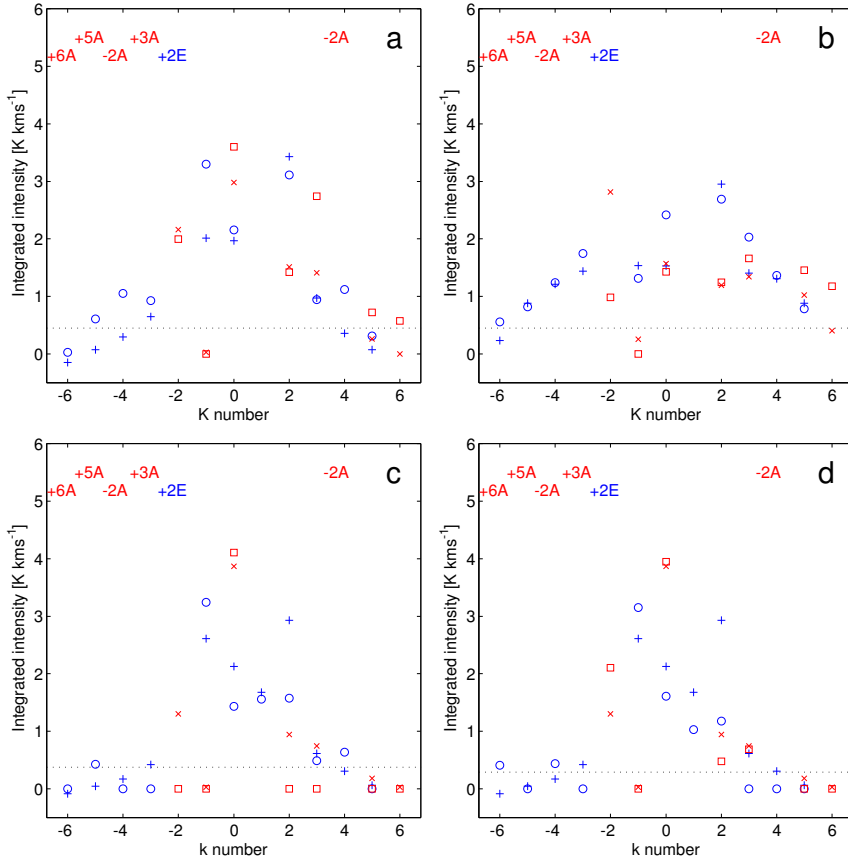


Figure 3.7: Plots of the integrated intensity for different $\text{CH}_3\text{OH } 7_K \rightarrow 6_K$ transitions and the best χ^2 model values. In the panels the observed flux (open symbols) is plotted, as well as the non-LTE model values (plusses and crosses). Also indicated is the 3σ detection limit. Circles and plusses (blue) are used for E-type lines and squares and crosses (red) for A-type. Labels on the top identify blended lines, for which the combined flux and model value are displayed. The $K=+1$ line which is blended with an SO_2 was not included in the analysis for the centre region components (top panels). The parameters of the fits are listed in Table 3.3. *a*: main, -10.5 km s^{-1} velocity component at the “Centre” position with beam dilution factor of 1, *b*: red-shifted, -5.2 km s^{-1} velocity component at “Centre” with a beam dilution factor of 50, *c*: the “NE Outflow” and *d*: “Envelope”.

3 Distribution and excitation of thermal methanol in Cepheus A

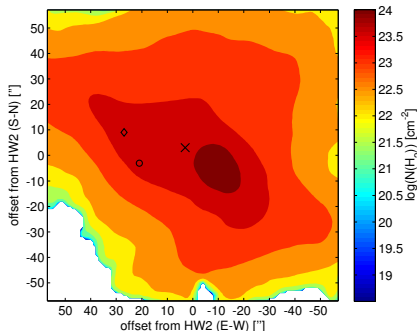


Figure 3.8: H₂ column densities derived from the SCUBA dust continuum for a constant dust temperature of 30 K.

scale properties and for constraining the distribution of the excitation; running pixel-based non-LTE models is beyond the scope of this chapter.

3.4.5 H₂ column density

To estimate the methanol abundance we require a measure of the H₂ column density to combine with the estimates of the methanol column density. Therefore we used the SCUBA map of Bottinelli & Williams (2004) and derived the H₂ column distribution using the formula of Henning et al. (2000) (eq. 3.2), where S_ν is the flux in units of Jy beam⁻¹, $\kappa_d(\lambda)$ the dust opacity at the observed wavelength, Ω_{mb} the solid angle of the main beam, $B_\nu(T)$ the Planck function (Black body), m_H the mass of the hydrogen atom, and R is the gas-to-dust ratio. In the calculation we used: $\kappa_d(875\mu\text{m}) = 1.4$ and $R=150$ (Henning et al. 2000).

$$N(H_2) = \frac{S_\nu}{\kappa_d(\lambda)\Omega_{mb}B_\nu(T)2m_H}R \quad (3.2)$$

The calculations were run for two cases. In the first case, we assumed a constant dust temperature of $T_d = 30$ K to derive the H₂ column density and the methanol abundance, X_M . In the second case we assumed the dust temperature T_d to be equal to the rotation temperature that we derived from the rotation diagram analysis in Sec. 3.4.1 and used that as input to the black-body function.

3.4.6 Methanol abundance

The results of the constant temperature hydrogen column density and methanol abundance calculations are presented in Figs. 3.8 – 3.9. The resulting hydrogen column density

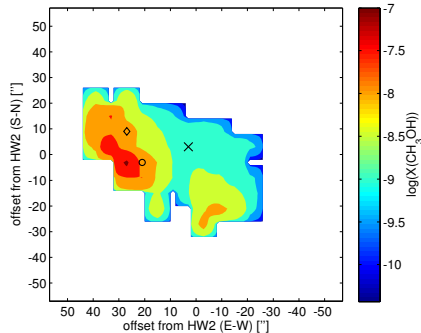


Figure 3.9: Methanol abundance derived from the methanol column densities obtained in the rotation diagram analysis and the H_2 column densities obtained for the constant dust temperature 30 K.

Fig. 3.8 is the SCUBA map (by Bottinelli & Williams (2004)) scaled by a constant factor to convert it from Jy beam^{-1} to $N(\text{H}_2)$ in cm^{-2} . The result is a very smooth map with H_2 column densities between $\sim 10^{21} \text{ cm}^{-2}$ and $\sim 10^{24} \text{ cm}^{-2}$. The general morphology of the dust emission is similar to that of the methanol gas, though notably the dust emission does not peak at the position of HW2, but closer to the SE at position $(-9'', -4'')$.

Similarly, the methanol abundance map derived with a constant dust temperature, Fig. 3.9, shows the same structure as the column density map, since there are no large variations in the SCUBA dust map. We derive a methanol abundance of $X_{\text{M}} \sim 10^{-8.5}$ for the central region. As noted before, the distribution is relatively flat and probably not very accurate for the centre position.

In the second case, when we used the methanol rotation temperature as a measure of the dust temperature, we find the resulting H_2 column density to be anti-correlated to the rotation temperature, because the high rotation temperatures derived for the centre region then result in a lower H_2 column. In this way we would derive a H_2 column of $\sim 10^{22} \text{ cm}^{-2}$ (much lower than inferred earlier $\sim 10^{24} \text{ cm}^{-2}$; Martín-Pintado et al. 2005). Although we already encountered the limited validity of the rotation diagram for the “Centre” region in Sec. 3.4.4, clearly there must be a mismatch between the gas and dust temperature on the scales of the JCMT maps. Both the rotation diagram and the non-LTE calculations indicate higher temperatures towards the centre, for which there is little evidence in the dust images, which even peak at an offset of $\sim 10''$ from the rotation temperature maximum. Besides the possibility that the rotation temperature is not a good estimate of the kinetic temperature of the gas, it seems plausible that the kinetic temperature of the gas is not equal to the dust temperature at these locations. Therefore, we adopt a constant dust temperature of 30 K to estimate the H_2 column density and CH_3OH abundance, realising that this method will overestimate $N(\text{H}_2)$ at the centre of the map.

3.5 Discussion

3.5.1 Outflow morphology

We have presented maps of the large-scale distribution of the thermal methanol associated with Cep A East (Figs. 3.3, 3.5, and 3.6). The emission is constrained to a region of size 0.29×0.15 pc ($85'' \times 43''$), roughly centred on the location of the radio continuum source HW2, the most massive YSO in the region. Moreover, the velocity field shows that the methanol gas is entrained in a large-scale bipolar outflow. The position angle of this outflow appears to be consistent with the HW2 geometry and earlier results (Gómez et al. 1999).

While the highest flux of the $K=-1$ E line Fig. 3.3a is associated with the receding part of the outflow (towards the SW), which is coincident with the SCUBA peak, the most energetic gas appears at the opposite side of HW2. This is evident already in the velocity width distribution of the brightest line, which has a line width of >4 kms, to the NE of HW2, Fig. 3.3c. It becomes clearer when the temperatures are derived from a rotation diagram analysis where the rotation temperature peaks to the NE of HW2 at ~ 200 K (Fig. 3.5).

Several authors (Patel et al. 2005, Jiménez-Serra et al. 2007, Torrelles et al. 2007) have inferred obscuring gas in a flattened circumstellar structure of $\sim 1''$ (700 AU) surrounding HW2. The gas shows signs of rotation and is perpendicular to the high-velocity outflow (~ 500 kms) seen in the radio continuum (Curiel et al. 2006). The molecular outflow that we observe in methanol is blueshifted to the NE, which implies that this side of the outflow is pointing towards the observer, Fig. 3.3b. In Chapter 2 we propose a model in which the methanol maser emission arises in a ring-structure in the equatorial plane of HW2. In contrast to the circumstellar molecular material, the masers do not show signs of rotation; rather the observations seem to indicate an infall signature. It is argued that the masers occur in the shock interface between the circumstellar disk and inflow regulated by a large-scale magnetic field (Vlemmings et al. 2010). We derive an inclination of 67.5° and a position angle of 9.3° for the ring in Chapter 2. The masing gas occurs on size scales of $\sim 2''$ and is very likely clumpy on smaller scales $\sim 0.1''$ (Minier et al. 2002). At the resolution of the observations presented in this chapter the masing gas clearly cannot be resolved, nevertheless the geometry that is observed on smaller scales suggests that to the NE of HW2 we have a line of sight into the outflow that probes highly excited gas close to the protostar, which explains why we see such a high rotation temperature in this region. Evidence for this wide-angle molecular outflow has recently been presented by Torrelles et al. (2010).

3.5.2 Methanol distribution

The highest methanol temperatures appear to occur close to the HW2 central source, but we demonstrated in Sec. 3.4.6 that the dust emission is not showing the same distribution. It seems plausible that the highest methanol rotation temperatures occur in a region

where the dust is at least partly destroyed, possibly at the onset of the outflow where the evaporation from the grains occurs that produces the methanol gas in the first place. The considerations on the dust distribution force us to adopt a constant dust temperature in our abundance analysis. On small radii this may have two effects: firstly, the gas-to-dust ratio may be higher because of grain destruction, which increases $N(\text{H}_2)$ and lowers the abundance. Secondly, the dust temperature may be higher than 30 K, which decreases $N(\text{H}_2)$ and increases the abundance. Increasing the gas-to-dust ratio from 150 to 200/250 decreases the abundance with a factor of 0.75/0.60 respectively. Increasing the dust temperature to 60/100/300 K increases the resulting abundance by a factor of 2.3/4.1/13.0 respectively. High optical depth of the dust will lower the derived abundance. These arguments show that at the peak rotation temperature, the methanol abundance is quite sensitive to increased dust temperatures, but is probably correct to within an order of magnitude, without taking beam-dilution effects into account.

The derived abundances of $\sim 10^{-8.5}$ are higher than expected from gas-phase chemistry, but lower than seen in the solid state (Gibb et al. 2004). High optical depth of the lines is ruled out by the excitation calculations, except in the central region. However, it is possible that there the local methanol abundance is still higher. For example, the methanol maser occurs on much smaller scales than those we are probing in these JCMT observations. The total extent of the CH_3OH maser is $\sim <2''$. Moreover, we found that the same small-scale enhancement can explain the peculiar excitation of the ‘‘Centre’’ region. This strengthens the idea that the highly excited methanol gas emission is coming from the same region. Assuming that the dust and the corresponding H_2 is smoothly distributed, this component can have a higher column density because of the optical depth and beam-dilution, resulting in methanol abundance estimate of $\sim 10^{-7}$ locally. This value is similar to previous values by other authors for maser regions (Menten et al. 1986, 1988) and still higher than expected from gas-phase chemistry and lower than seen in the solid state. Possibly the methanol evaporated from grain mantles some time ago (~ 1000 yr) and is now destroyed by chemical reactions and/or photo-dissociated.

As noted earlier, all the methanol gas seem to be entrained in an outflow, spanning 0.29 pc. The outflow is oriented close to the plane of the sky, assuming an inclination of 67.5° (Chapter 2) we find an outflow velocity of $\sim 5.8 \text{ km s}^{-1}$. The result implies a dynamical timescale of $\sim 2.4 \times 10^4$ yrs. The dynamical timescale agrees well with the chemical timescale (a few 10^4 years) for which such a methanol enhancement is believed to be possible (van der Tak et al. 2000a). This supports the argument of a common driving source for all the methanol gas in the region. Alternatively, the methanol may be released in the wake/outflow cavity of the jets described by Cunningham et al. (2009): the uv-radiation produced in the shock interface may shine back into the cavity and photo-desorb the methanol, which causes a local enhancement in the methanol column density.

3.5.3 Physical conditions

The rotation diagram analysis shows fairly warm gas entrained in a large-scale outflow. Although the non-LTE analysis demonstrates that the methanol band used in this study is

3 Distribution and excitation of thermal methanol in Cepheus A

quite sensitive to collisional excitation even in the low temperature regime, it qualitatively confirms the large-scale presence of warm methanol gas. Over large areas of the source the total methanol column density appears to be fairly constant at $\sim 10^{15} \text{ cm}^{-2}$, assuming a uniform distribution with unity beam-filling factor.

The fidelity of the rotation diagrams is breaking down particularly in the centre area, where higher excitation lines appear. Especially the red-shifted component requires non-LTE excitation and/or beam-dilution effects to be explained. At these locations a complete analysis requires high-resolution data and non-LTE modelling that includes excitation by infrared radiation. That more methanol levels should be taken into account is demonstrated by the detection of the torsionally excited $-1 \text{ A } v_t=1$ line at 337.969 GHz in the redshifted component (Leurini et al. 2007). Radiative pumping is also expected from models of methanol maser excitation (Cragg et al. 2005, Sobolev & Deguchi 1994, Sobolev et al. 1997)

3.5.4 Origin of maser emission

Although a wider area around Cep A has been searched for maser emission (Chapter 2), only one place in this source that is so abundant in methanol does show maser emission. We find the maser position to contain warmer gas than the other positions, to have probably the highest column density, and certainly the density appears to have a maximum here at $\sim 10^7 \text{ cm}^{-3}$. Moreover, this position does stand out as the position where a second kinematic component at -5.2 km s^{-1} is found. Special properties for this component are the detection of the torsionally excited line, and the requirement to invoke a large beam-dilution to explain the ratios of the higher excited lines. This dilution factor matches quite well with the size of the area of $< 2''$ over which masers are detected in Chapter 2 (Sugiyama et al. 2008b, Torstensson et al. 2011). Combining these facts, we identify this component with the origin of the maser action. We note that the densities we derive for this component are still below 10^9 cm^{-3} , where the maser lines would be quenched according to model calculations (Cragg et al. 2005). The models have methanol temperature ranges and methanol column densities that are consistent with our estimates, but it is hard to test the dust temperature, which must be $> 100 \text{ K}$ for the maser excitation. We note that many of the values estimated here are inferred indirectly and the relevant processes may occur on even smaller scales than reflected by the beam-dilution factor.

The central abundance of $X_M \sim 10^{-7}$ is not in excess to that found in low-mass star-forming regions, but the methanol column density $N_M \sim 10^{17} \text{ cm}^{-2}$ clearly is (Maret et al. 2005). This could point to the condition that the high-density, high-temperature region in low-mass star-forming regions is too small to produce a path length long enough, with sufficient methanol column density, to produce maser emission. Jørgensen et al. (2002) show the high-density, high-temperature region for a low-mass protostar to be $\sim 10\text{-}30 \text{ AU}$. In contrast, for a high-mass protostar, the region extends over $\sim 1000 \text{ AU}$ (Doty et al. 2002), which possibly facilitates the necessary amplification. Alternatively, Pandian et al. (2008) suggest that in low-mass stars the critical infrared pumping is only available in the inner region, where the density is so high that the maser will be quenched. Both effects

favour maser emission in the environments of high-mass protostars and explain that the masers occur on large distances from the central object, as found in Chapter 2.

To further constrain the physical conditions at the position of the methanol maser and discern radiation and density effects, high-J and $\nu_t = 1$ line observations are required, for example with the CHAMP+ instrument on the APEX telescope. To probe the excitation of methanol gas on small scales (comparable to that of the maser emitting region), high-resolution interferometry observations are needed, with instruments such as the SMA and the IRAM interferometers, and in the longer term, for lower declination sources, ALMA. The interpretation of these observations requires models that include the excitation of CH₃OH by infrared radiation.

Acknowledgements

The authors wish to thank an anonymous referee for comments that led to substantial improvements of the analysis methods and the robustness of the conclusions of this paper. This research was supported by the EU Framework 6 Marie Curie Early Stage Training programme under contract number MEST-CT-2005-19669 “ESTRELA”. WV acknowledges support by the *Deutsche Forschungsgemeinschaft* through the Emmy Noether Research grant VL 61/3-1.

Distribution and excitation of thermal methanol in 6.7 GHz maser bearing star-forming regions

II. A sample of 14 sources

Abstract

The 6.7 GHz CH₃OH maser is exclusively associated with high-mass star formation and this signpost allows us to do statistical studies of high-mass star-forming regions. CH₃OH is thought to originate from the icy mantles of dust grains and released in shocks. Furthermore, CH₃OH excited in massive young stellar objects shows a rich spectrum. To understand the origin of the CH₃OH maser emission, we map the distribution and excitation of the thermal CH₃OH emission in a sample of 12 relatively nearby (<6 kpc) high-mass star forming regions that are identified through 6.7 GHz maser emission. JCMT observations of the $J = 7 \rightarrow 6$ band at 338 GHz are used to image the line emission of 25 transitions, with upper energy levels between 65 and 390 K, over a 2' field at 14'' resolution. The images are velocity-resolved and allow us to study the kinematics of the regions. Further, rotation diagrams are created to derive rotation temperatures and column densities of the large scale molecular gas. The effects of optical depth and subthermal excitation are studied with population diagrams. For eight of the sources in our sample the thermal CH₃OH emission is confined to a region <0.4 pc and with a central peak close (<0.03 pc) to the position of the CH₃OH maser emission. Four sources have more extended thermal CH₃OH emission without a clear peak, and for the remaining two sources, the emission is too weak to map. The compact sources have linear velocity gradients along the semi-major axis of the emission of 0.3 – 13 km s⁻¹ pc⁻¹. The rotation diagram analysis shows that in general the highest rotation temperature is found close to the maser position. The population diagram analysis of the gas at the maser position does not show signs of large beam dilution effects, but indicates moderate optical depths of the lower- K lines which reduces our estimate of the excitation temperature. The confined and centrally peaked CH₃OH emission in the compact sources indicates a single source for the CH₃OH gas

4 Thermal methanol toward 6.7 GHz methanol maser sources

and the velocity fields show signs of outflow in all but one of the sources. The high detection rate of the torsionally excited $v_t = 1$ line and signs of high- K lines at the maser position indicate radiative pumping, though the general lack of measurable beam dilution effects may mean that the masing gas is not sampled well and originates in a very small region.

4.1 Introduction

In star-forming regions, maser action is commonly seen from various molecules (mostly OH, H₂O and CH₃OH ; sometimes NH₃; rarely SiO, H₂CO). Among these masers, the 6.7 GHz CH₃OH maser is unique because it is wide spread and exclusively associated with high-mass star formation (Minier et al. 2003, Xu et al. 2008). Much effort has gone into determining what physical component the maser emission traces (Norris et al. 1998, Pestalozzi et al. 2004, Minier et al. 2002, Bartkiewicz et al. 2005b). High resolution VLBI studies of the methanol masers indicate that they occur in physical structures on size scales of ~ 1000 AU, close to the protostar(s) (Bartkiewicz et al. 2009). Other studies are focussing on determining whether the masers trace a mass range or a particular time range in the evolutionary sequence by observing the spectral energy distribution (SED) of the central objects (Breen et al. 2010, Pandian et al. 2009).

CH₃OH is a versatile probe of the physical conditions in these regions, since it is sensitive to both the temperature and density due to its slight asymmetry. However, care must be taken when choosing which transitions to observe as different bands may trace different parameters. The $J = 7_K \rightarrow 6_K, \nu_t = 0$, band is sensitive to both temperature and density (Leurini et al. 2004). However, infrared pumping can mimic the excitation effects of high density in the $\nu_t = 0$ state. Therefore, to distinguish between infrared pumping and density the torsionally excited $\nu_t = 1$ state should ideally be observed too (Leurini et al. 2007). Maser models show that maser emission can occur over a range of specific conditions (Sobolev & Deguchi 1994, Sobolev et al. 1997, Cragg et al. 2005). The 6.7 GHz maser is the most commonly occurring and generally brightest among a number of CH₃OH maser transitions. For the infrared pumping to be effective, dust temperatures exceeding 100 K are required, and for maser emission velocity specific column densities between a few times 10^{11} and 10^{14} cm⁻³s are necessary. Furthermore, for densities $> 10^9$ cm⁻³ the maser is quenched by collisional de-excitation. To a lesser extent the gas temperature also influences the brightness temperature of the maser, with higher gas temperatures leading to a reduction of the brightness temperature.

Clearly for the maser emission to occur an enhanced (relative to pure gas-phase chemistry $\sim 10^{-11}$) CH₃OH abundance is required. The CH₃OH molecules form in the icy mantles of dust grains at low temperatures (~ 10 K) by hydrogenation of CO (Watanabe et al. 2003, 2004, Fuchs et al. 2009) and evaporate off the dust grains as they warm up at ~ 100 K (Collings et al. 2004). Alternatively, photo-desorption by UV photons may enhance the methanol abundance. As the protostar ignites and starts to ionise its environment the radiation will start to break down the methanol molecules. Therefore the methanol enhancement is thought to be very short (a few 10^4 years) and can serve as a chemical clock of the region (van der Tak et al. 2000a). The excitation of the 6.7 GHz methanol maser is through infra-red pumping and thus at least at the site of the methanol maser the radiation field cannot be neglected. To study the small scale distribution and excitation of the gas at the site of the methanol maser interferometric observations at mm and sub-mm wavelengths are required (e.g. Beuther et al. 2007b).

Ever since their discovery the 6.7 GHz methanol maser was found to be associated with high-mass star-formation because of its association with other maser species (OH

4 Thermal methanol toward 6.7 GHz methanol maser sources

and H₂O) and ultra-compact H II (UCHII) regions (Menten 1991a). Initial surveys targeted IRAS sources and other maser sites, though the detection rate was not always particularly high (Schutte et al. 1993, Gaylard & MacLeod 1993, Caswell et al. 1995, van der Walt et al. 1995, Szymczak et al. 2000). The first blind survey by Ellingsen et al. (1996) showed that many methanol masers were not exclusively associated with IRAS sources and had colours different from typical UCHII regions. More recent studies have shown that the 6.7 GHz maser is generally associated with mm dust continuum (> 95%) and much less frequently with cm emission (~ 25%) (Walsh et al. 1998, Beuther et al. 2002, Walsh et al. 2003, Hill et al. 2005). Breen et al. (2010) propose an evolutionary sequence in which, apart from the mm dust continuum, a weak 6.7 GHz CH₃OH maser is one of the first indicators of the high mass star-forming object. As the young star evolves and increases in luminosity, thus warming up its environment, the density decreases, and the brightness of the 6.7 GHz maser increases. After some 2×10^4 years a 12.2 GHz maser also forms and the source may be detectable in free-free emission at centimetre wavelengths. At this stage the OH maser turns on and after another 2×10^4 years the methanol masers disappear as the star continues to ionise its environment. Alongside the methanol masers water maser emission may be found in the outflow or shocked regions. Much effort is currently being spent on complete blind surveys of the 6.7 GHz methanol maser and follow-up programs (Green et al. 2010, Caswell et al. 2010, Pandian et al. 2011).

Our goal is to study the thermal methanol distribution and excitation in sources that exhibit 6.7 GHz methanol maser emission. We have started by studying the large scale characteristics of these regions. Consequently we have performed JCMT HARP-B observations of the $J = 7_K \rightarrow 6_K$, $v_t=0$, transition band of methanol at 338 GHz towards 13 sources with 6.7 GHz methanol masers, Table 4.1. The sources were initially selected from a sample of 12 relatively nearby, infrared bright 6.7 GHz sources studied at high resolution with the European VLBI Network (EVN). Due to scheduling constraints and to include a few more distant sources four other methanol maser sources mapped with the EVN were included from the sample of Bartkiewicz et al. (2009) even though their exact nature was uncertain at that point. The details of the observation procedure and data reduction are the same as for Cepheus A, described in Chapter 3. In this chapter we present the results of the remaining 13 sources and a statistical analysis of the complete sample.

4.2 Observations and data reduction

The JCMT¹ observations of the sources in this chapter were taken in 2007 and 2008 on the dates listed in Table 4.1 in the three observing programmes M07AN16, M07BN04, and M08AN10. We used the 16 element array receiver HARP and the observations were performed in a jiggle-chop mode (harp5) to create 2'×2' maps with a pixel spacing of 6". This ensures proper Nyquist sampling of the 14" JCMT beam at 338 GHz. During the observations regular pointings were done on calibrators and we estimate an absolute

¹The James Clerk Maxwell Telescope is operated by the Joint Astronomy Centre on behalf of the Science and Technology Facilities Council of the United Kingdom, the Netherlands Organisation for Scientific Research, and the National Research Council of Canada.

pointing accuracy of $\sim 1''$. In two cases, G23.657 and G24.541, the initial mapping scans showed the methanol emission to be constrained to a small area and very weak < 0.2 K, so for these two sources single pointing observations were done with the best receptor at the source.

The ACSIS correlator backend was set up with a bandwidth of 1 GHz (880 km s^{-1}) (at the time of the observations the 2 GHz bandwidth was not available) and 2048 channels centred on the $\text{CH}_3\text{OH } 7_0 \rightarrow 6_0 \text{ A}^+$ line at 338.41 GHz. The set-up covers 25 methanol lines in the $7_k \rightarrow 6_k$ band with a velocity resolution of 0.43 km s^{-1} , see Table 4.2 for details of the individual transitions. In our analysis we have adopted a main beam efficiency of 0.6 (Buckle et al. 2009) and estimate a calibration uncertainty of 20%.

The initial data inspection and re-gridding of the data was done with the Starlink package using Gaia/SPLAT after which the data were converted to GILDAS/CLASS format and the remaining data reduction and analysis was performed in CLASS. In order to increase the signal to noise of the spectra the data were smoothed to a velocity resolution of 0.87 km s^{-1} after which a linear baseline was fitted to the emission free regions of each spectra and subtracted. The analysis was then performed on a pixel by pixel basis in which the strongest unblended line in the spectra (-1E) was fitted with a Gaussian. The velocity of the -1E line was then used to calculate the velocities of the other 24 methanol lines. Around each calculated velocity the moments were calculated within a window size of two times the line width of the fitted -1E line.

The $\text{CH}_3\text{OH } +1\text{E}$ line is potentially blended with the $\text{SO}_2 20_{4,19} \rightarrow 19_{2,18}$ at 338.61 GHz. However, the $\text{SO}_2 18_{4,14} \rightarrow 18_{3,15}$ at 338.31 GHz, which has a similar line strength and upper level energy, is not detected in most of our spectra. Therefore the contamination of the CH_3OH line by SO_2 is probably small in these sources.

The observations of DR21 were initially performed in alt-az beam-switching. In this region the emission extends in the North-South direction resulting in the off beam switching into an area with methanol emission at the same or similar velocity as in the region of interest. The observing program was modified to switch in East-West direction instead. The absorption features caused by the off beam switching into emission have been inspected and do in the end not influence the measurements.

Like in Chapter 3 we continue with a rotation diagram analysis for all pixels with at least three lines above our 6σ detection limit, and we have used the first and second moment of the lines to help determine whether the line is an actual detection. The velocity of the line is not allowed to deviate more than 1 km s^{-1} from the expected line velocity as determined by the fitting of the -1E line. Similarly the second moment may not deviate from the measured line width of the -1E line by more than 1 km s^{-1} . In the case of the complex emission of DR21, we have accepted the first and second moments to deviate up to 2 km s^{-1} .

Table 4.1: Sources and observing details. The observing dates are in yymmdd format.

Source	RA (J2000)	DEC (J2000)	d (kpc)	Luminosity (L_{\odot})	Observing date
AFGL5142	+05:30:45.60	+33:47:52.0	1.8 ^a	4×10^3	070813
DR21(OH)	+20:39:00.40	+42:24:37.0	1.45 ^b	10^4	080730
G23.207-00.377	+18:34:55.20	-08:49:11.0	4.6 ^c	$< 10^4$	070617
G23.389+00.185	+18:33:14.33	-08:23:57.4	4.5 ^c	10^4	070617, 080731
G23.657-00.127	+18:34:51.56	-08:18:21.4	3.19 ^d	6×10^3	070617, 080801
G24.541+00.312	+18:34:55.72	-07:19:06.6	5.7 ^c	$< 10^4$	080729, 080730, 080802
G40.62-0.14	+19:06:01.609	+06:46:37.15	2.3 ^e	3×10^3	080622, 080729, 080731
G73.06+1.80	+20:08:10.10	+35:59:24.0	4.9 ^f	3×10^3	080729, 080730, 080731
G78.12+3.63	+20:14:26.1	+41:13:31	1.64 ^g	10^4	070708
L1206	+22:28:52.1	+64:13:43	0.776 ^h	900	070602, 070616, 070708, 080801
S255	+06:12:54.5	+17:59:20	1.59 ^h	2×10^4	080115
W3(OH)	+02:27:03.8	+61:52:25	1.95 ⁱ	8×10^4	070812

Notes: The coordinates are the actual observed coordinates and in the case of AFGL5142 the maser position is offset $\sim 30'$ to the East. ^aSnell et al. (1988), ^bRygl et al. (2011), ^cBartkiewicz et al. (2009), ^dBartkiewicz et al. (2008), ^eThis chapter, ^fMolinari et al. (2002), ^gMoscadelli et al. (2011), ^hRygl et al. (2010), ⁱXu et al. (2006).

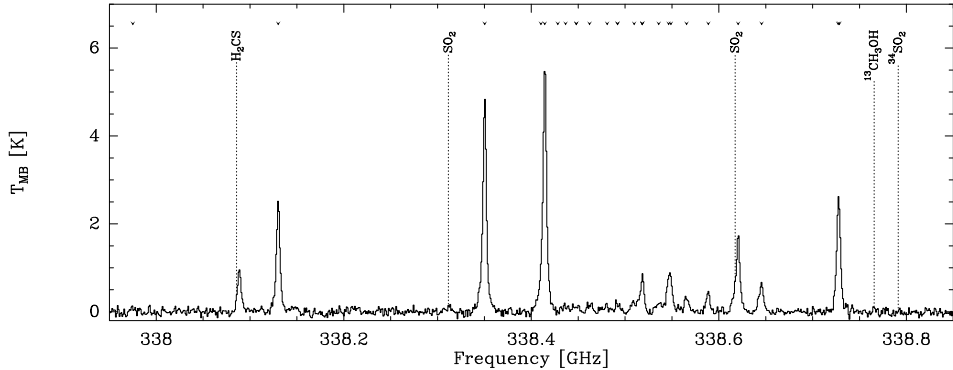


Figure 4.1: *AFGL 5142*: Spectrum of the maser position indicated in Fig. 4.2. The tick marks at the top indicate the frequencies of the methanol lines.

4.3 Results

In this section we discuss the results on the individual sources, starting with a brief background on the sources with emphasis on the aspects relevant for this chapter, like information on distance to the source, orientation, and occurrence of outflows etc. For each source the morphology of the $\text{CH}_3\text{OH} - 1\text{E}$ line emission is described and the results of the rotation diagram analysis are summarised in Table 4.3.

4.3.1 AFGL 5142

Observations of cm and mm continuum indicate that AFGL 5142 is a zero-age main sequence (ZAMS) B2 star with a luminosity of $4 \times 10^3 L_\odot$ (Zhang et al. 2002) at a distance of 1.8 kpc (Snell et al. 1988). Zhang et al. (2007) identify five mm continuum peaks (MM-1 – MM-5) and three cm continuum peaks (CM-1A, CM-1B, and CM-2) within $4''$. MM-1 and MM-2 appear to be more massive (both 4×10^3 to $7 \times 10^4 L_\odot$) and/or evolved than MM-3 – MM-5 although only MM-1 and MM-3 are associated with cm continuum emission. Molecular line observations of CH_3CN show that MM-2 ($v_{\text{LSR}} = -3.4 \text{ km s}^{-1}$) has a much higher temperature and column density than MM-1 ($v_{\text{LSR}} = -1.0 \text{ km s}^{-1}$) suggesting that MM-2 is in a more evolved state even though it is not associated with cm continuum emission (Zhang et al. 2007). The 6.7 GHz CH_3OH maser position is located between the two cm continuum peaks 1A and 1B associated with MM-1 (Goddi et al. 2007). Early CO(2-1) and CO(3-2) studies reveal an outflow in the North-South direction associated with the mm continuum emission, unresolved in single-dish data (Hunter et al. 1995). Interferometric imaging shows at least three different outflows associated with the mm continuum peaks. Zhang et al. (2007) identify the North-South outflow (A, $\text{PA}=5^\circ$) with MM-2, a second outflow (B, $\text{PA}=35^\circ$) with MM-3, and the third (C, $\text{PA}=-60^\circ$) with MM-1.

4 Thermal methanol toward 6.7 GHz methanol maser sources

Table 4.2: CH₃OH ($7_K \rightarrow 6_K$) line data for the observed transitions.

Frequency (MHz)	$\mu_g^2 S_g$ (D ²)	E_u (K)	Transition K type
337969.414	5.55	390.1	-1 A $\nu_r=1$
338124.502	5.65	78.1	0 E
338344.628	5.55	70.6	-1 E
338404.580	1.49	243.8	+6 E
338408.681	5.66	65.0	0 A
338430.933	1.50	253.9	-6 E
338442.344*	1.49	258.7	+6 A
338442.344*	1.49	258.7	-6 A
338456.499	2.76	189.0	-5 E
338475.290	2.76	201.1	+5 E
338486.337*	2.77	202.9	+5 A
338486.337*	2.77	202.9	-5 A
338504.099	3.80	152.9	-4 E
338512.627*	3.81	145.3	-4 A
338512.639*	3.81	145.3	+4 A
338512.856*	5.23	102.7	-2 A
338530.249	3.82	161.0	+4 E
338540.795*	4.60	114.8	+3 A
338543.204*	4.60	114.8	-3 A
338559.928	4.64	127.7	-3 E
338583.195	4.62	112.7	+3 E
338614.999	5.68	86.1	+1 E
338639.939	5.23	102.7	+2 A
338721.630	5.14	87.3	+2 E
338722.940	5.20	90.9	-2 E

Notes: All lines are from the $J = 7 \rightarrow 6$ band, and throughout the chapter a notation like “-6 E” refers to the $J = 7_{-6} \rightarrow 6_{-6}$ E transition. Blended lines are indicated by a *. Adopted from the CDMS (Cologne Database of Molecular Spectroscopy, Müller et al. (2005)).

4.3 Results

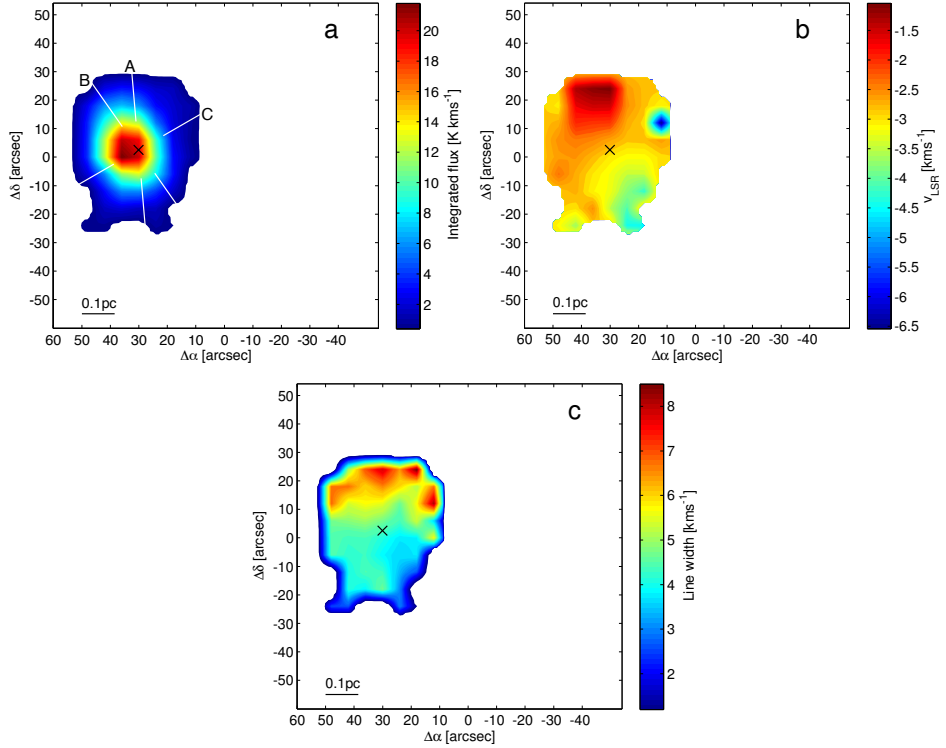


Figure 4.2: Integrated intensity (a), central velocity (b) and FWHM width (c) of the CH₃OH 7(-1) → 6(-1) E line observed toward AFGL 5142. The black cross marks the position of the 6.7 GHz maser and the outflow directions A, B, and C (Zhang et al. 2007) are indicated by the white lines.

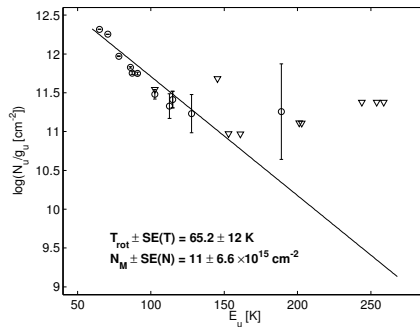


Figure 4.3: *AFGL 5142*: Rotation diagram of CH₃OH for the position of the maser.

4 Thermal methanol toward 6.7 GHz methanol maser sources

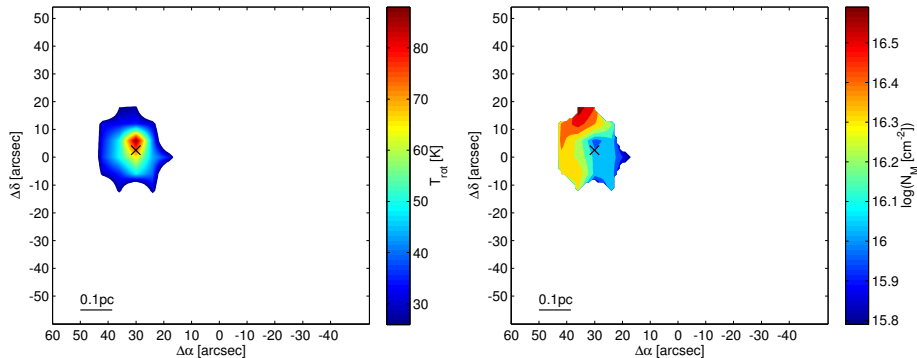


Figure 4.4: *AFGL 5142*: Maps of CH_3OH rotation temperature and column density.

The observations of *AFGL5142* were performed at the wrong coordinates (offset by $\sim 30''$) and therefore the maser (indicated by the black cross) and CH_3OH emission do not appear in the centre of the map. The CH_3OH emission (Figs. 4.2 a-c) is constrained to a roughly circular area with a clear peak intensity of the -1E line in the centre, close to the position of the methanol maser ($\Delta\alpha=+30.1''$, $\Delta\delta=+2.6''$). The velocity map shows a bipolar velocity field with redshifted velocities to the NE and blueshifted velocities to the SW. The blueshifted spot to the NW of the maser position is probably not significant. The line width map indicates that the line widths are larger to the North than to the South, however this may be due to lower signal-to-noise to the North.

The spectrum from the maser position in *AFGL5142* (Fig. 4.1) shows that lines up to $K=3$ are detected. There is no detection of the vibrationally excited line ($v_t = 1$). There is some SO_2 emission, but it is at most 10% of the $K=+1\text{E}$ flux and it is offset in velocity. Since we only integrate an area two times the line width the contribution of SO_2 to the $K=+1\text{E}$ flux is negligible. Therefore we include the $K=+1\text{E}$ line in the analysis. We find rotation temperatures between 26.0 and 88.5 K, and column densities between 6.3×10^{15} and $4.0 \times 10^{16} \text{ cm}^{-2}$ across the map. The highest rotation temperatures are associated with the position of the methanol maser, Fig. 4.4a. There seems to be a column density gradient across the source with higher column densities associated with the redshifted emission to the NE and lower column densities associated with the blueshifted emission to the SW, Fig. 4.4 b.

4.3.2 DR21 (FIR1 & FIR2)

DR21(OH)N is part of the *DR21-W75* filament in the Cygnus X region. The complex has a parallax distance of 1.45 kpc (Rygl et al. 2011) and the dense massive core (C160) that both *FIR1* and *FIR2* are associated with has a total luminosity of $1.1 \times 10^4 L_\odot$ (Roy et al. 2011). The massive core consists of five mm clumps and the 6.7 GHz CH_3OH masers *FIR1* and *FIR2* are associated with the clumps *N43* and *N51* respectively (Motte et al.

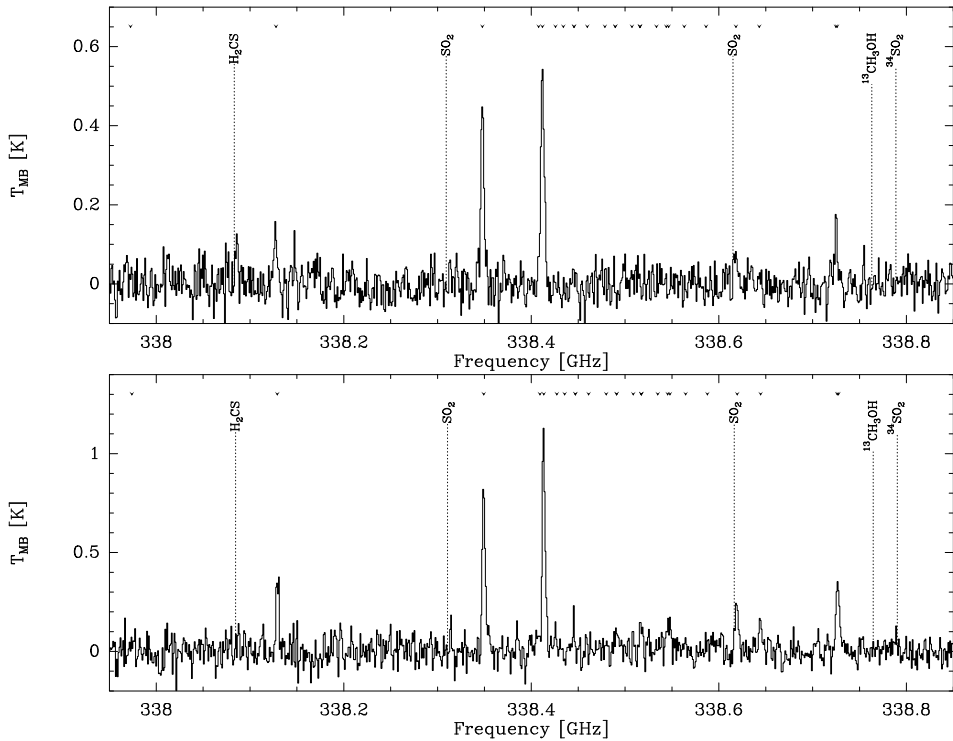


Figure 4.5: *DR21:* *Top:* Spectrum of the FIR1 maser position. *Bottom:* Spectrum of the FIR2 maser position. The tick marks at the top indicate the frequencies of the methanol lines.

4 Thermal methanol toward 6.7 GHz methanol maser sources

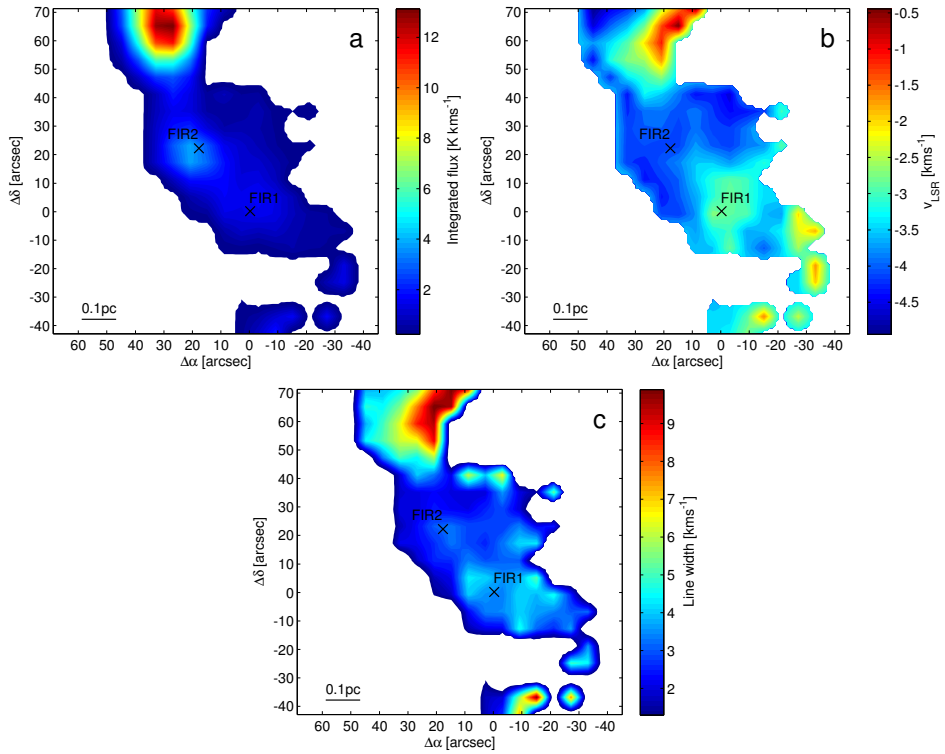


Figure 4.6: As Fig. 4.2 for the source DR21.

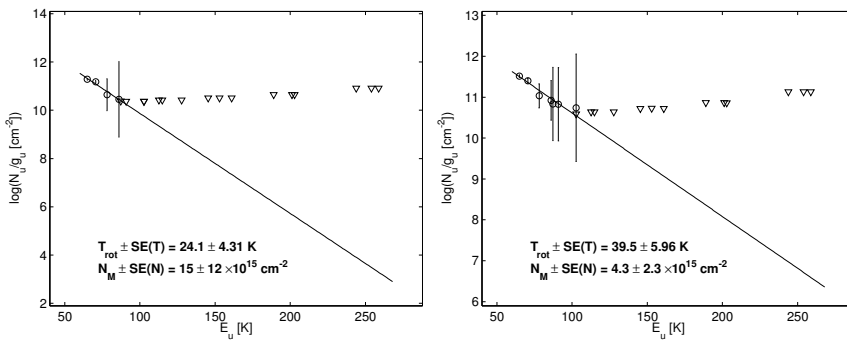


Figure 4.7: DR21: Rotation diagrams of CH₃OH for the positions of the masers. *Left:* FIR1. *Right:* FIR2.

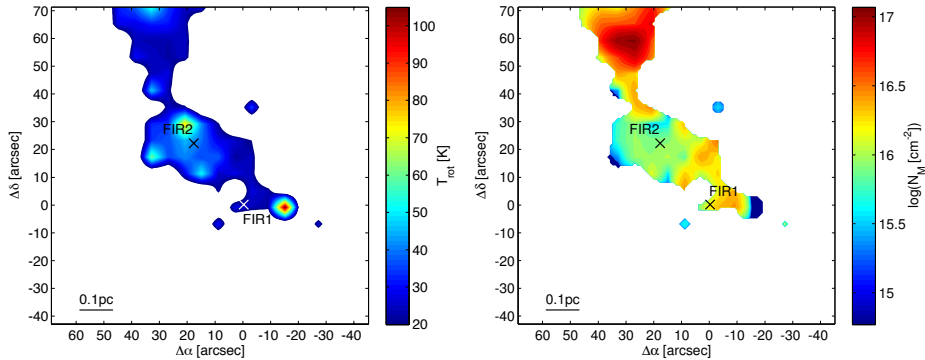


Figure 4.8: *DR21*: Maps of CH_3OH rotation temperature and column density.

2007). The source FIR1 has a luminosity of $\sim 1400 L_{\odot}$ (Chandler et al. 1993). Several molecular outflows have been observed as well as multiple H_2 knots (Davis et al. 2007, Schneider et al. 2010, 2006).

In DR21, the $\text{CH}_3\text{OH} -1\text{E}$ line emission shows that the emission extends in a large structure from South to North with the brightest emission to the North, Figs. 4.6 a-c. The two maser positions FIR1 ($\Delta\alpha = -0.3''$, $\Delta\delta = +0.1''$) and FIR2 ($\Delta\alpha = +17.6''$, $\Delta\delta = +22.3''$) are located in the central region of the map. The velocity field map is complex and does not show any clear indication of a simple velocity gradient in the area of the maser emission. The line width map shows a maximum in the North in the region of the source FIR3 (Motte et al. 2007), the lines in this area of the map are asymmetric.

The spectra of the two maser regions FIR1 and FIR2 (Fig. 4.5) show that lines up to $K=1$ and $K=2$ are detected. The $\nu_t = 1$ line is not detected. We do not observe any SO_2 emission at either position and therefore include the $+1\text{E}$ line in the rotation diagram analysis. In the rotation diagram analysis we use a SNR cut-off of 4 and a maximum velocity and width difference of 2 km s^{-1} between the expected velocity/width and the calculated moments. However, because we focused on the maser positions during the observations, the emission to the North, where the lines are not Gaussian cannot be analysed properly.

The results of the rotation diagram analysis are illustrated by the rotation temperature and column density maps (Figs. 4.8 a-b). There is a rotation temperature maximum close to the source DR21 FIR2. In contrast, no enhanced rotation temperature is seen at the position of FIR1. The column density map shows an enhanced column density to the North of both maser sources but does not show any enhancement at either of the positions of the two masers.

4.3.3 G23.207–00.377

The source G23.207–00.377 has a MIR counterpart, and is associated with water masers, although no radio continuum has been detected (Bartkiewicz et al. 2011). Its distance is

4 Thermal methanol toward 6.7 GHz methanol maser sources

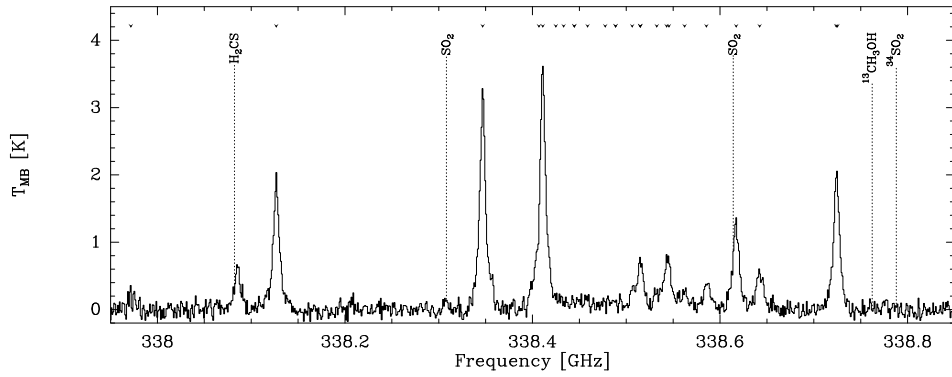


Figure 4.9: *G23.207–00.377*: Spectrum of the maser position.

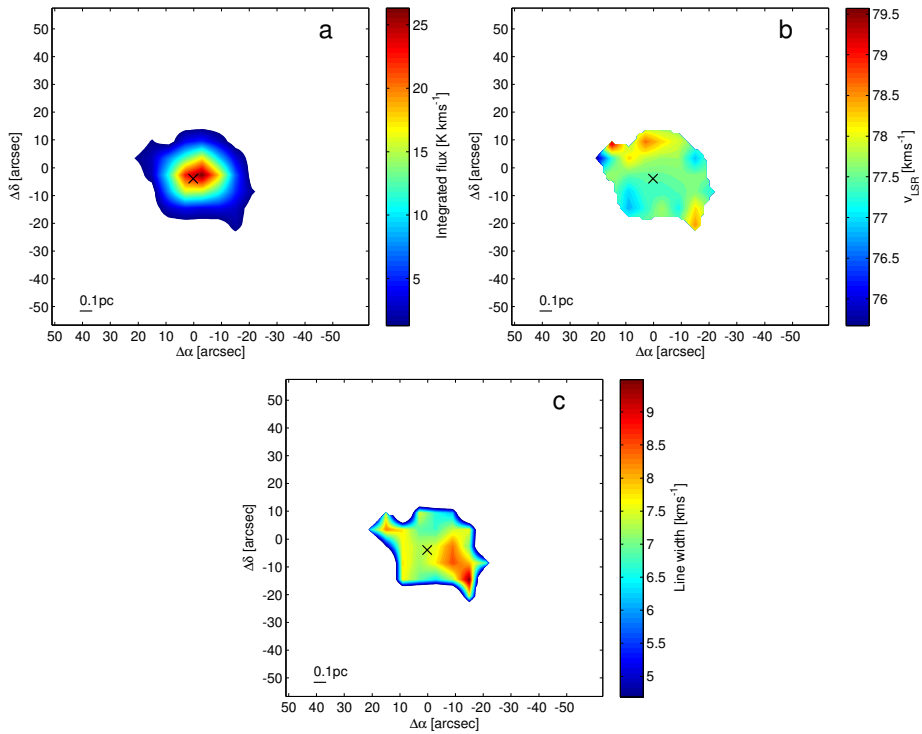


Figure 4.10: As Fig. 4.2 for the source *G23.207–00.377*.

4.3 Results

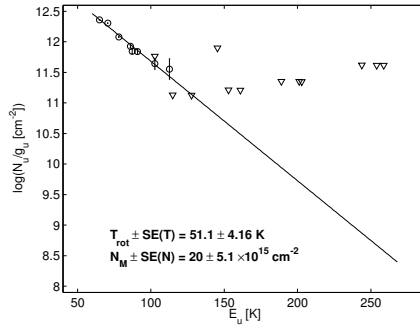


Figure 4.11: *G23.207–00.377*: Rotation diagram of CH_3OH for the maser position.

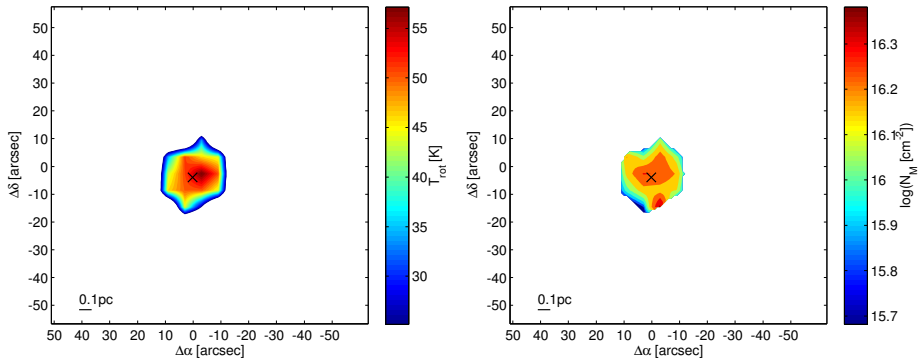


Figure 4.12: *G23.207–00.377*: Maps of CH_3OH rotation temperature and column density.

4 Thermal methanol toward 6.7 GHz methanol maser sources

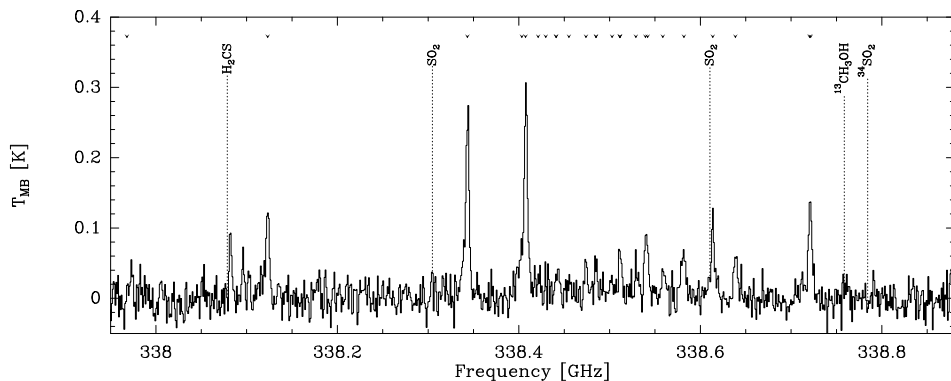


Figure 4.13: *G23.389+00.185*: Average spectrum of the four centre pixels of the maser position. The tick marks at the top indicate the frequencies of the methanol lines.

estimated to 4.6 kpc by Bartkiewicz et al. (2009) based on the kinematic distance model of Reid et al. (2009b). Using the IRAS fluxes we have estimated the luminosity of the source to $< 10^4 L_{\odot}$ using eq. 3 in Walsh et al. (1997), though the non-detections at 60 and $100 \mu\text{m}$ make not only the luminosity uncertain, but also its identification as a high-mass star-forming region.

The $\text{CH}_3\text{OH} - 1\text{E}$ line emission in *G23.207-00.377* (Figs. 4.10) is confined to within $20''$ radius from the source with a clear maximum in the centre of the map close to the position of the maser ($\Delta\alpha=+0.2''$, $\Delta\delta=-3.9''$). The maps of the velocity field and the line width do not show a clear structure, probably as a result of a low signal-to-noise ratio.

The spectra of the maser position (Fig. 4.9) show that lines up to $K=2$ are detected. There is also an emission feature tentatively identified with the $\nu_t = 1$ line. The SO_2 emission is weak and we have therefore included the $k=+1\text{E}$ line in the analysis. The rotation temperature and column density of the maser position are reported in Table 4.3. Similar to the $\text{CH}_3\text{OH} - 1\text{E}$ line flux, both the rotation temperature and column density in *G23.207-00.377* (Figs. 4.12 a-b) show a maximum close to the position of the maser.

4.3.4 *G23.389+00.185*

G23.389+00.185 has a near kinematic distance of 4.5 kpc, it has a MIR counterpart and a luminosity of $10^4 L_{\odot}$ (Bartkiewicz private communication). It is associated with water maser emission though no radio continuum emission has been detected (Bartkiewicz et al. 2011, 2009).

In *G23.389+00.185* the CH_3OH emission is compact and confined to the central area with a clear maximum at the position of the maser ($\Delta\alpha=+0.0''$, $\Delta\delta=0.0''$), Figs 4.14 a-c. The velocity field map shows sign of a velocity gradient of $1.4 \text{ km s}^{-1} \text{ pc}^{-1}$ across the source with redshifted emission to the SE and blueshifted emission to the NW. The line width map does not show any features of particular interest.

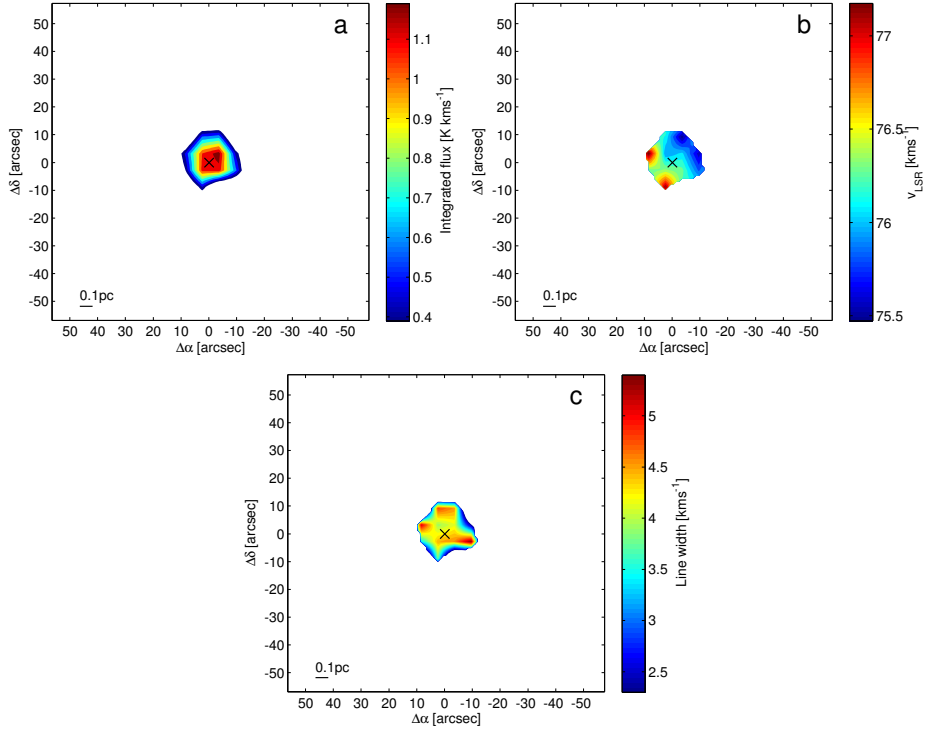


Figure 4.14: As Fig. 4.2 for the source G23.389+00.185.

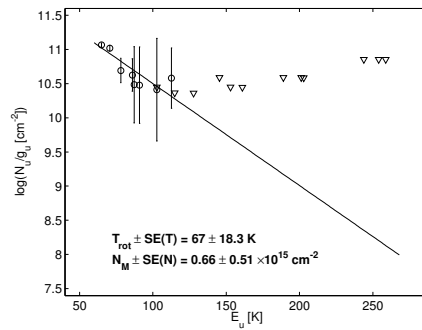


Figure 4.15: G23.389+00.185: Rotation diagram of the four averaged pixels at the position of the maser.

4 Thermal methanol toward 6.7 GHz methanol maser sources

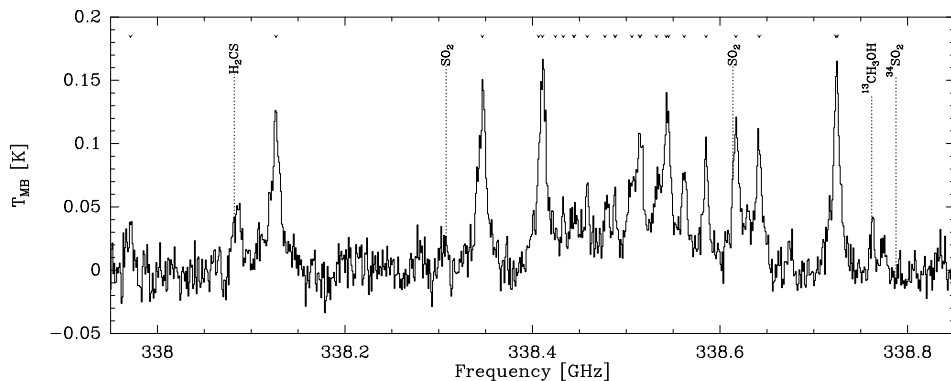


Figure 4.16: *G23.657–00.127*: Spectrum at the maser position. The tick marks at the top indicate the frequencies of the methanol lines.

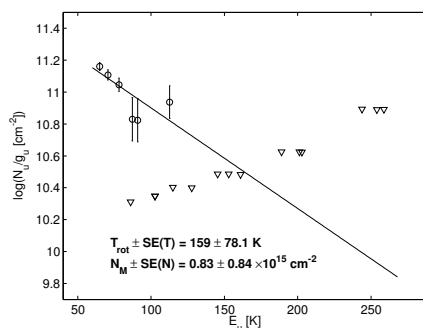


Figure 4.17: *G23.657–00.127*: Rotation diagram of CH_3OH for the position of the maser.

The extent of the CH_3OH emission is small and to improve the signal to noise the four centre pixels are averaged. The averaged spectrum (Fig. 4.13) shows the detection of lines up to $K=2$. There is a weak emission feature in the spectrum close to the frequency of the $\nu_t = 1$ line. The SO_2 line is not detected and consequently the +1E line is included in the analysis. We find a rotation temperature of 67 K and a methanol column density of $6.6 \times 10^{14} \text{ cm}^{-2}$.

4.3.5 G23.657–00.127

The conspicuous ring source *G23.657–00.127*, characterised by its ring-distribution of 6.7 and 12.2 GHz CH_3OH maser emission, has a parallax based distance estimate of 3.19 kpc (Bartkiewicz et al. 2008, 2005b), considerably closer than its (near) kinematic distance of ~ 5 kpc. It has an infrared counterpart and its SED suggests a luminosity of

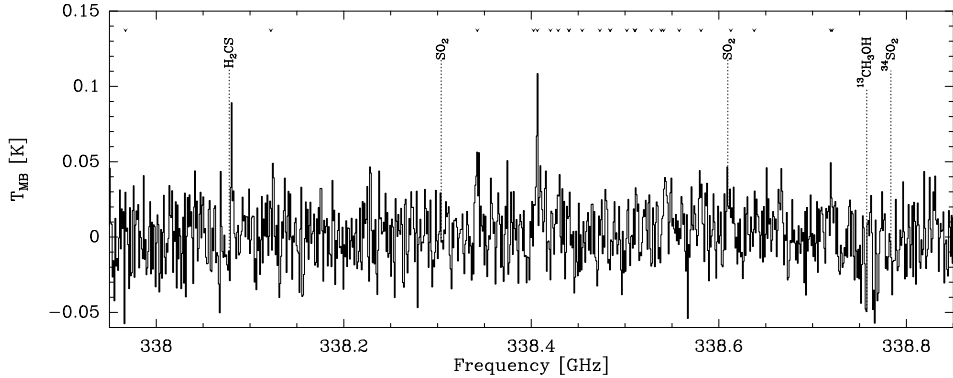


Figure 4.18: *G24.541+00.312*: Spectrum of the maser position. The tick marks at the top indicate the frequencies of the methanol lines.

$6 \times 10^3 L_{\odot}$ (Bartkiewicz, priv. communication), equivalent to a single B1 ZAMS star (Panagia 1973). The source does not have water maser or radio continuum emission association (Bartkiewicz et al. 2009, 2011).

The CH_3OH emission in *G23.657-00.127* is weak and compact and we are therefore unable to map the distribution as we have done for the other sources. Instead the source was observed in a single pointing mode in which the receptor was centred on the position of the maser emission for a deep integration. The resulting spectrum (Fig. 4.16) is complex and suffers from line blending. Because of the line blending only lines up to $K=2$ are included in the analysis, though higher K lines contribute to the spectrum. Also the $v_t = 1$ line is detected. There may be some SO_2 emission but it does not seem to contribute significantly to the measured CH_3OH flux and the +1E line is therefore included in the analysis. We find a rotation temperature of ~ 160 K and a column density of $\sim 10^{15} \text{ cm}^{-2}$, however, there appears to be multiple velocity components that we are unable to separate and therefore the complexity of the spectrum violates the assumptions we use for the statistical approach in this chapter. In the rotation diagram (Fig. 4.17) several of the lines have upper limits below the fitted line, but we have chosen to disregard these because of the line blending.

4.3.6 *G24.541+00.312*

G24.541+00.312 has a near kinematic distance of 5.70 kpc. It has a MIR counterpart but no close association with water masers or detected radio continuum (Bartkiewicz et al. 2009, 2011). The source luminosity is estimated in the same manner as for *G23.207-00.377*, Sec. 4.3.3. We find a luminosity of $< 10^4 L_{\odot}$ though the non-detections at 60 and $100 \mu\text{m}$ make not only the luminosity uncertain, but also its identification as a high-mass star-forming region.

Also in *G24.541+00.312* the CH_3OH emission is weak < 0.1 K and unresolved, and

4 Thermal methanol toward 6.7 GHz methanol maser sources

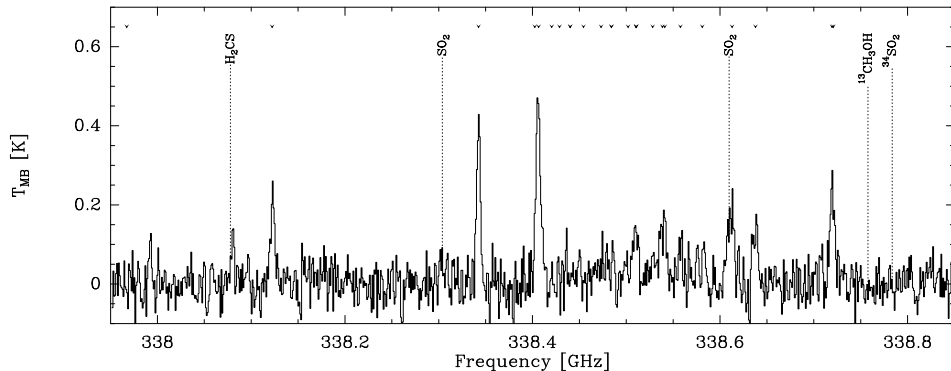


Figure 4.19: *G40.62–0.14*: Spectrum of the maser position.

after the initial mapping attempts the single pointing mode was used to acquire the data. Due to the poor signal to noise we have excluded this source from the analysis and only show the spectrum here for completeness, Fig. 4.18.

4.3.7 G40.62–0.14

In recent literature two different distances for G40.62–0.14 are used: 2.2 kpc (López-Sepulcre et al. 2010) and 10.5 kpc (Pandian et al. 2009). To be consistent we have calculated the kinematic distance using the model of Reid et al. (2009b). We find a kinematic distance of 2.3 kpc, similar to the distance adopted by López-Sepulcre et al. (2010) and the source has a luminosity of $2.5 \times 10^3 L_{\odot}$ scaled from the kinematic far distance (Pandian et al. 2009, 2010). The source has a $\sim 30''$ bipolar molecular outflow oriented SE (blue) - NW (red) (López-Sepulcre et al. 2010). The radio continuum source is detected at 1.3 cm and 6.9 mm, but not at 3.6 cm, which indicates that it may be a hyper-compact (HC) HII region. There is a second cm/mm source nearby ($\sim 2''$) consistent with an UCHII region (Pandian et al. 2010).

The $\text{CH}_3\text{OH} - 1\text{E}$ line emission in G40.62–0.14 (Figs. 4.20 a-c) is compact, and constrained to the centre of the map with a maximum near the position of the methanol maser ($\Delta\alpha=+0.1''$, $\Delta\delta=+0.1''$). The velocity map shows a velocity gradient with blueshifted emission to the SE and redshifted emission to the NW, consistent with previous observations (López-Sepulcre et al. 2010). To the SE of the maser position, in the blueshifted area, there is a maximum in the line width map, though it may be due to poor signal to noise.

The spectrum of the maser position (Fig. 4.19) shows that lines up to $K=2$ are detected. Higher- K lines and the $\nu_1 = 1$ line are not detected. SO_2 is detected and seems to contribute a significant amount of flux to the +1E line and we have therefore excluded this line from the analysis. The results of the rotation diagram analysis at the maser position are listed in Table 4.3.

4.3 Results

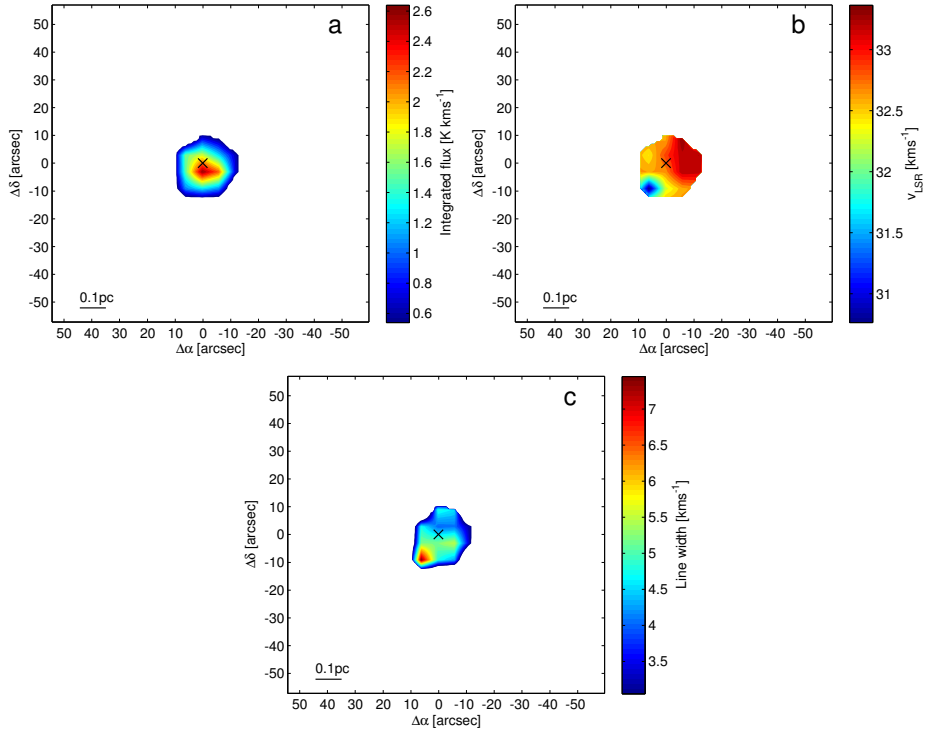


Figure 4.20: As Fig. 4.2 for the source G40.62–0.14.

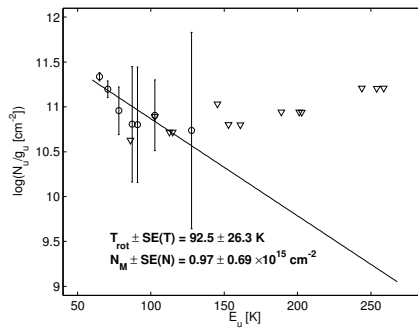


Figure 4.21: *G40.62–0.14*: Rotation diagram of CH₃OH at the position of the maser.

4 Thermal methanol toward 6.7 GHz methanol maser sources

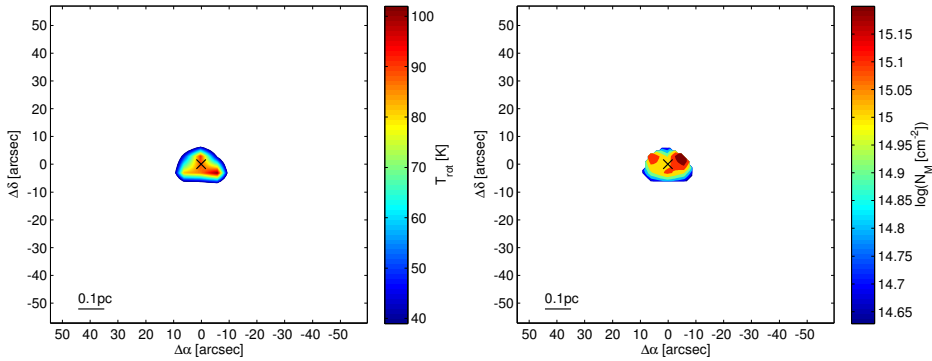


Figure 4.22: *G40.62–0.14*: Maps of CH₃OH rotation temperature and column density.

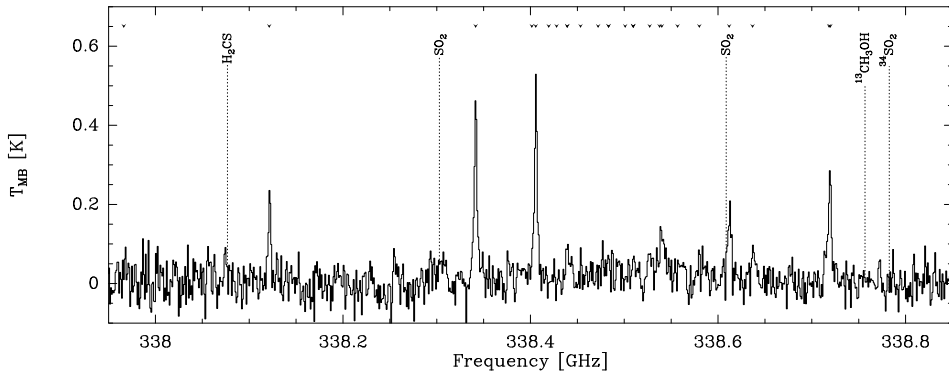


Figure 4.23: *G73.06+1.80*: Spectrum of the maser position. The tick marks at the top indicate the frequencies of the methanol lines.

4.3.8 G73.06+1.80

G73.06+1.80 has a luminosity of $3.2 \times 10^3 L_{\odot}$ at a kinematic distance of 4.9 kpc (Molinari et al. 2002), and is associated with both methanol and water masers. Although it shows a complex velocity field in HCO⁺ it also has a bipolar outflow seen in CO, infrared, and H₂ (Zhang et al. 2005, Varricatt et al. 2010). The outflow is oriented NE (blue) - SW (red) and seems to originate from a faint infrared source $< 0.5''$ from the methanol maser position (Chapter 5).

In *G73.06+1.80* the CH₃OH –1E line maps (Figs. 4.24 a-c) show that the emission is compact and constrained to the centre of our map with a maximum close to the maser position ($\Delta\alpha=+0.1''$, $\Delta\delta=+0.1''$). The velocity map shows a gradient with blueshifted emission to the E and redshifted emission to the W. The redshifted emission to the W is however associated with a maximum in the line width map and the single data point

4.3 Results

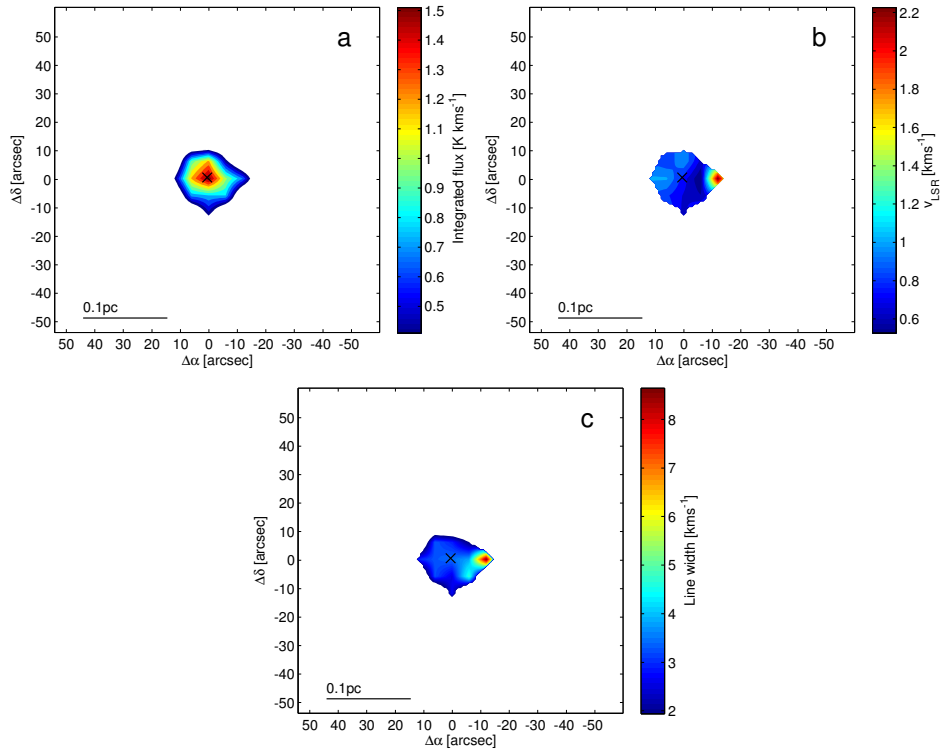


Figure 4.24: As Fig. 4.2 for the source G73.06+1.80.

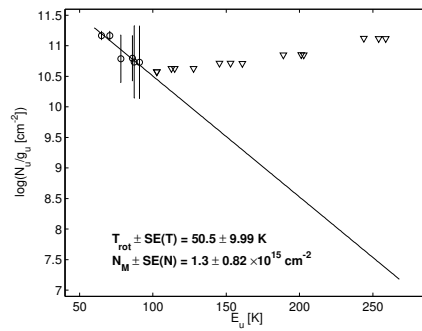


Figure 4.25: *G73.06+1.80*: Rotation diagram of CH₃OH for the position of the maser.

4 Thermal methanol toward 6.7 GHz methanol maser sources

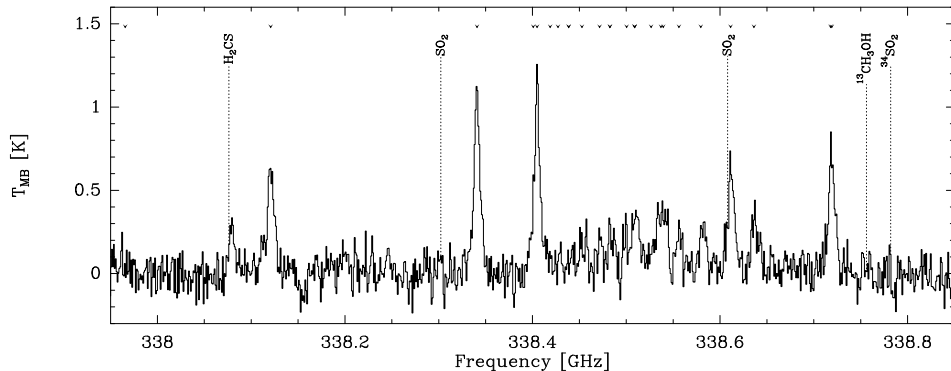


Figure 4.26: *G78.12+3.63*: Spectrum of the maser position. The tick marks at the top indicate the frequencies of the methanol lines.

responsible for it seems to be due to poor signal to noise.

The spectrum of the maser position (Fig. 4.23) shows that lines up to $K=2$ are detected. The contribution of SO_2 to the +1E line flux does not seem to be significant and we have included the line in the analysis. The signal to noise of our data does not allow us to map the excitation and only for the centre pixel can we perform a rotation diagram analysis, Fig. 4.25.

4.3.9 G78.12+3.63

G78.12+3.63 (IRAS 20126+4104) has been studied extensively at many different wavelengths, see Varricatt et al. (2010) for a recent comprehensive review. The object has a luminosity of $10^4 L_\odot$ at a parallax distance of 1.64 kpc (Moscadelli et al. 2011). It has a molecular outflow that extends ~ 0.4 pc oriented to the NW (red) - SE (blue). At the origin of the outflow mm continuum emission is associated with a Keplerian disk seen in several molecular species, the disk is oriented roughly perpendicular to the outflow (Cesaroni et al. 1999, 2005).

The $\text{CH}_3\text{OH} - 1\text{E}$ line emission in *G78.12+3.63* is constrained to the centre of the map and elongated in the SE/NW direction (Figs. 4.27a-c), consistent with the thermal CH_3OH being part of the molecular outflow. The integrated flux map shows a maximum close to the position of the methanol maser ($\Delta\alpha=-0.6''$, $\Delta\delta=+1.7''$). There is a clear velocity gradient of $13.1 \text{ km s}^{-1} \text{ pc}^{-1}$ in the direction of the outflow with blueshifted emission to the SE and redshifted emission to the NW. The line width map shows a maximum to the SE, associated with the blueshifted emission.

The spectra from the centre region (Fig. 4.26) are complex and suffer from line blending. The $v_t = 1$ is not detected but the flux from the SO_2 line in the centre region has led us to exclude the +1E line from the analysis. Lines up to $K=2$ are detected, though from the rotation diagram (Fig. 4.28) it is clear that the high- K line strengths are over estimated

4.3 Results

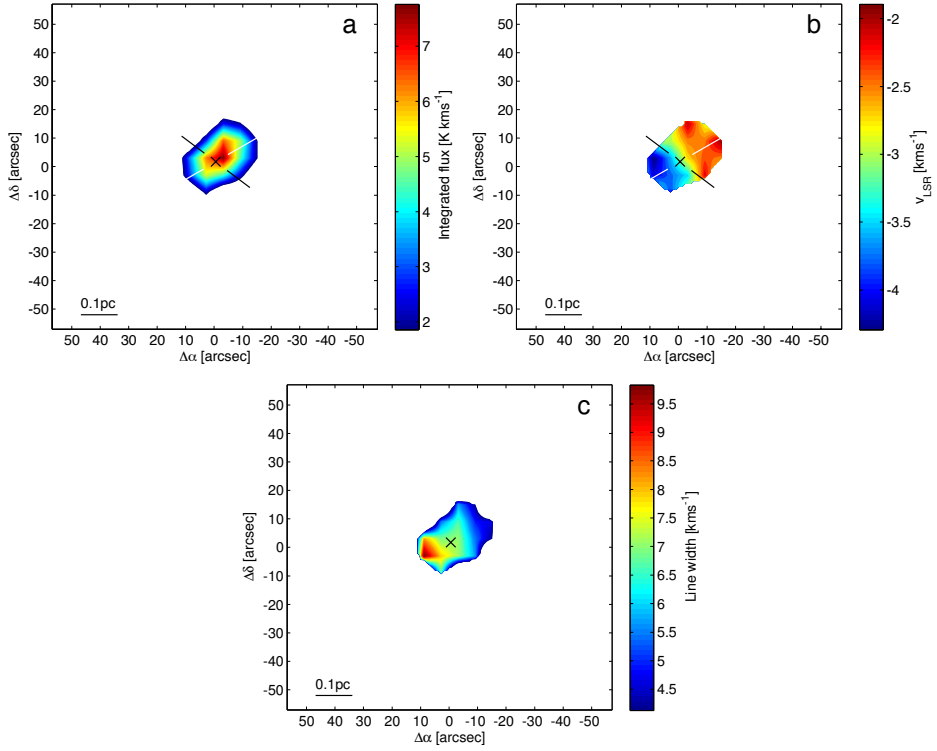


Figure 4.27: As Fig. 4.2 for the source G78.12+3.63. The white line indicates the direction of the outflow and the black line that of the disk (Cesaroni et al. 2005).

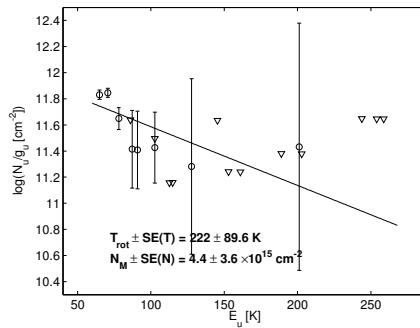


Figure 4.28: G78.12+3.63: Rotation diagram of CH_3OH for the position of the maser.

4 Thermal methanol toward 6.7 GHz methanol maser sources

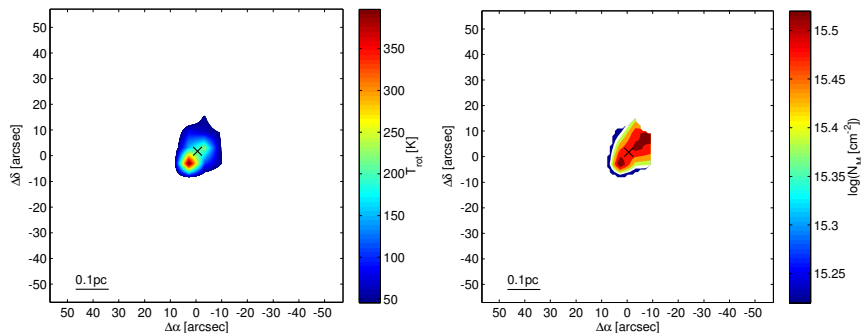


Figure 4.29: *G78.12+3.63*: Maps of rotation temperature and column density.

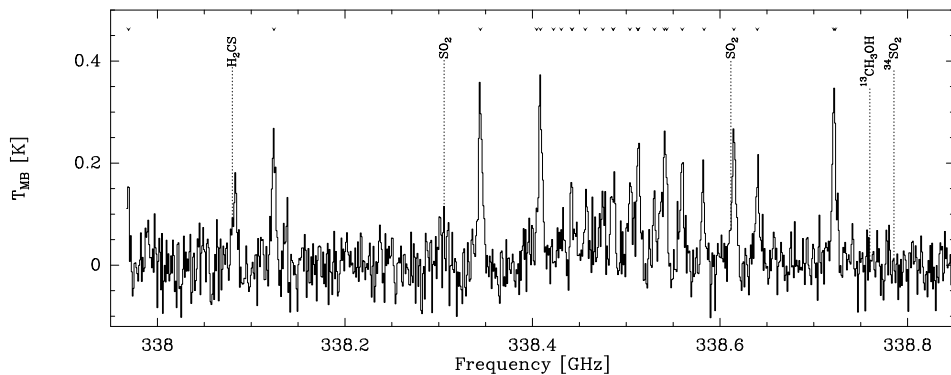


Figure 4.30: *L1206*: Spectrum of the maser position. The tick marks at the top indicate the frequencies of the methanol lines.

and we consider the rotation temperature as an upper limit. The rotation temperature shows a maximum associated with the blueshifted emission to the SE of the maser position (Fig. 4.29a). The column density map shows an enhancement both to the SE and to the NW of the maser position (Fig. 4.29b).

4.3.10 L1206

L1206 has a luminosity of $900 L_{\odot}$ scaled to the parallax distance of 776 pc (Rygl et al. 2010). It has a systemic velocity of $v_{\text{LSR}} = 11 \text{ km s}^{-1}$ measured in C^{18}O ($J = 1 \rightarrow 0$) and HC_3N ($J = 12 \rightarrow 11$) and a CO outflow (PA=140°) with blueshifted emission to the NW and redshifted emission to the SE (Beltrán et al. 2006). This is opposite to what we see in our velocity cut along the major axis. It could be consistent with our measurement of the

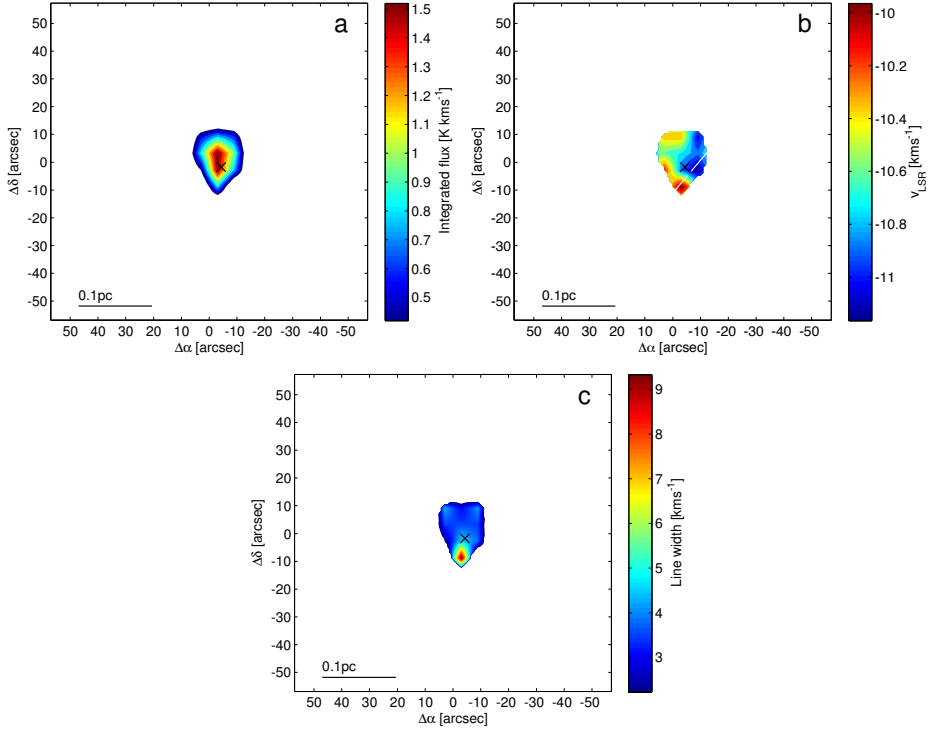


Figure 4.31: As Fig. 4.2 for the source L1206. The white line indicated the PA of the CO outflow.

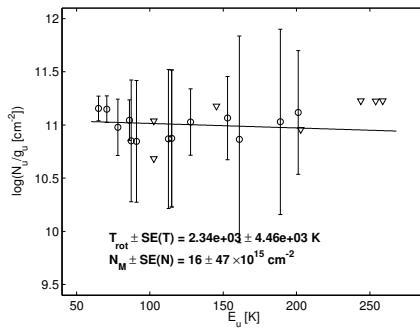


Figure 4.32: *L1206*: Rotation diagrams for the position of the maser.

4 Thermal methanol toward 6.7 GHz methanol maser sources

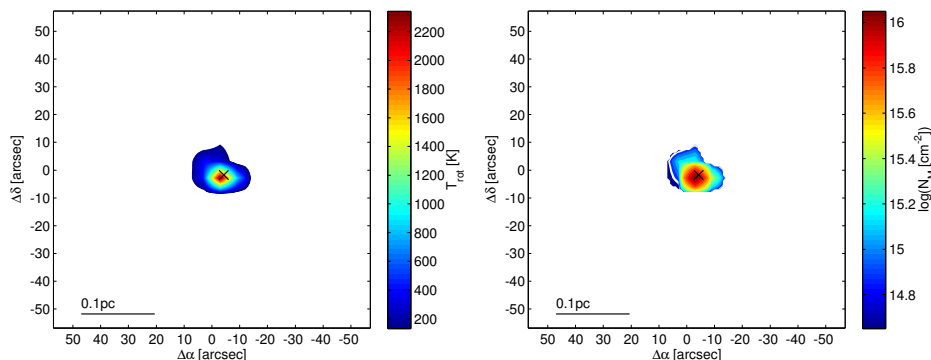


Figure 4.33: *L1206*: Maps of rotation temperature and column density.

velocity if the cut was made just to the South of the maser position at the same PA as the CO outflow (indicated in Fig. 4.31b).

During the data reduction process we discovered two issues with the data for L1206. First, the data acquired on the date 20070602 show large ripples in baselines of receptor R06. Second, the data taken on 20070616 show a pronounced broad “absorption” feature in some areas sampled by receptor R06. Consequently the data from receptor R06 in all twelve scans from these dates were flagged.

The $\text{CH}_3\text{OH} -1\text{E}$ line emission (Figs. 4.31) is compact and constrained to the centre of the map with a maximum close to the position of the methanol maser ($\Delta\alpha=-4.3''$, $\Delta\delta=-1.7''$). The line velocity map shows the blueshifted emission to the W and the more redshifted emission to the S and SE. There is a maximum in the line width map to the S associated with the redshifted emission.

The spectrum from the centre region (Fig. 4.30) is noisy and suffers from line blending. The $v_t = 1$ line is detected but right at the band edge. We exclude high optical depth effects as being important because of the lack of $^{13}\text{CH}_3\text{OH}$ emission. The contribution of SO_2 looks to be small and we have therefore included the +1E line in the rotation diagram analysis. The data do not allow us to map the excitation and the rotation diagram analysis is restricted to the centre pixel (Fig. 4.32). Lines up to $K=4$ are detected with our detection criteria. However, as can be seen in the rotation diagram the low signal to noise and line blending leads to an unrealistically high (2300 K) rotation temperature, also the population diagram analysis (Sec. 4.4.3) is affected by this. Nevertheless, the conclusion that the rotation temperature is high (> 100 K) is secure.

4.3.11 S255

With a parallax distance estimate of 1.59 kpc (Rygl et al. 2010), S255IR is a high mass star forming complex situated between the HII regions S255 to the East and S257 to the West. S255IR consists of three UCHII regions, S255N, S255S, and S255IR. The central

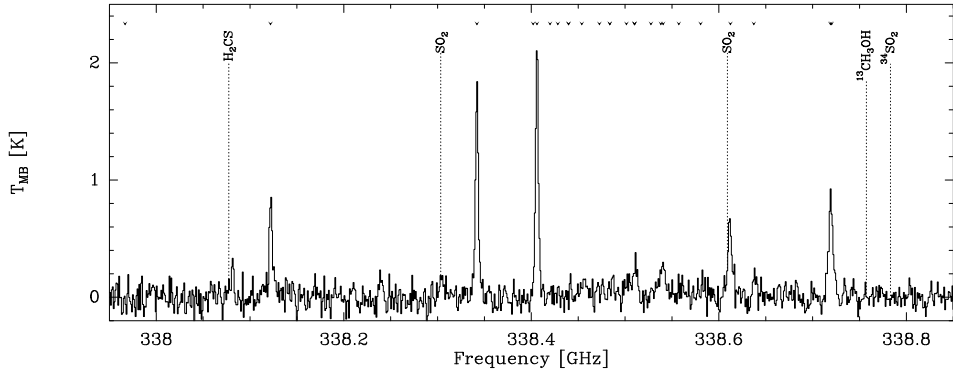


Figure 4.34: S255: Spectrum of the maser position. The tick marks at the top indicate the frequencies of the methanol lines.

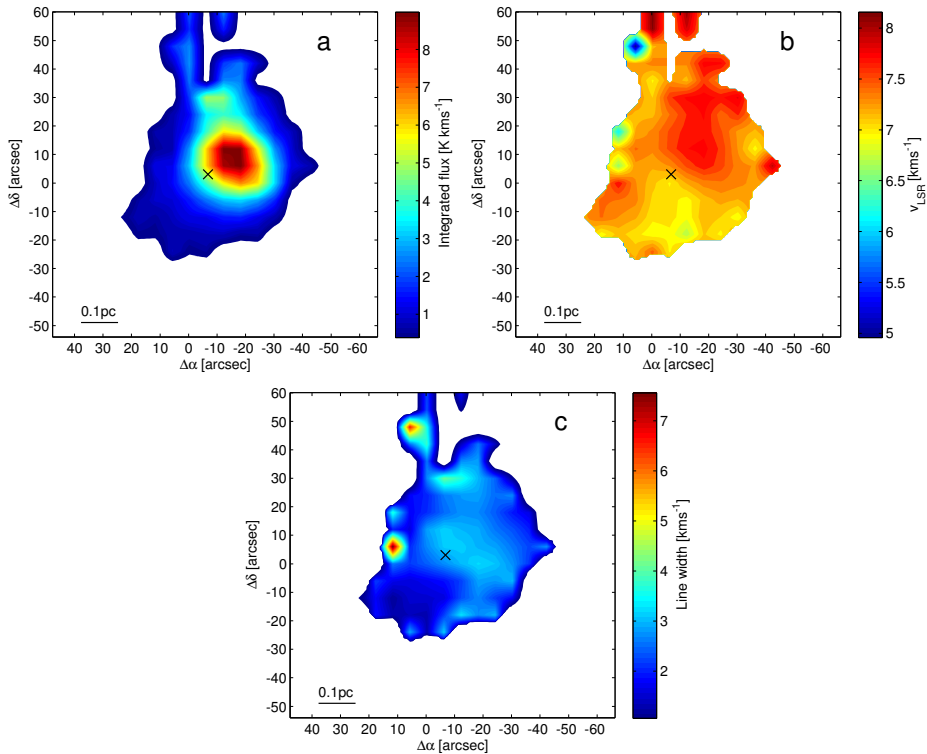


Figure 4.35: As Fig. 4.2 for the source S255.

4 Thermal methanol toward 6.7 GHz methanol maser sources

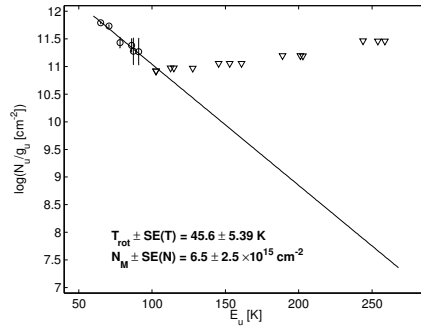


Figure 4.36: S255: Rotation diagrams for the positions of the maser.

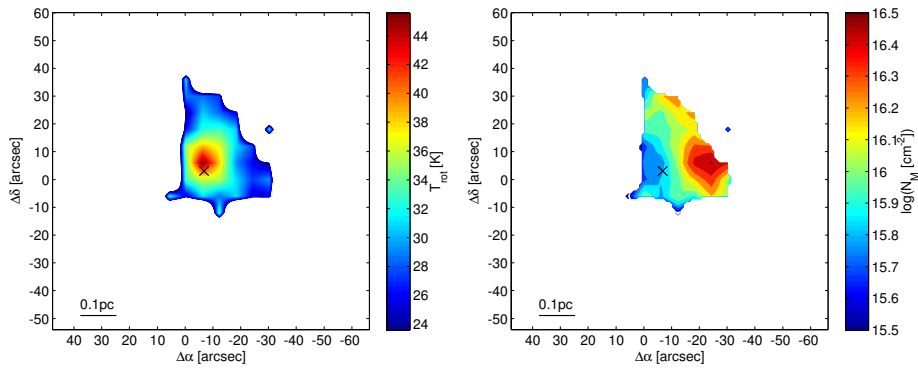


Figure 4.37: S255: Maps of CH_3OH rotation temperature and column density.

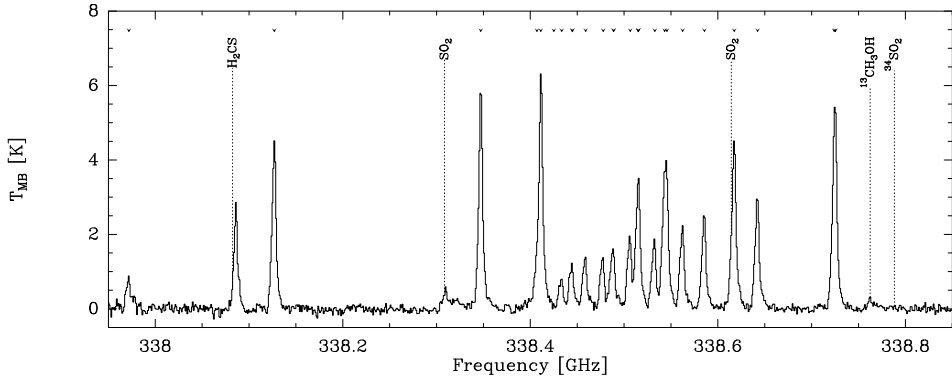


Figure 4.38: *W3(OH)*: Spectrum at the maser positions. The tick marks at the top indicate the frequencies of the methanol lines.

source S255IR has a luminosity of $2.4 \times 10^4 L_{\odot}$, and higher-resolution mm continuum observations have revealed that it breaks up into three separate mm cores: SMA1, SMA2, SMA3. There are several outflows that interact in the region, but the outflow originating from S255IR-SMA1 (associated with the methanol masers) is oriented roughly NE (red) - SW (blue) (Wang et al. 2011).

The $-1E$ line maps of S255 (Figs. 4.35) show that emission is roughly circular and shows a maximum in the central region of the map, to the NW of the position of the methanol maser ($\Delta\alpha = -6.8''$, $\Delta\delta = +3.0''$). The velocity map is complex, but there seems to be a velocity gradient across the maser position with redshifted emission associated with the line flux peak to the NW and more blueshifted emission to the S. The line width map is also complex but it appears that the line width is larger to the NW of the maser than to the S of the maser. Some interference in receptor R15 was seen in the data reduction process and consequently it was masked out.

The spectrum of the maser region (Fig. 4.34) shows that lines up to $K=2$ are detected. The $\nu_l = 1$ line is not detected and the SO_2 emission does not contribute significantly to the $+1E$ line which is included in the rotation diagram analysis (Fig. 4.36). The rotation temperature has a maximum close to the position of the maser, to the E of the $\text{CH}_3\text{OH} -1E$ line flux maximum (Fig. 4.37). The column density map indicates that the higher column densities are associated with the redshifted emission to the NW of the maser position and lower column densities with the blueshifted emission to the S.

4.3.12 W3(OH)

The well known UCHII region W3(OH) with a parallax distance estimate of 1.95 kpc (Xu et al. 2006) is part of the extensively studied W3 complex that houses many different stages of star formation (Helmich & van Dishoeck 1997). The 6.7 GHz CH_3OH maser emission is associated with the UCHII region (Harvey-Smith & Cohen 2006). Six

4 Thermal methanol toward 6.7 GHz methanol maser sources

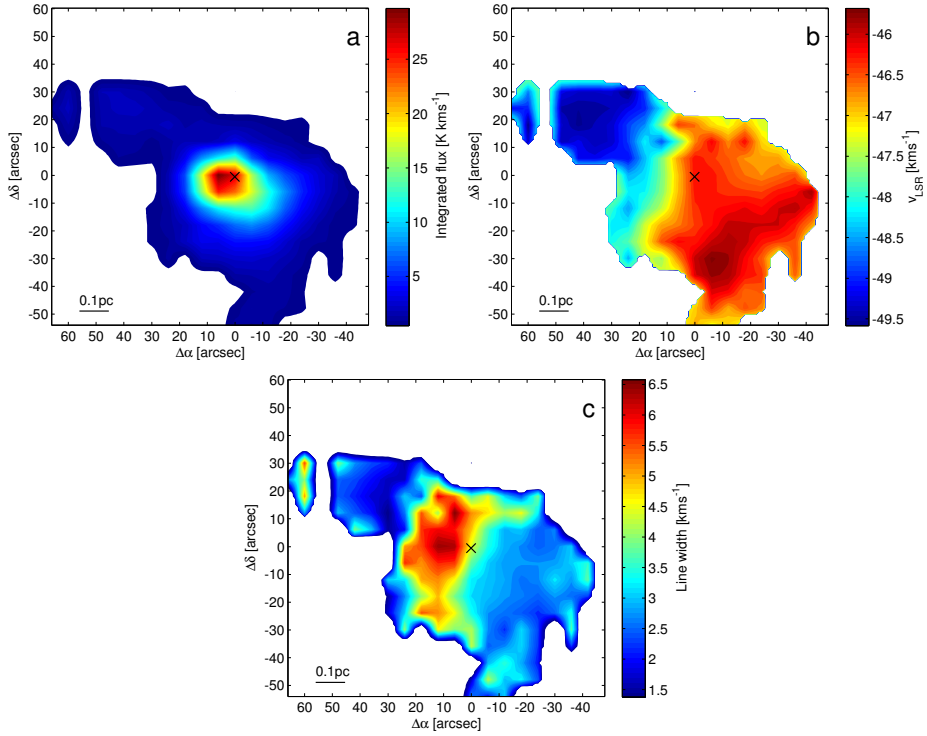


Figure 4.39: As Fig. 4.2 for the source W3(OH).

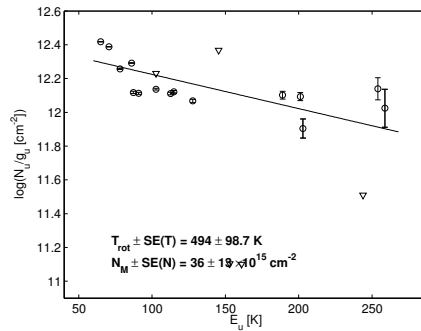


Figure 4.40: W3(OH): Rotation diagram of CH₃OH for the position of the maser.

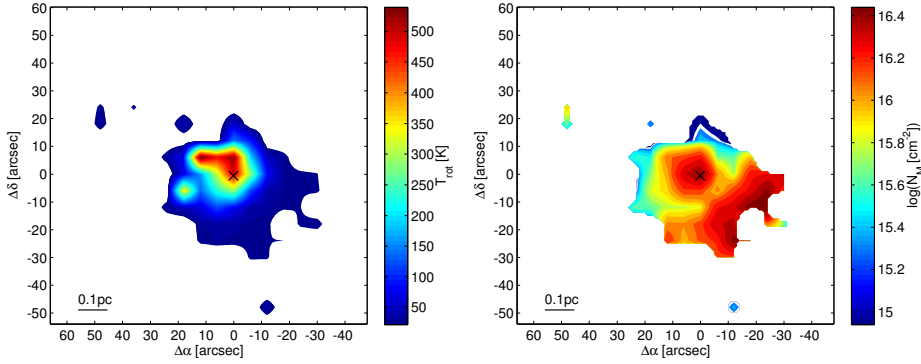


Figure 4.41: *W3(OH)*: Maps of CH_3OH rotation temperature and column density.

arc seconds to the East of *W3(OH)* is the hot core *W3(H₂O)* (van der Tak et al. 2000b, Bisschop et al. 2007). *W3(OH)* has a luminosity of $8 \times 10^4 L_{\odot}$ and *W3(H₂O)* has a luminosity of $2.4 \times 10^4 L_{\odot}$. In *W3(OH)* the mm-continuum emission is dominated by free-free emission, whereas in *W3(H₂O)* it is dominated by dust emission (Stecklum et al. 2002). High-resolution interferometric observations have confirmed the chemical differentiation of the two sources where O-bearing species such as CH_3OH are present in both sources whereas N-bearing species only are present in *W3(H₂O)* (Wyrowski et al. 1999).

The -1E line maps of *W3(OH)* (Fig. 4.39) show that the CH_3OH emission has higher line fluxes towards the centre of the map close to the position of the methanol maser ($\Delta\alpha=+0.1''$, $\Delta\delta=-0.5''$). The velocity map shows a large scale velocity gradient with redshifted velocities in the SW and blueshifted velocities towards the NE. The line width map shows that the large line widths are associated with the blueshifted emission to the NE of the maser and that the redshifted emission to the SW is associated with smaller line widths.

The spectrum of the maser region shows that lines up to $K=5$ are detected and line wings are seen in the lines. Notably the $\nu_1 = 1$ at 337.97 GHz is clearly detected and shows a complex line structure. There is a small amount of SO_2 but we have deemed its contribution small enough that we include the $+1\text{E}$ line in the rotation diagram analysis. There may be a second gas component (offset in velocity) seen in the CH_3OH emission but the complexity of the spectrum and line blending prohibits us from separating the two components. Furthermore, because of the $^{13}\text{CH}_3\text{OH}$ detection, optical depth effects cannot be neglected (Fig. 4.40) and it is clear that the rotation diagram analysis breaks down in the centre region.

The rotation temperature map of *W3(OH)* (Fig. 4.41) shows a maximum at the position of the maser and extending to the NE, towards the more blueshifted emission. The column density map shows a maximum at the position of the maser and also an enhancement to the SW associated with the redshifted emission.

4 Thermal methanol toward 6.7 GHz methanol maser sources

Table 4.3: Derived rotation temperatures and methanol column densities at the position of the maser.

Source	$\Delta\alpha$ ($''$)	$\Delta\delta$ ($''$)	T_{rot} (K)	N_{M} (cm^{-2})
AFGL5142	+30.1	+2.6	65.2 ± 12.0	$1.1 \pm 0.7 \times 10^{16}$
DR21 FIR1	-0.3	+0.1	24.1 ± 4.3	$1.5 \pm 1.2 \times 10^{16}$
DR21 FIR2	+17.6	+22.3	39.5 ± 6.0	$4.3 \pm 2.3 \times 10^{15}$
G23.207-00.377	+0.2	-3.9	51.1 ± 4.2	$2.0 \pm 0.5 \times 10^{16}$
G23.389+00.185	-0.1	-0.1	67.0 ± 18.3	$6.6 \pm 5.1 \times 10^{14}$
G23.657-00.127	-	-	158.6 ± 78.1	$8.3 \pm 8.4 \times 10^{14}$
G24.541+00.312	-	-	-	-
G40.62-0.14	+0.1	+0.1	92.5 ± 26.3	$9.7 \pm 6.9 \times 10^{14}$
G73.06+1.80	+0.6	+0.7	50.5 ± 10.0	$1.3 \pm 0.8 \times 10^{15}$
G78.12+3.63	-0.6	+1.7	222.3 ± 89.6	$4.4 \pm 3.6 \times 10^{15}$
L1206	-4.3	-1.7	2342.6 ± 4456.0	$1.6 \pm 4.7 \times 10^{16}$
S255	-6.8	+3.0	45.6 ± 5.4	$6.5 \pm 2.5 \times 10^{15}$
W3(OH)	+0.1	-0.5	493.6 ± 98.7	$3.6 \pm 1.3 \times 10^{16}$

Notes: The maser position is given in $\Delta\alpha$ and $\Delta\delta$ relative to the map centre. The two sources G23.657-00.127 and G24.541+00.312 were observed in single pointing mode and therefore do not have any offsets. Too few lines were detected in G24.541+00.312 to perform a rotation diagram analysis.

4.4 Analysis

4.4.1 Rotation diagram analysis

The results of our rotation diagram analysis are summarised in Table 4.3 which lists the derived rotation temperatures and column densities for the positions of the methanol masers. We find typical rotation temperatures between 25 and 100 K and column densities between 6×10^{14} and $2 \times 10^{16} \text{ cm}^{-2}$. For sources which have a simple structure both the rotation temperature peak and column density peak is closely associated with the maser position ($< 0.1 \text{ pc}$). This result is similar to what we found in Chapter 3. However, in Cep A HW2 we were able to identify two different velocity components at the maser position with the second component presumably associated with the maser emission. A more detailed analysis of the second gas component, using population diagram and non-LTE modelling, revealed that in fact the column density was significantly higher for this gas component but that beam dilution and optical depth effects made the rotation diagram analysis break down (Chapter 3).

4.4.2 CH₃OH gas distribution

To compare the CH₃OH gas distribution of the sources in our sample we have fitted a two dimensional Gaussian to the integrated flux of the $-1E$ line. The emission is represented by an ellipse with corresponding offset from the map centre, major/minor axis, and position angle. To determine the linear scales the distances in Table 4.1 were used. The results of the fits are presented in Table 4.4. For sources that we mapped we have determined the distance r between the methanol maser position and the centre of the ellipse. It should be noted that although the beam size of the JCMT at 338 GHz is $14''$, the signal-to-noise ratio of our data allows us to determine the positions and source sizes to a fraction of the beam width. Moreover, the velocity field in the $-1E$ maps indicates that the sources are resolved.

Based on the morphology of the $-1E$ line maps we have divided the sources into three separate classes: weak (*W*), compact (*C*), and extended (*E*). The two weak sources G23.657–00.127 and G24.541+00.312, for which the distance estimate of G23.657–00.127 is based on parallax measurements, are amongst the more distant sources in our sample. Because the sources were observed in a single deep pointing we cannot map these sources and therefore we have no reliable size estimates.

In the seven compact sources of our sample, the CH₃OH $-1E$ line emission is isolated and confined to a well defined region of the maps with the peak of the $-1E$ line flux close to the maser position ($r < 0.05$ pc). Furthermore, the velocity maps indicate a relatively simple velocity field. The distances to the seven sources span from 0.78 kpc to 4.6 kpc, though only for L1206 and G78.12 are the distance estimates based on parallax measurements. Nevertheless, the compact sources have major axes between $10''$ and $20''$ which correspond to physical sizes between ~ 0.04 pc and ~ 0.4 pc. As discussed in Sec. 4.3 most of these sources have been observed in other molecules. With the exception of G23.207–00.377 all compact sources can be fitted with a simple linear velocity gradient along the major axes. The fitted linear velocities v_{lin} are between -1.4 and 12.4 km s⁻¹ pc⁻¹ (Table 4.4, column 10). A similar physical extent and velocity gradient is seen in Cep A, where the gas is part of the HW2 wide-angle outflow. So including Cep A, we have a sample of 14 sources, of which eight sources are C-type.

The three extended sources in our sample DR21, S255, and W3(OH) all have measured parallaxes with corresponding distances between 1.45 and 2.0 kpc. In these three sources, the CH₃OH $-1E$ line emission is extended over 0.3 – 0.5 pc and shows a complex velocity field in the central velocity maps. Fitting 2D Gaussians is not appropriate for these sources, which are part of larger-scale molecular cloud complexes, and have already been extensively discussed in the literature.

Table 4.4: Results of the 2D Gaussian fit of the integrated $-1E$ line emission.

Source	Class	$\Delta\alpha$ (")	$\Delta\delta$ (")	a (")	b (")	PA ($^\circ$)	a (pc)	b (pc)	v_{lin} (km s^{-1} pc^{-1})	r (pc)	σ_r (pc)
AFGL5142	C	+33.00	+3.48	20.0	15.8	5.7	0.17	0.14	6.78	0.027	0.009
DR21 FIR1	E	+19.53	+40.48	67.0	19.1	26.8	0.47	0.13	—	0.316	0.007
DR21 FIR2	E	+19.53	+40.48	67.0	19.1	26.8	0.47	0.13	—	0.129	0.007
G23.207-00.377	C	-1.62	-3.00	15.8	12.2	72.7	0.355	0.273	—	0.045	0.022
G23.389+00.185	C	+0.54	+1.08	10.3	9.6	-74.0	0.223	0.208	-1.37	0.028	0.022
G23.657-00.127	W	—	—	—	—	—	—	—	—	—	0.016
G24.541+00.312	W	—	—	—	—	—	—	—	—	—	0.028
G40.62-0.14	C	-1.06	-1.55	11.1	10.1	-58.4	0.12	0.11	6.03	0.021	0.011
G73.06+1.80	C	+0.13	-0.15	11.6	9.7	79.5	0.28	0.23	1.7	0.021	0.024
G78.12+3.63	C	-2.42	+3.70	14.3	9.6	-51.2	0.12	0.08	12.4	0.023	0.008
L1206	C	-3.30	+1.56	10.9	8.2	2.5	0.041	0.031	7.44	0.013	0.004
S255	E	-12.30	+12.72	34.5	22.2	4.4	0.27	0.17	—	0.086	0.008
W3(OH)	E	+1.08	-5.09	38.5	22.9	56.0	0.36	0.22	—	0.044	0.010

Notes: The in offsets in RA ($\Delta\alpha$) and DEC ($\Delta\delta$) are measured from the map centre, also reported are the major axes (a), minor axes (b), and position angles (PA). The linear scales are based on the distances in Table 4.1. v_{LIN} is the linear velocity gradient measured along the major axis and r is the maser offset from the centre of the fitted 2D Gaussian. The two sources G23.657-00.127 and G24.541+00.312 were observed in single pointing mode and are only included in the table for completeness.

4.4.3 Population diagram analysis

The environment close to the protostar is expected to be quite different from the more extended emission region. In particular, the excitation of the methanol maser requires specific conditions and the maser extent is typically only a few hundred to a couple of thousand AU, see Chapter 5 (e.g. Bartkiewicz et al. 2009). Therefore, to investigate the influence of source size/clumpiness and optical depth effects on our data we have performed a population diagram (PD) analysis of the spectra at the maser position. The analysis is performed as a χ^2 test in which the methanol column density, excitation temperature, source size, are varied to minimise the χ^2 difference between the synthetic and observed spectra. In the process the optical depths of the transitions are also calculated. The beam filling factor $f = \Omega_s/\Omega_a$ is assumed to be the same for all lines, although in reality the highly excited lines could have a smaller extent than the lines with lower excitation temperatures. In the two extreme cases that all lines are optically thick and all lines are optically thin the method is degenerate in $f \times T_{\text{ex}} = \text{Constant}$ and $f \times N_M = \text{Constant}$, respectively. However, this degeneracy is broken if both optically thin and optically thick lines are observed. For a detailed discussion on the PD analysis see Goldsmith & Langer (1999) and Wang et al. (2010). In order for the method to work a minimum of three lines need to be observed, therefore we have only performed this analysis in the centre region where more lines are detected. For each best fit we can check the optical depth of all lines.

We have used column densities from 10^{14} to 10^{18} cm^{-2} , excitation temperatures from 10 to 500 K and beam filling factors between 0.01 and 1 (corresponding to source sizes between $1.5''$ and $> 14''$). The results of the analysis for the individual sources are summarised in Table 4.5. We do not find any large beam dilution effects in our analysis, nor very high optical depths. Compared to Cep A the apparent lack of small source sizes may be because for most sources only the low- K lines have integrated fluxes larger than our signal-to-noise cut-off ratio of six. The main contribution to the low- K line emission likely comes from the more extended gas rather than the gas directly associated with the maser region, as in Cep A (Chapter 3). In fact, for several sources we find lower excitation temperatures than what was found in the rotation diagram analysis. This results from the fact that we infer moderate optical depths ($\tau \approx 1$) for the lower K lines. The optical depth correction raises the population estimates of those levels, thus lowering the derived excitation temperature. We find beam-averaged column densities between 3×10^{14} and 10^{16} cm^{-2} . Taking the beam filling factor into account the corrected total column densities are a few times higher (4×10^{14} to $4 \times 10^{16} \text{ cm}^{-2}$). These column densities are similar to what we found for the methanol gas associated with the larger scale outflow at the maser position in Cep A. For the second gas component in Cep A, presumed to be associated with the maser emission, we found a column density of a few times 10^{17} cm^{-2} , at least an order of magnitude higher than found here. Furthermore, in the sources where the $v_t = 1$ line is detected, it seems to have a small offset in velocity compared to the low- K lines of the $v_t = 0$ band. All these reasons suggest that we are primarily probing the more extended CH_3OH gas, and to a much lesser extent the highly excited masing gas.

4 Thermal methanol toward 6.7 GHz methanol maser sources

Table 4.5: Results of the population diagram analysis.

Source	$\Delta\alpha$ (")	$\Delta\delta$ (")	T_{ex} (K)	N_{M} (cm^{-2})	Ω_s/Ω_a	τ_{min}	τ_{max}
AFGL 5142	30.1	0.0	20.8	7.4×10^{15}	1	0.002	1.16
DR21 FIR1	-3.2	-0.08	12.9	1.9×10^{15}	1	0.036	0.19
DR21 FIR2	14.7	23.3	12.9	4.0×10^{15}	0.91	0.02	0.40
G23.207-00.377	3.0	-2.6	20.8	1.0×10^{16}	1	0.13	1.57
G23.389+00.185	0.0	0.0	20.8	4.0×10^{14}	0.81	0.0052	0.063
G23.657-00.127	0.0	0.0	48.5	2.9×10^{14}	0.76	0.0079	0.026
G24.541+00.312							
G40.62-0.14	0.3	2.9	24.8	5.4×10^{14}	0.81	0.0055	0.085
G73.06+1.80	0.1	0.3	16.8	6.3×10^{15}	0.16	0.18	0.90
G78.12+3.63	-3.2	3.0	28.7	1.6×10^{15}	0.91	0.0010	0.23
L1206	-3.0	-2.8	340	1.4×10^{15}	0.76	0.0008	0.0025
S255	-6.3	6.0	16.8	3.4×10^{15}	0.95	0.096	0.48
W3	-2.6	0.1	99.2	5.8×10^{15}	0.95	0.0059	0.16

4.5 Discussion

We have mapped the large scale ($10'' - 50''$) distribution of the $\text{CH}_3\text{OH } J = 7_K \rightarrow 6_K, v_t=0$, band towards 14 regions (including Cep A) of high-mass star formation associated with 6.7 GHz methanol masers. Two sources are too weak (W) to map and will be partly excluded from this discussion. The eight compact (C) sources are characterised by the CH_3OH emission being confined to a < 0.4 pc region and with a single peak close to the maser position in the integrated flux maps. In the remaining three sources, the emission is extended (E) over $0.3 - 0.5$ pc without a clear peak in the maps of the line flux, velocity, and line width.

The largest uncertainty in our analysis stems from the poor distance estimate of half of our sample. Only for seven sources are the distance estimates based on parallax measurements (Cep A and L1206 are the only compact sources with measured parallax), typically accurate to within $\sim 10\%$. For the remaining sources in the sample the distance estimate is found in the literature and based on the kinematic distance, accurate to a factor of ~ 2 .

4.5.1 Excitation of CH_3OH gas

To characterise the large scale physical conditions of the gas we have performed a pixel-based rotation diagram analysis for the sources for which we have a sufficiently high signal to noise ratio. We typically find the highest rotation temperatures close to the maser position. The column density peak seems to be less closely associated with the maser position. Note that this is similar to what we found in Cep A initially, where closer inspection of the excitation on smaller scales proved that the highest column densities

occur at the maser position. Typical rotation temperatures for the large scale distribution are 30 to 50 K and column densities between 10^{15} and 10^{17} cm^{-2} , similar to what we found in Cep A (Chapter 3).

Because the 6.7 GHz CH_3OH maser is typically located within ~ 1000 AU of the protostar(s) responsible for the excitation of the masing gas (Bartkiewicz et al. 2009), we therefore expect the highly excited gas to have a similar small extent. To investigate optical depth and beam dilution effects a population diagram analysis was performed on the gas at the maser positions. However, we do not see the need for large beam dilution effects in our analysis. One possible explanation for this is that we mainly detect the lower K lines and that the main contribution to the emission of these lines comes from the more extended gas. In Cep A we were able to distinguish two different gas components, one component with strong low- K lines associated with the large scale structure, and a second component associated with the masing gas and much more readily detected in the high- K lines. In the thermal CH_3OH spectra of the sources in our sample we are not able to identify more than one single gas component and at most positions the line shape appears Gaussian. A possible explanation may be the relatively large distances of the sources in our sample (with the exception of L1206) compared to that of Cep A (700 pc, see below).

In fact, in the population diagram analysis we find for several sources a lower excitation temperature than we find in the rotation diagram analysis. For these sources we also find that the optical depth of the lowest K lines is not negligible ($\tau \approx 1$). The optical depth correction and consequently lower excitation temperature in the population diagram analysis also leads to somewhat lower estimates of the column density. The general lack of detection of the $^{13}\text{CH}_3\text{OH}$ ($13_{0,13} \rightarrow 12_{1,12}$) A^+ $\nu_t = 0$ line with an upper energy level of 206 K and high transition probability ($S\mu^2 = 1.11$), indicates that the optical depth is at most moderate.

An independent indication of highly excited CH_3OH gas is the detection of the -1A $\nu_t = 1$ line at 337.97 GHz in approximately half of the sources in our sample. Because collisional pumping alone is very inefficient at populating the torsionally excited state, the $\nu_t = 1$ line is an indicator of infrared pumping at work (Leurini et al. 2007). The sources for which the $\nu_t = 1$ line is detected also show signs of the high- K lines, supporting the argument of highly excited gas. Although high- K lines are weak, we have a considerable detection rate of the $\nu_t = 1$ line. The high detection rate of the $\nu_t = 1$ line could be an effect of our sample selection, because we have intentionally targeted bright 6.7 GHz methanol maser sites, which are thought to be pumped by infrared radiation. For both the $\nu_t = 1$ line and the high- K lines beam dilution effects are likely important. There does however not seem to be any correlation between the distance of the source or the luminosity and the occurrence of the $\nu_t = 1$ line which one might expect. Neither are the sources with the $\nu_t = 1$ line detection those with the largest integrated flux of the -1E line. Instead, the $\nu_t = 1$ line seems to be correlated with the sources for which we find a non-negligible optical depth in the low- K lines in the population diagram analysis. Higher resolution interferometric observations with beam sizes similar to the extent of the maser regions (and more accurate distance estimates) would greatly help to constrain the excitation of the highly excited gas (Beuther et al. 2007c).

4.5.2 Morphology

The three extended sources all have accurate distance estimates and are excellent candidates for detailed studies, however the complexity of the sources makes them less suitable for the analysis method applied here. Therefore, the remainder of the discussion will focus on the eight sources classified as compact.

The $\text{CH}_3\text{OH} -1\text{E}$ emission of the compact sources is confined to a central peak in the integrated -1E flux maps. The confined emission and central peak indicates that, as in Cep A, there is a single source of CH_3OH production in these sources. We have characterised the -1E line emission by a 2D Gaussian and find it centred close to the maser positions ($r < 3.4''$). The absolute pointing accuracy of the observations is $\sim 1''$ which means that the maser may be somewhat offset from the peak of the -1E line flux, similar to what has been seen in Cep A. All but one of the compact sources (G23.207–00.377) show a simple linear velocity gradient along the major axis, further strengthening the argument for a central origin of the CH_3OH gas. We suggest that the velocity field indicates a young, large opening angle outflow, similar to what is found in Cep A (Chapter 3).

Although the source sizes that we find are similar to the beam of the JCMT telescope in several cases, the signal-to-noise ratio of the data allows us to measure the position and size of the sources to a few arc seconds accuracy, and we therefore argue that the sources are resolved. This argument is further supported by the velocity gradients seen in the central velocity maps (and along the major axes). Using the adopted distances in Table 4.1 we find major axes between 0.04 and 0.4 pc. The chemical life-time of CH_3OH is expected to be a few 10^4 years (van der Tak et al. 2000a). Assuming a common age of 2.4×10^4 (as found in Cep A) we find expansion velocities of 0.8 to 8 km s^{-1} (similar to the 5.8 km s^{-1} we find in Cep A). The spread in expansion velocities could have at least three origins. First of all, the sources may not have the same age. Secondly, it could be an orientation effect. Outflows in the plane of the sky have larger apparent extent than outflows oriented towards/away from us. The fitted linear velocity gradient along the major axes tends to be higher for the sources with smaller extents, supporting the argument of orientation effects playing a role. Thirdly, the linear velocity gradient depends directly on the distance, and the uncertainties of the distance estimates are substantial for all the compact sources but Cep A and L1206.

Finally, we also note that the H_2CS feature at $\sim 338.08 \text{ GHz}$ appears to be common towards regions of star formation (e.g. van der Tak et al. 2003). In most sources in our sample the H_2CS seem to be offset by a few km s^{-1} from the CH_3OH , implying that it may trace another gas component.

4.6 Conclusions

We have performed JCMT observations of the thermal CH_3OH gas in a sample of 12 high-mass star forming regions. Thermal CH_3OH ($J = 7_K \rightarrow 6_K$) emission was detected towards all sources although for two of the sources the emission was not bright enough to be mapped. The rotation diagram analysis method was used to analyse the large scale

excitation of the gas and towards the maser positions where more lines were detected we have performed a population diagram analysis. The main conclusions of this work are:

- In most sources the thermal CH₃OH emission is confined and shows a single peak close to the maser position in the integrated flux maps, consistent with a single source of origin of the CH₃OH gas.
- A large fraction of sources show a linear velocity gradient along the major axis of the integrated flux of the $-1E$ line, indicating an outflow, probably young and with a large opening angle.
- In the population diagram analysis we find no evidence of a small highly excited gas component as characteristic of hot cores. However this may be because we are not able to separate the highly excited gas in the core from the more extended thermal CH₃OH emission.
- The population diagram analysis indicates that in half of the sources the optical depth of the low- K lines is not negligible which results in somewhat lower estimates of the excitation temperature and column density than what we find in the rotation diagram analysis.
- There is evidence of the CH₃OH $J = 7 \rightarrow 6 A^+ \nu_t = 1$ line in half of the sources. The detection of this line may indicate radiative pumping and the high detection rate is probably due to the source selection. The $\nu_t = 1$ line and the high- K lines could come from a region of ~ 1000 AU, seriously affected by beam dilution at the current resolution.
- Half of the sources in our sample have measured parallaxes. For the remaining sources, with kinematic distance estimates, the major uncertainty in our analysis is the accuracy of the distance estimate.
- Assuming radiative excitation is important on 1000 AU scales, with the onset of ALMA, high-resolution imaging of thermal CH₃OH emission is possible for large source samples. This will shed light on the origin of the CH₃OH masers.

Acknowledgements

This research was supported by the EU Framework 6 Marie Curie Early Stage Training programme under contract number MEST-CT-2005-19669 “ESTRELA”.

Dynamics of 6.7 GHz methanol masers in high-mass star-forming regions

II. Sources with confined thermal CH₃OH emission

Abstract

The 6.7 GHz CH₃OH maser serves as a signpost of high-mass star formation. Moreover, a recent VLBI study has shown that in 30% of the sources the CH₃OH masers occur in ring-like structures on scales of a few hundreds of AU and with velocity fields indicative of infall or outflow. On larger physical scales, in a sample of twelve high-mass star-forming regions, seven have been found to have confined (<0.4 pc) thermal CH₃OH emission thus making them suitable for a study of the relation of the thermal CH₃OH emission and the CH₃OH maser emission. To test the hypothesis that there is a common origin of the 6.7 GHz CH₃OH maser emission and the thermal CH₃OH emission, we have compared the maser emission in seven sources with the position and orientation of that of the thermal emission. The European VLBI Network has been used to map at high resolution the 6.7 GHz methanol maser emission in a sample of five sources that all have compact thermal CH₃OH emission. Phase referencing allows for determining the position to milli-arcsec accuracy. A further two sources with compact thermal CH₃OH emission that recently have been mapped with the EVN have been included. Three (AFGL5142, G73.06, and G78.12) of the five sources observed by us with the EVN were successfully mapped and the 6.7 GHz CH₃OH maser emission has a physical extent between 330 and 1700 AU. For the two sources (L1206 and G40.62) that we were unable to map CH₃OH maser data from the literature have been used, this is also the case for the last two sources (G23.207 and G23.389) that were recently observed with the EVN. In all seven sources in this study the CH₃OH maser emission arises close (<0.05 pc) to the centre of the thermal CH₃OH emission. Further, in at least three of the seven sources the major axis of the CH₃OH maser emission is roughly perpendicular to the velocity gradient seen in the thermal CH₃OH emission. The position of the CH₃OH maser emission close to the centre of

5 Dynamics of 6.7 GHz methanol masers in high-mass star-forming regions

the thermal CH_3OH distribution is in accordance with a common origin of the gas phase CH_3OH in these sources. Further, in several sources the CH_3OH masers seem to delineate or be part of a disk or torus in the equatorial region of the YSO with major axes orthogonal to that of the thermal CH_3OH velocity field and we suggest that the thermal CH_3OH is entrained in a bipolar outflow. The high sensitivity and high resolution capabilities of new instruments such as ALMA will allow us to probe these regions in an unprecedented manner.

5.1 Introduction

Since their discovery twenty years ago (Menten 1991a) the 6.7 GHz CH₃OH masers have been shown to be associated with the earliest stages of high-mass star formation. To date, there are >800 known CH₃OH maser sites (Green et al. 2009). A study of the radio continuum emission towards 233 CH₃OH maser sites shows that only ~25% of the CH₃OH masers are associated with HII regions (Walsh et al. 1998). In contrast, sub-millimetre continuum from warm dust has been detected towards more than 95% of the 6.7 GHz CH₃OH masers (Hill et al. 2005). Recent studies suggest that the CH₃OH maser turns on before the H₂O and OH masers that are sometimes associated with the same sources (Breen et al. 2010). The water masers typically span a larger velocity range than the methanol masers and it is therefore likely that they occur in different physical structures (Bartkiewicz et al. 2011). The sources studied with high resolution VLBI techniques show that the CH₃OH maser distributions typically have extents between 100 and 2000 AU with different morphologies and have been classified as: simple, linear, complex, and disks (Norris et al. 1998, Phillips et al. 1998, Minier et al. 2002, Pestalozzi et al. 2004, Bartkiewicz et al. 2009). However, some sources have been found to be embedded in larger structures seen at shorter baselines (Pandian et al. 2011).

A recent VLBI study showed that 30% (9 of 31) of the sources selected from a blind survey of 6.7 GHz CH₃OH masers had an elliptical morphology (Bartkiewicz et al. 2009). The morphology suggests that the masers occur in a ring-like structure and that the exciting source(s) are in the centre of the ring as in the spectacular Ring source (G23.657–00.127) (Bartkiewicz et al. 2005a) and Cepheus A (Cep A) HW2 (Chapter 2). Moreover, the lack of cm continuum emission in the elliptical sources compared to the rest of the sample suggests an earlier evolutionary stage prior to any detectable free-free emission. The velocity field of the maser spots indicates that both radial and rotational velocities are important, which together with the ellipse location suggest that the maser emission occurs in a “torus” in the equatorial region of the protostar. However, with the maser observations alone it is not possible to determine the orientation of the ring and consequently not possible to distinguish outflow motions from those of infall.

Furthermore, the CH₃OH masers have recently been used to probe the magnetic field on similarly small scales (mas) and in at least two sources the magnetic field appears to be funnelling the infalling gas through a circumstellar torus around the protostellar object towards the accretion disk (Vlemmings et al. 2010, Surcis et al. 2011).

The H₂O masers and radio continuum seen on size scales similar to the CH₃OH maser emission appear to be associated with disk winds, thermal jets, and outflows (Torrelles et al. 2011). On parsec scales, molecular outflows are common signatures of these small scale processes. However, source multiplicity, with overlapping outflows and precession of the outflows, often complicates the picture and it can be difficult to trace the larger scale outflows back to a particular protostar and determine its orientation.

Recent studies have shown that in AFGL 5142 the velocity field of the CH₃OH masers can be described by a radial infall whereas the H₂O masers associated with the source seem to trace the disk wind (Goddi et al. 2007). In the case of G78.12 (IRAS 20126+4104) the CH₃OH maser emission seems to arise in two distinct regions, one

5 Dynamics of 6.7 GHz methanol masers in high-mass star-forming regions

Table 5.1: Coordinates of the science targets phase centres and calibrators observed with the EVN.

Source	Coordinates (J2000)		θ °	Cal.
	RA (h m s)	Dec (° ′ ″)		
AFGL 5142	05 30 48.0	+33 47 55		A
J0518+3306	05 18 05.1425	+33 06 13.365	2.7	
G73.06	20 08 09.8	+35 59 20		B,C
J2016+3600	20 16 45.6188	+36 00 33.374	1.7	
G78.12	20 14 26.1	+41 13 31		B,C
J2007+4029	20 07 44.9449	+40 29 48.604	1.5	
G40.62-0.14	19 06 00.0	+06:47:22		B,C
J1912+0518	19 12 54.2577	05 18 00.421	2.3	
L1206	22 28 51.5000	+64 13 42.000		A,B,C
J2232+6249	22 32 22.8655	+62 49 36.436	1.5	
J2208+6519	22 08 03.1103	+65 19 38.791	2.5	
DA193	05 55 30.8056	+39 48 49.165		A
3C345	16 42 58.8100	+39 48 36.994		B
3C454.3	22 53 57.7479	+16 08 53.561		C

Notes: θ is the angular separation between maser and phase calibrator. A, B & C designates the amplitude and bandpass calibrators used for each source respectively.

group of maser spots seems to trace the disk and a second group appears to be associated with the disk wind interface. Also in this source the H₂O masers are associated with outflow and appear to trace a conical jet (Moscadelli et al. 2005, 2011).

In Chapter 4 we mapped the distribution and kinematics of the thermal CH₃OH emission in a sample of high-mass star-forming regions. Based on those results we classified seven of the twelve observed sources as having confined (< 0.4 pc) thermal CH₃OH emission. The aim of this chapter is to compare how the CH₃OH maser emission in these seven sources is related to the thermal CH₃OH emission and other outflow tracers. We present EVN observations of the 6.7 GHz CH₃OH maser in three (AFGL 5142, G73.06, and G78.12) of these seven sources. Of the four remaining sources, two (G23.207 and G23.389) have been classified as having elliptical maser distributions (Bartkiewicz et al. 2009), and also for the remaining two sources (L1206 and G40.62) maser data from the literature have been used.

5.2 Observations and data reduction

The EVN observations were performed in Nov 2004 as part of a larger project EL032. The telescopes participating in the experiment were Effelsberg, Westerbork, Medicina, Onsala, Toruń, Cambridge, Noto, and Darnhall. All observations were performed in phase referenced mode and each source was observed for a total of ~2 h, split into two

Table 5.2: 2D distribution of the 6.7 GHz CH₃OH maser emission.

Source	$\Delta\alpha$ (mas)	$\Delta\delta$ (mas)	a (mas)	b (mas)	PA ($^\circ$)
AFGL 5142	+213.3	-440.1	184.2	124.3	-1
G73.06	+528.5	+657.2	342.6	47.2	-78
G78.12	-436.4	-296.6	306.0	43.9	81

Notes: The positional offsets $\Delta\alpha$ and $\Delta\delta$ refer to the positions of Table 5.1, also reported are the major axes (a), minor axes (b) and position angles (PA).

one hour blocks separated by a few hours to improve the uv-coverage. Each one hour block included observation of a strong calibrator at the beginning and end of the block, the remaining observing time was spent switching between the target source and a nearby calibrator (3 min + 2 min). Table 5.1 lists target coordinates and calibrator details. The receivers were set up with the rest frequency of 6668.5142 MHz and a bandwidth of 2 MHz with 1024 channels, corresponding to a velocity resolution of 0.088 km s⁻¹ and a total velocity coverage of 90 km s⁻¹. Both right and left circular polarisation were recorded.

The data were correlated on the EVN correlator at JIVE with a short integration time of 0.25 s to facilitate the possibility of performing a wide field search in a larger area surrounding the known maser position. All data reduction and analysis were performed in AIPS following the same recipe as described in Chapter 2. For some sources the phase calibrator was too weak to image directly and for these sources reverse phase referencing was performed. After initial calibration on the brightest maser channel the calibration was applied to the phase reference source and the offset in position measured and applied to the clean maser cube.

The final image cubes have an rms of 2 mJy beam⁻¹ in the case of G73.06 and G78.12, and 4 mJy beam⁻¹ in the case of AFGL 5142. These cubes were searched for maser spots with the AIPS task SAD. Stepping through the cube on a channel by channel basis all spots with a signal to noise larger than five were fitted by a Gaussian. The list of maser spots was then manually inspected and spurious spots that did not have any adjacent neighbour were removed.

5.3 Results

We have successfully mapped three (AFGL 5142, G73.06, and G78.12) of the five sources with the EVN that have compact thermal methanol emission. Due to the weak flux levels of both target and calibrator sources, we were unable to calibrate and image the two sources G40.62-0.14 and L1206 with these observations. The observations were performed in phase referenced mode and we estimate the absolute position to be accurate to ~ 1 mas (Chapter 2).

In Fig. 5.1 we present the spectra and maser spot distribution of the three sources,

5 Dynamics of 6.7 GHz methanol masers in high-mass star-forming regions

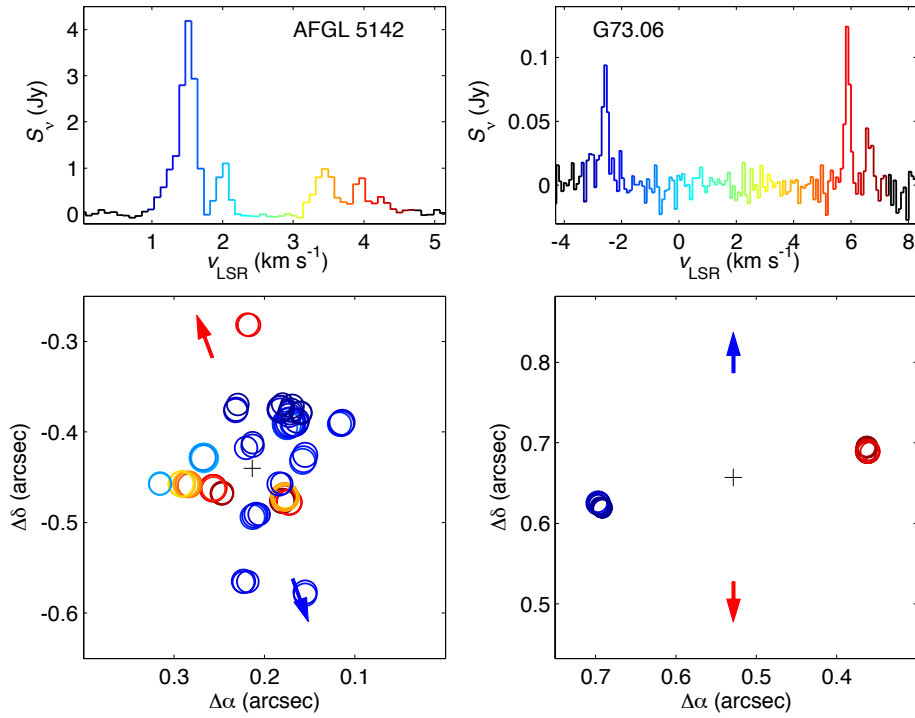


Figure 5.1: Spectrum of the maser emission and maps of the individual spots for the sources AFGL 5142, G73.06, and G78.12. The area of the circles is proportional to the logarithm of the maser flux. The arrows indicate the direction of the thermal CH $_3$ OH outflow (Chapter 4).

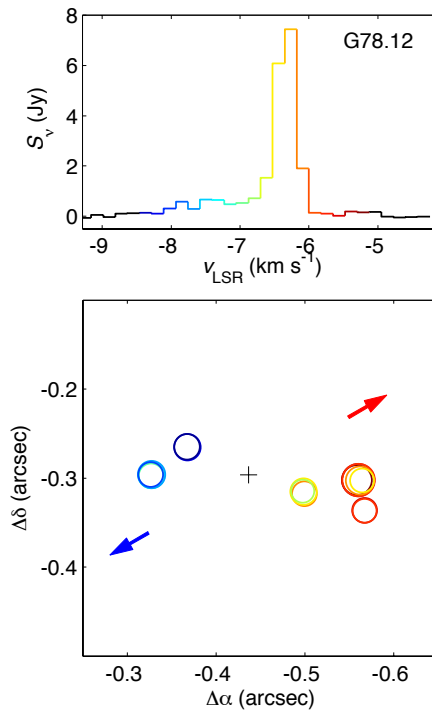


Figure 5.1: continued.

5 Dynamics of 6.7 GHz methanol masers in high-mass star-forming regions

and the individual spots are reported in Table 5.3. Furthermore, we have summarised the maser spot properties by their 2D distribution in Table 5.2. All positions are relative to the absolute positions in Table 5.1. To illustrate the details of the maser spot distribution we represent all maser spots in each velocity channel by a circle. Spurious single channel spots that do not have any neighbour in any adjacent velocity channel have been excluded. For AFGL 5142 and G73.06 the channel separation is 0.088 km s^{-1} whereas for G78.12 a channel separation of 0.176 km s^{-1} was used to improve the signal to noise ratio. The sizes of the circles are proportional to the logarithm of the maser spot intensity and the colours represent the v_{LSR} as indicated in the spectra.

For the source AFGL 5142 we are able to independently confirm the results of Goddi et al. (2007) who mapped this source at the same epoch as us with greater sensitivity (a total integration time of 12 h). The spectrum shows maser emission between $v_{\text{LSR}} = +1$ and $+5 \text{ km s}^{-1}$ and the maser distribution is complex with predominately blueshifted emission to the NW and redshifted emission to the SE. The extent of the maser emission is 184.2 mas, corresponding to 330 AU at a kinematic distance of 1.8 kpc (Snell et al. 1988). The CH_3OH maser emission is closely associated with 22 GHz radio continuum emission between two groups of H_2O masers to the NW and SE (Goddi et al. 2007).

The spectrum of G73.06 (IRAS 20062+3550) shows three CH_3OH maser emission features, one at $v_{\text{LSR}} = -2 \text{ km s}^{-1}$ and two close to $+6 \text{ km s}^{-1}$. The maser spots are grouped in two distinct clumps with the blueshifted clump to the East and the redshifted clump to the West. The clumps are separated by 342.6 mas, corresponding to 1700 AU at a kinematic distance of 4.9 kpc (Molinari et al. 2002). The maser emission is located between the two HCO^+ cores A and B at the edge of the 3.4 mm continuum emission observed by Molinari et al. (2002).

The spectrum of G78.12 (IRAS 20126+4104) shows maser emission between $v_{\text{LSR}} = -8.5$ and -5.5 km s^{-1} , with a bright main feature at -6.3 km s^{-1} . The maser spot distribution has an extent of ~ 306.0 mas, corresponding to 502 AU at a parallax distance of 1.64 kpc (Moscadelli et al. 2011) and is oriented in the East - West direction. Our results agree with earlier studies of the CH_3OH maser emission in this source (Minier et al. 2001, Edris et al. 2005, Moscadelli et al. 2011) and the maser emission appears to be originating in the NE part of the molecular disk, offset by ~ 200 mas from the protostar (Cesaroni et al. 2005).

5.4 Discussion

The aim of this work is to test our hypothesis that there is a common origin of the thermal CH_3OH emission reported in Chapter 4 and the CH_3OH maser emission reported in this chapter. In order to establish the orientation of the sources we have also included auxiliary data from the literature where available.

The seven sources studied in this chapter are all characterised by the extent of their thermal CH_3OH distribution being confined to <0.4 pc. We find that for all seven sources the CH_3OH maser position coincides to within 0.05 pc of the centre of the thermal CH_3OH emission. The errors are dominated by the pointing error of the JCMT ($\sim 1''$) (Chapter 4)

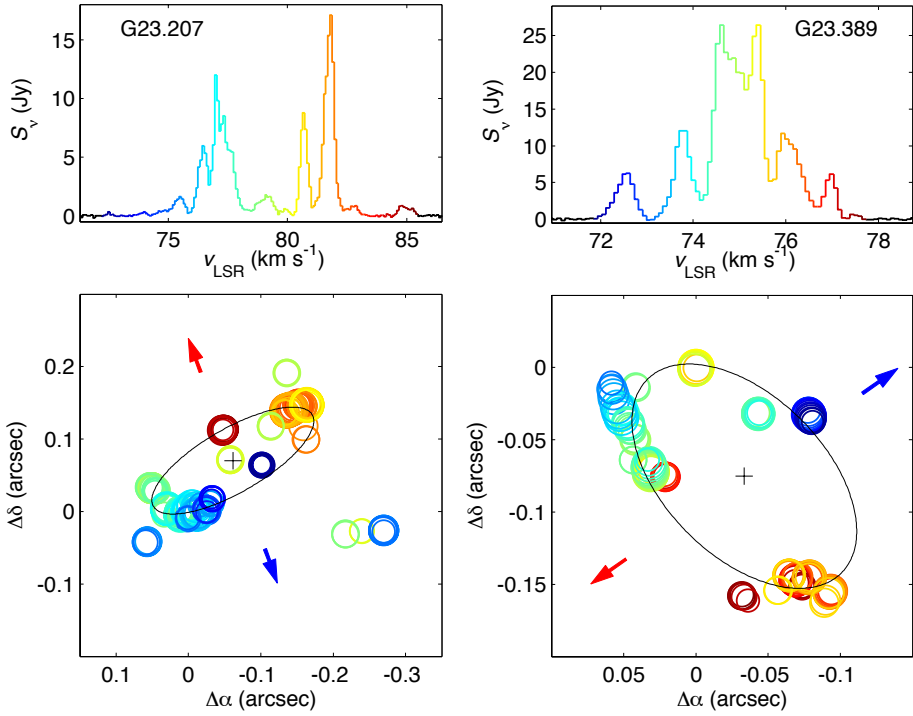


Figure 5.1: Spectrum of the maser emission and maps of the individual spots for the two sources G23.207 and G23.389 (Bartkiewicz et al. 2009). The area of the circles is proportional to the logarithm of the maser flux, also indicated is the elliptical fit of the maser distribution. The arrows indicate the direction of the thermal CH_3OH outflow (Chapter 4).

5 Dynamics of 6.7 GHz methanol masers in high-mass star-forming regions

and the large uncertainty of the (kinematic) distance estimate towards several sources. The maser distributions mapped in this chapter have sizes between $0.18''$ and $0.34''$ which corresponds to physical sizes between 330 and 1700 AU at the distance of the sources. These are typical extents of methanol masers, although for at least the source G78.12 the masers do not trace the entire circumstellar torus around the protostellar object. Initially we tested a model in which the maser spots were fitted by an ellipse and the velocity field was represented by a rotational and a radial velocity component. However, as argued below, for the three sources mapped with the EVN such an elliptical distribution is not appropriate.

It has also been argued that in at least some sources the long baselines of VLBI filter out larger scale source structure and that observations with shorter baselines are needed to recover these larger structures (Pandian et al. 2011). While we cannot show conclusively that this is not the case for the sources we have observed, we compare the VLBI spectra to those of single dish observations in the literature. The single dish observations are observed at different epochs to the VLBI observations and due to the variability of the maser emission we can only compare the general shape of the different components and the velocity span of the emission. The two sources AFGL 5142 and G78.12 (and Cep A HW2) have been observed with the Effelsberg telescope by Vlemmings (2008) and although only a fraction (10%) of the total flux is recovered in the VLBI observations, the spectra are qualitatively very similar. Likewise, the observations of Szymczak et al. (2000) with the Toruń telescope reveal that the spectra of G73.06, G23.207 and G23.389 is qualitatively very similar to the VLBI spectra of these sources with a wide range of recovered fluxes. The affinity of the VLBI spectra and the single dish spectra suggests that the VLBI maps represents the whole maser structure. The missing flux filtered out by the long VLBI baselines may arise in a more extended halo around the compact maser spots seen in the VLBI maps.

The two sources G23.207 and G23.389 have an elliptical distribution of CH_3OH masers (Bartkiewicz et al. 2009), and the major axes of the CH_3OH maser is roughly perpendicular to the velocity gradient seen in thermal methanol emission, Fig. 5.1. We interpret the thermal CH_3OH velocity gradient as an indicator of the early stages of a molecular outflow and use it to constrain the orientation of these sources. Bartkiewicz et al. (2009) fitted ellipses to the maser positions and used the velocity field of the maser spots to test a model with a radial and a rotational velocity component. However, without further constraints it is not possible to determine the sign of the velocity components. With the velocity gradient from our thermal CH_3OH observations in mind we interpret the near side of the ring to be to the NE in the case of G23.207 and to the SE in the case of G23.389. For both sources the radial velocity component found by Bartkiewicz et al. (2009) is then that of infall, similar to what was seen in Cepheus A HW2 (Chapter 2).

The remaining five sources do not show any elliptical maser distribution that can easily be used to determine the orientation and we therefore need to discuss them in some detail. Most of the sources are well studied and the recent literature can be used to determine the orientation of outflows and in some cases disks. Below we argue that in general the orientation of the thermal CH_3OH emission is in agreement with outflows seen in other molecular species and that in several cases the CH_3OH maser distribution appears to be

perpendicular to the outflows.

In the source G78.12 (IRAS 20126+4104) the methanol masers are associated with an YSO of $\sim 7 M_{\odot}$ still in its accreting phase, with a molecular disk with a position angle of 53° and an outflow roughly perpendicular to the disk (PA= -60°) (Cesaroni et al. 2005). Supporting this are the multi-epoch H_2O maser observations of Moscadelli et al. (2011) who find the water masers to trace a conical jet with a position angle of -65° , in good agreement with the molecular outflow. Our thermal CH_3OH observations show a clear velocity gradient with a similar position angle ($\sim -60^{\circ}$). The velocities and proper motions of the CH_3OH maser spots suggest that the CH_3OH masers are located in two distinct groups, the westernmost that seem to be associated with a disk/outflow interface and the easternmost that are lying in the plane of the disk (Moscadelli et al. 2011). Disregarding the second group associated with the outflow interface the methanol maser distribution is roughly perpendicular to the outflow, though they only trace a very small segment of the disk (Fig. 5.1c).

AFGL 5142 is a complex cluster with five millimetre continuum cores (MM-1–5) within $5''$ and at least three different molecular outflows (A–C) with position angles of 5° , 35° , and -60° (Zhang et al. 2007). Both H_2O and CH_3OH masers are associated with MM-1 (Hunter et al. 1999, Goddi & Moscadelli 2006, Goddi et al. 2007). The H_2O masers trace a bipolar outflow with a position angle of -40° and it is therefore thought that outflow C is associated with MM-1 (Zhang et al. 2007). Furthermore, the core MM-1 is associated with radio continuum emission at 3.6, 8.4, and 22 GHz (Goddi & Moscadelli 2006, Zhang et al. 2007). The 3.6 GHz emission is double peaked, possibly tracing a jet with a position angle of -29° . In contrast, the higher frequency centimetre emission is single peaked and centred between the two groups of H_2O masers. The CH_3OH masers are situated between the two groups of H_2O masers, close to the centre of the high frequency centimetre continuum peak. Goddi et al. (2007) proposed that while the H_2O masers trace the two outflow cones, the velocity field of the CH_3OH masers is better described by a radial infall model. Our CH_3OH maser results agree with this interpretation, although we cannot extend the analysis as the observations were performed at the same epoch. The thermal CH_3OH observations in Chapter 4 show a velocity gradient with a position angle of 20° which is in agreement with the findings of Zhang et al. (2007). It does however suggest that MM-1 may not be the major driving source of the thermal CH_3OH in the region, though they observe that there seems to be some contribution to the thermal CH_3OH from outflow “C” (Fig. 5.1a). Clearly, the lower-resolution JCMT thermal CH_3OH observations cannot be used to determine the outflow direction of the YSO associated with the maser emission and further high-resolution observations are needed to disentangle the dynamics of this cluster.

In G73.06 Molinari et al. (2002) observed a complex velocity field with four HCO^+ cores (A–D) of which core B has a 3.4 mm counterpart. The CH_3OH maser emission occurs between core A and B, on the edge of the millimetre continuum emission. The line wings of the HCO^+ emission indicate blueshifted emission to the North and redshifted emission to the South, in agreement with the velocity field seen in CO (Zhang et al. 2005). Varricatt et al. (2010) observed an outflow with position angles 43° and 212° in H_2 ($2.12 \mu m$) emission and pinned the driving source of the outflow to within $0.5''$

5 Dynamics of 6.7 GHz methanol masers in high-mass star-forming regions

of the CH₃OH maser position. It is difficult to determine any preferred direction from the thermal CH₃OH map (Chapter 4) but we note that the centre of the thermal CH₃OH ellipsoid agrees well with the maser position and the outflows seen in other tracers are perpendicular to the methanol maser distribution (Fig. 5.1b).

The two sources L1206 and G40.62 for which we were unable to map the CH₃OH maser emission have previously been studied with interferometers. Voronkov & Slysh (2002) observed L1206 with the EVN and found the CH₃OH maser emission in two clumps (“A” and “B”) separated by 200 mas and with a position angle of -65° . They argue that feature “A” may trace a disk in roughly N-S direction which would place feature “B” in the outflow. However, such velocity gradients as seen in feature “A” have been observed in many maser clumps and may be due to the nature of the maser emission and should not necessarily be interpreted as a disk signature. Nevertheless, the position of the CH₃OH maser emission is close to the centre of the centroid fitted to the thermal CH₃OH emission in Chapter 4, though it is difficult to interpret the velocity field.

G40.62 was observed with the ATCA by Beuther et al. (2002) and found to have only a single CH₃OH maser clump associated with millimetre dust continuum, H₂O masers, centimetre continuum emission, and a MIR source. The position of the CH₃OH maser is close to the centre of the ellipsoid of the thermal CH₃OH emission that has a velocity gradient in the SE-NW direction.

A further complication when comparing the AU size CH₃OH maser distribution to that of the parsec size thermal CH₃OH is the size scales on which they occur and the dynamical processes that occur. Precessing jets have been inferred in several high-mass star-forming sources (e.g., Cep A HW2 and G78.12) and it can therefore be difficult to trace the larger scale outflow back to the YSO and infer the orientation of the disk/outflow system (Cunningham et al. 2009, Cesaroni et al. 2005). To make clear the link between the CH₃OH maser emission and the thermal CH₃OH emission higher resolution studies of the thermal gas are in order.

5.5 Summary

We have mapped the 6.7 GHz CH₃OH emission in three high-mass star-forming regions. We have also included the results of four more sources from the literature for comparison with the thermal CH₃OH results in Chapter 4.

In the three CH₃OH maser sources that we have mapped, the maser emission extends over 330 – 1700 AU, similar to what has been found in other high-resolution studies of masers and in agreement with the four extra sources included in this chapter. The velocity field of the masers cover $\sim 3 - 4 \text{ km s}^{-1}$, also in agreement with what is typically found for CH₃OH maser emission.

A comparison of the VLBI spectra to single dish spectra from the literature show that although the VLBI spectra only recover a fraction of the single dish flux, in all sources, most of the components seen in the single dish spectra are present in the VLBI spectra and span a similar velocity range. This suggest that although the maser spots seen with VLBI are embedded in more extended maser emission the compact emission represents

the whole physical structure, consistent with the core/halo pattern observed by Minier et al. (2002).

The CH₃OH maser emission in all seven sources arises close to the centre (<0.05 pc) of the thermal CH₃OH emission, consistent with a single common origin of the gas phase CH₃OH gas, as was found for Cep A HW2 in Chapter 2. Furthermore, in at least three of the seven sources discussed in this chapter the maser emission seem to delineate or be part of a disk with a major axis orthogonal to a velocity gradient seen in the larger scale thermal CH₃OH emission. In some sources the velocity gradient is parallel to known molecular outflows and we suggest that the thermal CH₃OH gas is entrained in a bipolar outflow.

To probe the masing gas on size scales similar to the CH₃OH maser emission and further investigate the link between the arc second scale maser emission and the larger scale (10'' – 20'') thermal CH₃OH emission high resolution studies are required. With the advent of ALMA such high resolution studies of larger samples will now be possible. In conjunction with high-sensitivity high-resolution studies of the radio continuum emission with instruments such as the EVLA and improved distance estimates to these objects the physical processes at play can be quantified much better.

Acknowledgements

This research was supported by the EU Framework 6 Marie Curie Early Stage Training programme under contract number MEST-CT-2005-19669 "ESTRELA".

5 Dynamics of 6.7 GHz methanol masers in high-mass star-forming regions

Table 5.3: Measured maser spots in the three sources mapped.

v_{LSR} (km s^{-1})	$\Delta\alpha$ (mas)	$\Delta\delta$ (mas)	S_p (mJy beam^{-1})
AFGL 5142			
4.371	180.5	-476.3	103
4.371	246.7	-468.0	45
4.283	179.9	-475.9	112
4.283	247.0	-468.0	63
4.195	246.4	-466.9	61
4.195	177.0	-475.6	42
4.107	256.1	-461.9	253
4.107	172.6	-477.7	94
4.019	256.5	-462.2	349
4.019	172.8	-477.4	166
4.019	216.6	-281.9	56
3.932	256.5	-461.9	241
3.932	172.7	-477.4	145
3.932	218.8	-281.6	50
3.844	256.1	-462.6	75
3.756	178.0	-472.3	69
3.668	177.8	-472.0	187
3.668	282.8	-458.6	87
3.580	177.5	-471.6	379
3.580	283.6	-457.9	185
3.493	177.3	-471.6	443
3.493	284.9	-457.9	149
3.405	177.1	-471.6	304
3.405	287.1	-457.9	138
3.317	290.5	-457.6	180
3.317	176.8	-471.2	91
3.229	292.2	-457.2	154
2.176	266.2	-429.1	197
2.088	266.7	-428.8	532
2.088	315.3	-457.2	44
2.000	267.4	-428.4	466
2.000	315.4	-456.8	53
1.912	267.9	-428.4	160
1.824	176.0	-394.9	58
1.737	175.1	-392.8	445
1.649	174.0	-391.0	1209
1.649	157.8	-432.4	163
1.649	168.7	-391.7	106

Table 5.3: Continued.

v_{LSR} (km s^{-1})	$\Delta\alpha$ (mas)	$\Delta\delta$ (mas)	S_{p} (mJy beam^{-1})
1.649	213.2	-493.9	96
AFGL 5142			
1.649	116.9	-391.3	72
1.561	172.4	-389.9	1531
1.561	156.8	-430.2	241
1.561	210.9	-492.5	110
1.561	155.0	-580.0	51
1.561	222.9	-565.9	49
1.473	170.5	-389.5	907
1.473	114.8	-391.0	161
1.473	155.1	-425.2	117
1.473	183.8	-457.6	78
1.473	209.3	-491.0	75
1.473	222.9	-564.8	74
1.473	154.8	-577.1	69
1.473	220.4	-417.6	56
1.385	166.2	-389.9	360
1.385	114.0	-389.5	149
1.385	182.2	-376.6	93
1.385	231.6	-376.6	86
1.385	172.7	-381.6	79
1.385	212.9	-415.1	58
1.385	205.8	-491.0	47
1.385	181.0	-456.8	45
1.385	218.2	-565.2	45
1.298	181.9	-375.1	269
1.298	164.0	-387.4	119
1.298	231.0	-374.8	90
1.298	171.5	-378.7	73
1.298	213.1	-411.8	43
1.210	182.2	-374.0	171
1.210	170.9	-375.8	73
1.210	160.0	-379.1	50
1.210	229.3	-369.7	45
1.122	169.3	-371.5	74
1.122	159.6	-378.4	43
1.122	179.8	-369.0	41
G73.06			
6.780	362.9	694.4	25
6.692	362.5	694.4	35

5 Dynamics of 6.7 GHz methanol masers in high-mass star-forming regions

Table 5.3: Continued.

v_{LSR} (km s^{-1})	$\Delta\alpha$ (mas)	$\Delta\delta$ (mas)	S_{p} (mJy beam^{-1})
6.604	362.5	694.4	33
6.517	362.5	693.4	20
6.429	362.9	693.7	10
6.078	362.2	689.4	18
5.990	361.8	689.4	87
5.902	361.1	689.4	80
5.814	360.7	689.0	51
5.726	359.1	689.0	15
-2.351	696.6	625.3	13
-2.439	696.2	625.0	53
-2.527	696.6	625.0	79
-2.615	695.9	624.6	45
-2.702	696.2	623.5	19
-2.790	695.2	621.4	12
-2.878	694.1	620.3	13
-2.966	692.3	619.2	14
-3.054	691.9	619.6	24
-3.141	691.2	618.1	15
G78.12			
-6.000	-558.7	-301.9	1454
-6.176	-559.8	-301.9	5827
-6.176	-567.0	-336.4	146
-6.351	-560.5	-302.3	4689
-6.351	-567.4	-336.5	114
-6.527	-562.0	-302.5	778
-6.527	-499.7	-317.3	152
-6.702	-498.6	-315.3	254
-6.702	-564.5	-302.4	110
-6.878	-497.5	-314.4	81
-7.054	-327.1	-297.5	170
-7.229	-327.5	-296.4	352
-7.405	-327.5	-296.0	477
-7.580	-326.8	-296.0	170
-7.756	-367.9	-265.4	266
-7.932	-367.6	-265.0	207

Bibliography

- Ball, J. A., Gottlieb, C. A., Lilley, A. E., & Radford, H. E. 1970, *ApJ*, 162, L203+
- Bartkiewicz, A., Brunthaler, A., Szymczak, M., van Langevelde, H. J., & Reid, M. J. 2008, *A&A*, 490, 787
- Bartkiewicz, A., Szymczak, M., Cohen, R. J., & Richards, A. M. S. 2005a, *MNRAS*, 361, 623
- Bartkiewicz, A., Szymczak, M., Pihlström, Y. M., et al. 2011, *A&A*, 525, A120+
- Bartkiewicz, A., Szymczak, M., & van Langevelde, H. J. 2005b, *A&A*, 442, L61
- Bartkiewicz, A., Szymczak, M., van Langevelde, H. J., Richards, A. M. S., & Pihlström, Y. M. 2009, *A&A*, 502, 155
- Beltrán, M. T., Girart, J. M., & Estalella, R. 2006, *A&A*, 457, 865
- Beuther, H., Churchwell, E. B., McKee, C. F., & Tan, J. C. 2007a, *Protostars and Planets V*, 165
- Beuther, H., Walsh, A., Schilke, P., et al. 2002, *A&A*, 390, 289
- Beuther, H., Zhang, Q., Bergin, E. A., et al. 2007b, *A&A*, 468, 1045
- Beuther, H., Zhang, Q., Hunter, T. R., Sridharan, T. K., & Bergin, E. A. 2007c, *A&A*, 473, 493
- Bisschop, S. E., Jørgensen, J. K., van Dishoeck, E. F., & de Wachter, E. B. M. 2007, *A&A*, 465, 913
- Blake, G. A., Sutton, E. C., Masson, C. R., & Phillips, T. G. 1987, *ApJ*, 315, 621
- Bonnell, I. A. & Bate, M. R. 2005, *MNRAS*, 362, 915
- Bonnell, I. A., Bate, M. R., & Zinnecker, H. 1998, *MNRAS*, 298, 93
- Bottinelli, S. & Williams, J. P. 2004, *A&A*, 421, 1113
- Bourke, S., van Langevelde, H. J., Harvey-Smith, L., & Golden, A. 2006, in *Proceedings of the 8th European VLBI Network Symposium*
- Breen, S. L., Ellingsen, S. P., Caswell, J. L., & Lewis, B. E. 2010, *MNRAS*, 401, 2219
- Brogan, C. L., Chandler, C. J., Hunter, T. R., Shirley, Y. L., & Sarma, A. P. 2007, *ApJ*, 660, L133
- Buckle, J. V., Hills, R. E., Smith, H., et al. 2009, *MNRAS*, 399, 1026
- Caswell, J. L., Fuller, G. A., Green, J. A., et al. 2010, *MNRAS*, 404, 1029

BIBLIOGRAPHY

- Caswell, J. L., Vaile, R. A., Ellingsen, S. P., Whiteoak, J. B., & Norris, R. P. 1995, *MNRAS*, 272, 96
- Cesaroni, R., Felli, M., Jenness, T., et al. 1999, *A&A*, 345, 949
- Cesaroni, R., Neri, R., Olmi, L., et al. 2005, *A&A*, 434, 1039
- Chandler, C. J., Gear, W. K., & Chini, R. 1993, *MNRAS*, 260, 337
- Collings, M. P., Anderson, M. A., Chen, R., et al. 2004, *MNRAS*, 354, 1133
- Comito, C., Schilke, P., Endesfelder, U., Jiménez-Serra, I., & Martín-Pintado, J. 2007, *A&A*, 469, 207
- Cragg, D. M., Johns, K. P., Godfrey, P. D., & Brown, R. D. 1992, *MNRAS*, 259, 203
- Cragg, D. M., Sobolev, A. M., & Godfrey, P. D. 2005, *MNRAS*, 360, 533
- Crowther, P. A., Schnurr, O., Hirschi, R., et al. 2010, *MNRAS*, 408, 731
- Cunningham, N. J., Moeckel, N., & Bally, J. 2009, *ApJ*, 692, 943
- Curiel, S., Ho, P. T. P., Patel, N. A., et al. 2006, *ApJ*, 638, 878
- Davis, C. J., Kumar, M. S. N., Sandell, G., et al. 2007, *MNRAS*, 374, 29
- De Buizer, J. M. 2003, *MNRAS*, 341, 277
- Doty, S. D., van Dishoeck, E. F., van der Tak, F. F. S., & Boonman, A. M. S. 2002, *A&A*, 389, 446
- Edris, K. A., Fuller, G. A., Cohen, R. J., & Etoke, S. 2005, *A&A*, 434, 213
- Elitzur, M. 1992, *ARA&A*, 30, 75
- Elitzur, M., Hollenbach, D. J., & McKee, C. F. 1989, *ApJ*, 346, 983
- Ellingsen, S. P., von Bibra, M. L., McCulloch, P. M., et al. 1996, *MNRAS*, 280, 378
- Evans, II, N. J. 1999, *ARA&A*, 37, 311
- Evans, II, N. J., Slovak, M. H., Becklin, E. E., et al. 1981, *ApJ*, 244, 115
- Fuchs, G. W., Cuppen, H. M., Ioppolo, S., et al. 2009, *A&A*, 505, 629
- Garay, G., Ramirez, S., Rodriguez, L. F., Curiel, S., & Torrelles, J. M. 1996, *ApJ*, 459, 193
- Gaylard, M. J. & MacLeod, G. C. 1993, *MNRAS*, 262, 43
- Gibb, E. L., Whittet, D. C. B., Boogert, A. C. A., & Tielens, A. G. G. M. 2004, *ApJS*, 151, 35
- Goddi, C. & Moscadelli, L. 2006, *A&A*, 447, 577
- Goddi, C., Moscadelli, L., Sanna, A., Cesaroni, R., & Minier, V. 2007, *A&A*, 461, 1027
- Goldsmith, P. F. & Langer, W. D. 1999, *ApJ*, 517, 209
- Gómez, J. F., Sargent, A. I., Torrelles, J. M., et al. 1999, *ApJ*, 514, 287
- Green, J. A., Caswell, J. L., Fuller, G. A., et al. 2009, *MNRAS*, 392, 783
- Green, J. A., Caswell, J. L., Fuller, G. A., et al. 2010, *MNRAS*, 409, 913
- Harvey-Smith, L. & Cohen, R. J. 2006, *MNRAS*, 371, 1550
- Helmich, F. P., Jansen, D. J., de Graauw, T., Groesbeck, T. D., & van Dishoeck, E. F. 1994, *A&A*, 283, 626
- Helmich, F. P. & van Dishoeck, E. F. 1997, *A&AS*, 124, 205
- Henning, T., Schreyer, K., Launhardt, R., & Burkert, A. 2000, *A&A*, 353, 211
- Herbst, E. & van Dishoeck, E. F. 2009, *ARA&A*, 47, 427

- Hill, T., Burton, M. G., Minier, V., et al. 2005, *MNRAS*, 363, 405
- Hughes, V. A. & Wouterloot, J. G. A. 1984, *ApJ*, 276, 204
- Hunter, T. R., Testi, L., Taylor, G. B., et al. 1995, *A&A*, 302, 249
- Hunter, T. R., Testi, L., Zhang, Q., & Sridharan, T. K. 1999, *AJ*, 118, 477
- Jiménez-Serra, I., Martín-Pintado, J., Caselli, P., et al. 2009, *ApJ*, 703, L157
- Jiménez-Serra, I., Martín-Pintado, J., Rodríguez-Franco, A., et al. 2007, *ApJ*, 661, L187
- Jørgensen, J. K., Schöier, F. L., & van Dishoeck, E. F. 2002, *A&A*, 389, 908
- Keto, E. 2003, *ApJ*, 599, 1196
- Kettenis, M., van Langevelde, H. J., Reynolds, C., & Cotton, B. 2006, in *Astronomical Society of the Pacific Conference Series*, Vol. 351, *Astronomical Data Analysis Software and Systems XV*, ed. C. Gabriel, C. Arviset, D. Ponz, & S. Enrique, 497
- Kurtz, S. 2005, in *IAU Symposium*, Vol. 227, *Massive Star Birth: A Crossroads of Astrophysics*, ed. R. Cesaroni, M. Felli, E. Churchwell, & M. Walmsley, 111–119
- Leurini, S., Schilke, P., Menten, K. M., et al. 2004, *A&A*, 422, 573
- Leurini, S., Schilke, P., Wyrowski, F., & Menten, K. M. 2007, *A&A*, 466, 215
- López-Sepulcre, A., Cesaroni, R., & Walmsley, C. M. 2010, *A&A*, 517, A66+
- Maret, S., Ceccarelli, C., Tielens, A. G. G. M., et al. 2005, *A&A*, 442, 527
- Martín-Pintado, J., Jiménez-Serra, I., Rodríguez-Franco, A., Martín, S., & Thum, C. 2005, *ApJ*, 628, L61
- McKee, C. F. & Tan, J. C. 2003, *ApJ*, 585, 850
- Menten, K. 1991a, in *Astronomical Society of the Pacific Conference Series*, Vol. 16, *Atoms, Ions and Molecules: New Results in Spectral Line Astrophysics*, ed. A. D. Haschick & P. T. P. Ho, 119
- Menten, K. M. 1991b, *ApJ*, 380, L75
- Menten, K. M., Reid, M. J., Forbrich, J., & Brunthaler, A. 2007, *A&A*, 474, 515
- Menten, K. M., Walmsley, C. M., Henkel, C., & Wilson, T. L. 1986, *A&A*, 157, 318
- Menten, K. M., Walmsley, C. M., Henkel, C., & Wilson, T. L. 1988, *A&A*, 198, 253
- Minier, V., Booth, R. S., & Conway, J. E. 2000, *A&A*, 362, 1093
- Minier, V., Booth, R. S., & Conway, J. E. 2002, *A&A*, 383, 614
- Minier, V., Conway, J. E., & Booth, R. S. 2001, *A&A*, 369, 278
- Minier, V., Ellingsen, S. P., Norris, R. P., & Booth, R. S. 2003, *A&A*, 403, 1095
- Molinari, S., Testi, L., Rodríguez, L. F., & Zhang, Q. 2002, *ApJ*, 570, 758
- Moscadelli, L., Cesaroni, R., & Rioja, M. J. 2005, *A&A*, 438, 889
- Moscadelli, L., Cesaroni, R., Rioja, M. J., Dodson, R., & Reid, M. J. 2011, *A&A*, 526, A66+
- Moscadelli, L., Reid, M. J., Menten, K. M., et al. 2009, *ApJ*, 693, 406
- Motte, F., Bontemps, S., Schilke, P., et al. 2007, *A&A*, 476, 1243
- Müller, H. S. P., Schlöder, F., Stutzki, J., & Winnewisser, G. 2005, *Journal of Molecular Structure*, 742, 215
- Norris, R. P., Byleveld, S. E., Diamond, P. J., et al. 1998, *ApJ*, 508, 275
- Panagia, N. 1973, *AJ*, 78, 929

BIBLIOGRAPHY

- Pandian, J. D., Leurini, S., Menten, K. M., Belloche, A., & Goldsmith, P. F. 2008, *A&A*, 489, 1175
- Pandian, J. D., Menten, K. M., & Goldsmith, P. F. 2009, *ApJ*, 706, 1609
- Pandian, J. D., Momjian, E., Xu, Y., Menten, K. M., & Goldsmith, P. F. 2010, *A&A*, 522, A8+
- Pandian, J. D., Momjian, E., Xu, Y., Menten, K. M., & Goldsmith, P. F. 2011, *ApJ*, 730, 55
- Patel, N. A., Curiel, S., Sridharan, T. K., et al. 2005, *Nature*, 437, 109
- Pestalozzi, M. R., Elitzur, M., Conway, J. E., & Booth, R. S. 2004, *ApJ*, 603, L113
- Phillips, C. J., Norris, R. P., Ellingsen, S. P., & McCulloch, P. M. 1998, *MNRAS*, 300, 1131
- Pottage, J. T., Flower, D. R., & Davis, S. L. 2004, *MNRAS*, 352, 39
- Reid, M. J., Menten, K. M., Brunthaler, A., et al. 2009a, *ApJ*, 693, 397
- Reid, M. J., Menten, K. M., Zheng, X. W., et al. 2009b, *ApJ*, 700, 137
- Roy, A., Ade, P. A. R., Bock, J. J., et al. 2011, *ApJ*, 727, 114
- Rygl, K. L. J., Brunthaler, A., Reid, M. J., et al. 2010, *A&A*, 511, A2
- Rygl, K. L. J., Brunthaler, A., Sanna, A., et al. 2011, *A&A*, submitted
- Schneider, N., Bontemps, S., Simon, R., et al. 2006, *A&A*, 458, 855
- Schneider, N., Csengeri, T., Bontemps, S., et al. 2010, *A&A*, 520, A49+
- Schöier, F. L., van der Tak, F. F. S., van Dishoeck, E. F., & Black, J. H. 2005, *A&A*, 432, 369
- Schutte, A. J., van der Walt, D. J., Gaylard, M. J., & MacLeod, G. C. 1993, *MNRAS*, 261, 783
- Snell, R. L., Huang, Y., Dickman, R. L., & Claussen, M. J. 1988, *ApJ*, 325, 853
- Sobolev, A. M., Cragg, D. M., & Godfrey, P. D. 1997, *A&A*, 324, 211
- Sobolev, A. M. & Deguchi, S. 1994, *A&A*, 291, 569
- Stecklum, B., Brandl, B., Henning, T., et al. 2002, *A&A*, 392, 1025
- Sugiyama, K., Fujisawa, K., Doi, A., et al. 2008a, *PASJ*, 60, 1001
- Sugiyama, K., Fujisawa, K., Doi, A., et al. 2008b, *PASJ*, 60, 23
- Sugiyama, K., Fujisawa, K., Honma, M., et al. 2007, in *IAU Symposium*, Vol. 242, IAU Symposium, ed. J. M. Chapman & W. A. Baan, 176–177
- Sun, Y. & Gao, Y. 2009, *MNRAS*, 392, 170
- Surcis, G., Vlemmings, W. H. T., Curiel, S., et al. 2011, *A&A*, 527, A48+
- Szymczak, M., Hrynek, G., & Kus, A. J. 2000, *A&AS*, 143, 269
- Szymczak, M., Wolak, P., Bartkiewicz, A., & van Langevelde, H. J. 2011, *A&A*, 531, L3+
- Thompson, A. R., Moran, J. M., & Swenson, Jr., G. W. 2001, *Interferometry and Synthesis in Radio Astronomy*, 2nd Edition, ed. Thompson, A. R., Moran, J. M., & Swenson, G. W., Jr.
- Torrelles, J. M., Gómez, J. F., Garay, G., et al. 1998, *ApJ*, 509, 262
- Torrelles, J. M., Patel, N., Curiel, S., et al. 2010, *A&A*, submitted

BIBLIOGRAPHY

- Torrelles, J. M., Patel, N. A., Curiel, S., et al. 2011, *MNRAS*, 410, 627
- Torrelles, J. M., Patel, N. A., Curiel, S., et al. 2007, *ApJ*, 666, L37
- Torstensson, K. J. E., van Langevelde, H. J., Vlemmings, W. H. T., & Bourke, S. 2011, *A&A*, 526, A38+
- van der Tak, F. F. S., Black, J. H., Schöier, F. L., Jansen, D. J., & van Dishoeck, E. F. 2007, *A&A*, 468, 627
- van der Tak, F. F. S., Boonman, A. M. S., Braakman, R., & van Dishoeck, E. F. 2003, *A&A*, 412, 133
- van der Tak, F. F. S., van Dishoeck, E. F., & Caselli, P. 2000a, *A&A*, 361, 327
- van der Tak, F. F. S., van Dishoeck, E. F., Evans, II, N. J., & Blake, G. A. 2000b, *ApJ*, 537, 283
- van der Walt, D. J., Gaylard, M. J., & MacLeod, G. C. 1995, *A&AS*, 110, 81
- van Dishoeck, E. F. & Blake, G. A. 1998, *ARA&A*, 36, 317
- Varricatt, W. P., Davis, C. J., Ramsay, S., & Todd, S. P. 2010, *MNRAS*, 404, 661
- Vlemmings, W. H. T. 2008, *A&A*, 484, 773
- Vlemmings, W. H. T., Diamond, P. J., van Langevelde, H. J., & Torrelles, J. M. 2006, *A&A*, 448, 597
- Vlemmings, W. H. T., Surcis, G., Torstensson, K. J. E., & van Langevelde, H. J. 2010, *MNRAS*, 404, 134
- Voronkov, M. A. & Slysh, V. I. 2002, in *IAU Symposium*, Vol. 206, *Cosmic Masers: From Proto-Stars to Black Holes*, ed. V. Migenes & M. J. Reid, 163
- Walsh, A. J., Bertoldi, F., Burton, M. G., & Nikola, T. 2001, *MNRAS*, 326, 36
- Walsh, A. J., Burton, M. G., Hyland, A. R., & Robinson, G. 1998, *MNRAS*, 301, 640
- Walsh, A. J., Hyland, A. R., Robinson, G., & Burton, M. G. 1997, *MNRAS*, 291, 261
- Walsh, A. J., Macdonald, G. H., Alvey, N. D. S., Burton, M. G., & Lee, J. 2003, *A&A*, 410, 597
- Wang, K., Kuan, Y., Liu, S., & Charnley, S. B. 2010, *ApJ*, 713, 1192
- Wang, Y., Beuther, H., Bik, A., et al. 2011, *A&A*, 527, A32+
- Watanabe, N., Nagaoka, A., Shiraki, T., & Kouchi, A. 2004, *ApJ*, 616, 638
- Watanabe, N., Shiraki, T., & Kouchi, A. 2003, *ApJ*, 588, L121
- Wyrowski, F., Schilke, P., Walmsley, C. M., & Menten, K. M. 1999, *ApJ*, 514, L43
- Xu, Y., Li, J. J., Hachisuka, K., et al. 2008, *A&A*, 485, 729
- Xu, Y., Reid, M. J., Zheng, X. W., & Menten, K. M. 2006, *Science*, 311, 54
- Zhang, Q., Hunter, T. R., Beuther, H., et al. 2007, *ApJ*, 658, 1152
- Zhang, Q., Hunter, T. R., Brand, J., et al. 2005, *ApJ*, 625, 864
- Zhang, Q., Hunter, T. R., Sridharan, T. K., & Ho, P. T. P. 2002, *ApJ*, 566, 982
- Zinnecker, H. & Yorke, H. W. 2007, *ARA&A*, 45, 481

Stervorming

Zware sterren, reuzen, spelen een belangrijke rol, zowel bij de evolutie van ons Melkwegstelsel, alsook voor ons bestaan in de ruimste betekenis. Hoe zwaarder een ster, des te korter is zijn levensduur en hoe spectaculairder zijn dood. Reuzen voorzien in een grote hoeveelheid mechanische energie en intense ultraviolette straling door middel van krachtige straalstromen, sterrenwinden en uiteindelijk ook als explosieve supernovae. Bovendien verrijken zij het interstellair medium met zware elementen. In feite bestaan wij allemaal voornamelijk uit sterrenstof van vroegere sterren zwaarder dan onze zon. Toch is ons inzicht in het ontstaan van zulke reuzensterren beperkt, grotendeels ten gevolge van de beperkingen die de waarnemingen aan hun ontstaan ondervinden. Reuzen worden gevormd in die gebieden van moleculaire wolken waar zich de grootste dichtheden ophopen en kunnen daarom niet worden waargenomen bij optische golflengtes. Omdat ze juist ontstaan in deze gebieden, worden ze vaak in clusters gevormd en is het dus moeilijk om te kunnen onderscheiden wat er precies gebeurt. Een ander probleem is dat reuzen zeldzaam zijn, doordat zij sneller evolueren dan lichte sterren. Een consequentie daarvan is dat ze gemiddeld op veel grotere afstanden gevonden worden dan dwergen, wat weer betekent dat de waarnemingen moeten worden gedaan met een groter oplossend vermogen.

Sterren ontstaan als gevolg van de ineenstorting van een moleculaire gaswolk onder invloed van zijn eigen zwaartekracht (zie figuur 1.1). In zo'n gaswolk kan de gasdruk de zwaartekracht enigszins compenseren. Maar de wolk zal ineenstorten als de gasdruk te laag is of de massa te groot. Andere fysische processen, zoals de aanwezigheid van magnetische velden en turbulentie kunnen het ineenstorten en fragmenteren van de wolk ook beïnvloeden. Bij het samentrekken van de wolk komt er gravitatie-energie vrij die via straling kan ontsnappen. Wanneer de wolk echter een steeds grotere dichtheid krijgt, wordt deze minder transparant en als de stralingskoeling niet meer efficiënt is, zal de temperatuur van de wolk stijgen. Op een gegeven moment gaat de ster 'aan' en brandt dan eerst op deuterium en vervolgens op waterstof. Op dat moment neemt de stralingsdruk drastisch toe. Theoretisch werk laat zien dat voor het ineenstorten van een bolvormige wolk de stralingsdruk de zwaartekracht opheft, wat ervoor zorgt dat sterren niet zwaarder kunnen worden dan acht zonnemassa's. Dit wordt echter niet onderschreven door de prak-

Nederlandse Samenvatting

tijk; veel zwaardere sterren zijn immers waargenomen en moeten dus via een onbekend mechanisme zijn ontstaan.

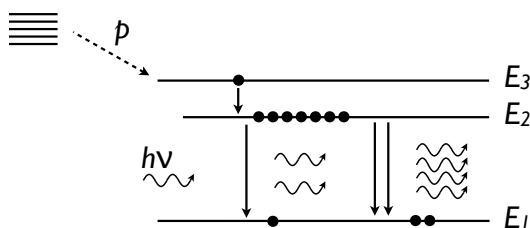
Er bestaan verschillende theorieën voor de vorming van reuzen. Momenteel zijn de twee belangrijkste theorieën de competitieve accretie en de monolitische ineenstorting. De twee scenario's verschillen voornamelijk in hoe wolkfragmenten individuele kernen worden, waaruit dan weer één of meerdere sterren ontstaan. Ondanks de overeenkomsten tussen beide modellen, hebben ze bijzonder verschillende implicaties voor de efficiëntie van de vorming van sterren. In het competitieve accretie model wordt bijna al het gas omgezet in sterren terwijl de monolitische ineenstorting voorspelt dat slechts een klein deel van het gas voor stervorming wordt gebruikt. In principe is dit een opgeschaalde versie van de vorming van gewone, lichte sterren waarbij accretie via een schijf plaatsvindt om zo de stralingsdruk te overwinnen. Vandaag de dag is de monolitische ineenstorting het meest gesteunde scenario.

Moleculen in de ruimte

Eén van de methoden die gebruikt wordt om het binnenste van wolken waar sterren ontstaan te onderzoeken, is het waarnemen van moleculaire emissie lijnen. Tijdens het ineenstorten en de gravitationele opwarming kan een keur aan chemische reacties plaats vinden in het koude ijs op de interstellaire stofdeeltjes en zo kunnen complexe moleculen ontstaan. Wanneer de temperatuur van de wolk verder stijgt, sublimeren deze moleculen waarna hun emissie in de gas fase kan worden waargenomen. Deze emissie vindt plaats in het millimeter en sub-millimeter gebied van het electromagnetisch spectrum. Het licht van deze grote golflengtes kan zich door de dichte wolken voortplanten en na een ruimtereis van enkele duizenden jaren ons hier op aarde bereiken, waar wij het kunnen waarnemen. Tot op heden zijn er bijna 170 moleculen geïdentificeerd in de ruimte. Sommige van deze moleculen kunnen worden gebruikt om de fysische condities te onderzoeken van de gebieden waar reuzensterren ontstaan. Door verschillende spectrale overgangen van een molecuul als methanol (CH_3OH) waar te nemen, kan de hoeveelheid methanol worden afgeschat en daarmee ook de temperatuur van het gas en de dichtheid van de wolk.

Maser emissie

Eén emissiemechanisme waar hier in het bijzonder aandacht aan wordt besteed, is de zogenaamde Microgolf Amplificatie door Gestimuleerde Emissie van Straling (Engels: Microwave Amplification by Stimulated Emission of Radiation - MASER). Dit is het equivalent van een LASER, maar dan voor langere golflengtes. In de ruimte kan maser emissie plaatsvinden als er een populatie-inversie van het gas is, dat wil zeggen, wanneer meer moleculen zich in een hoog aangeslagen toestand bevinden dan in een lagere energie-toestand. Een foton met de juiste energie of golflengte kan dan de emissie van een volgend, coherent foton stimuleren (figuur 1). Dit tweede foton is identiek aan het eerste en samen kunnen zij nogmaals twee fotonen stimuleren, enzovoorts. Het resultaat is een



Figuur 1: Een schema van het maser emissie principe.

exponentiële toename in de foton flux langs het pad van zo'n maser. In dit proefschrift ligt de nadruk op de 6.7 GHz (4.5 cm) CH₃OH maser. Deze specifieke maser wordt alleen waargenomen in de richting van plekken waar reuzen ontstaan en kan daarom worden gezien als een baken van het vroegste stadium waarin een reus geboren wordt. Het is echter meer dan alleen een baken, omdat de maser emissie zo helder is dat we deze objecten kunnen waarnemen met 'Very Long Baseline Interferometry' (VLBI), dat het grootst mogelijke oplossend vermogen biedt. Daarom kunnen we de kinematica bestuderen en onderzoek doen aan de fysische condities op zeer kleine schaal, vlakbij het protostellare object.

Radio Interferometrie

De resolutie van een telescoop bestaand uit een enkele schotel wordt bepaald door de waargenomen golflengte en de diameter van de telescoop. Idealiter bestudeert een astronoom zijn objecten met optische telescopen en radio telescopen van vergelijkbare resolutie. Maar radiogolven hebben langere golflengtes en daarom zou men eigenlijk gebruik moeten maken van telescopen die zo groot zijn, dat dat fysiek niet haalbaar is. De manier om de resolutie te vergroten is het combineren van het signaal van verschillende telescopen door middel van interferometrie om zo een veel groter instrument te creëren. De resolutie wordt dan bepaald door de afstand tussen de twee telescopen. Echter, voor deze hogere resolutie moet ook een prijs betaald worden. Het blijkt dat hoewel de resolutie groter wordt, de helderheid van het object ook groter moet zijn om gedetecteerd te kunnen worden. Voor VLBI komen alleen niet-thermische emissie mechanismen, zoals maser emissie, in aanmerking.

Dit proefschrift

Het doel van dit proefschrift is om de relatie te onderzoeken tussen de 6.7 GHz maser emissie, de protoster(ren) die verantwoordelijk zijn voor de verhoogde excitatie en de thermische CH₃OH emissie. Meer specifiek is er gekeken naar waar de CH₃OH maser



Figuur 2: De Onsala Space Observatory (Zweden) in de winter. Aan de rechterkant staat de 25 m telescoop en links de radome met de 20 m antenne. Beide telescopen worden gebruikt voor VLBI waarnemingen en zijn deel van het Europese VLBI Netwerk. Credit: Onsala Space Observatory/Magnus Thomasson

emissie ontstaat in relatie tot de protoster en wat de excitatie omstandigheden van het ‘maserende’ gas zijn. Om dit te kunnen doen, is een set van 14 CH_3OH maser objecten bestudeerd bij verschillende golflengtes en aan de hand van verschillende emissie mechanismen. De set omvat enkele van de dichtstbijzijnde gebieden waar reuzen vormen.

In Hoofdstuk 2 wordt een gedetailleerde studie van de 6.7 GHz en 12.2 GHz CH_3OH maser emissie in Cepheus A HW2 gepresenteerd, gebaseerd op VLBI waarnemingen. Het object HW2 is een protoster met een massa van ongeveer 20 zonsmassa’s, op een afstand van 700 pc. Cep A is één van de dichtstbijzijnde gebieden waar reuzen vormen. De CH_3OH maser vormt een filamentachtige boog langs de equator van de protoster, loodrecht op de thermische jet die waargenomen is bij radio golflengten. De kinematica van de masers locaties suggereert dat een invallende stroming prevaleert over rotatie, zoals je misschien aanvankelijk zou verwachten. We laten hier zien dat de CH_3OH masers voorkomen in (de buurt van) een schok op het grensvlak tussen de feitelijke accretie schijf en de wolk met het invallende materiaal dat daaromheen ligt. Dit beeld is consistent met metingen van het magnetisch veld.

In Hoofdstuk 3 worden sub-millimeter waarnemingen van het thermische CH_3OH gas in Cep A gepresenteerd, die uitgevoerd zijn met de James Clerk Maxwell Telescope. De distributie en excitatie van het CH_3OH gas op grote lengteschalen is in kaart gebracht. Het uitgebreide gas heeft een relatief lage temperatuur en het snelheidsveld suggereert dat het gas meegevoerd wordt door een straalstroom. Op de positie van de protoster HW2 wordt echter een tweede gas component waargenomen met een veel hogere excitatie. Deze tweede component is waarschijnlijk geassocieerd met de maser emissie, ondanks dat de

resolutie van onze waarnemingen te laag is om dit in detail te kunnen bestuderen.

Dezelfde observationele technieken en methodologieën die gebruikt zijn in Hoofdstuk 3, zijn toegepast op een set van 13 objecten die met 6.7 GHz CH_3OH maser emissie. Dit wordt beschreven in Hoofdstuk 4. Eén van de conclusies is dat de helft van de objecten een compacte CH_3OH gasdistributie hebben die zijn maximum heeft vlakbij de positie van de maser emissie. Voorts suggereert het lineaire snelheidsveld langs de hoofdas dat het thermische gas meegevoerd wordt in een straalstroom. In verschillende objecten zijn aanwijzingen van hoog geëxciteerd gas waargenomen. Waarschijnlijk gebeurt dit op de positie van de maser, maar met de huidige data is het onmogelijk deze excitatie tot in detail te bestuderen.

In Hoofdstuk 5 wordt een VLBI studie gepresenteerd naar de CH_3OH emissie in de richting van de compacte objecten uit Hoofdstuk 4. Ondanks dat de VLBI waarnemingen typisch slechts een fractie van de totale maser flux detecteren, zijn de contouren van de jonge sterren herkenbaar en kunnen we concluderen dat de VLBI data een representatie zijn van de totale fysieke structuur. De maser emissie komt voor op ruimtelijke schalen van een paar honderd tot een paar duizend astronomische eenheden, wat goed overeenkomt met eerdere studies. Voorts blijken de CH_3OH masers in de helft van de objecten onderdeel te zijn van een schijf of torus in de equatoriale regio van de reuzen-protoster, waarbij de invallende beweging te onderscheiden is. De oriëntatie van de schijf/torus is loodrecht op de thermische snelheidsgradiënt van methanol, wat de hypothese onderschrijft dat het uitgebreide gas meegevoerd wordt in een straalstroom.

Tot slot; we hebben laten zien dat voor een redelijke hoeveelheid van de objecten de methanol masers voorkomen op een ruimtelijke schaal van ongeveer 1000 AU, in de equatoriale regio van de reusachtige protoster. Het lijkt erop dat de invallende beweging belangrijker is dan de roterende beweging. Wij stellen voor dat de maser emissie plaatsvindt vlakbij, of in een geschokt grensvlak, wat mogelijk gerelateerd is aan de accretiestroom van de protostellare wolk naar de accretie schijf. De morfologie en kinematica van het thermische CH_3OH gas onderschrijft de hypothese dat de maser omgeving ook het gebied is waar de CH_3OH moleculen los worden gemaakt uit het koude ijs op stofdeeltjes. We hebben ook een afschatting gemaakt van de temperatuur en kolomdichtheid van het CH_3OH gas in de straalstromen en hebben bewijs gevonden voor excitatie ten gevolge van straling van het CH_3OH gas op de locatie van de maser emissie.

Refereed papers

- *Parallaxes and proper motions of interstellar masers toward the Cygnus X star-forming complex I. Membership of the Cygnus X region*
Rygl, K. L. J., Brunthaler, A., Sanna, A., Menten, K. M., Reid, M. J., van Langevelde, H. J., Honma, M., **Torstensson, K. J. E.**, & Fujisawa, K. Submitted to A&A
- *Distribution and excitation of thermal methanol in 6.7 GHz maser bearing star-forming regions. I. The nearby source Cepheus A*
Torstensson, K. J. E., van der Tak, F. F. S., van Langevelde, H. J., Kristensen, L. E., & Vlemmings, W. H. T. 2011, A&A, 529, A32 (Chapter 3)
- *Dynamics of the 6.7 and 12.2 GHz methanol masers around Cepheus A HW2*
Torstensson, K. J. E., van Langevelde, H. J., Vlemmings, W. H. T., & Bourke S. 2011, A&A, 526, A38 (Chapter 2)
- *Magnetic field regulated infall on the disc around the massive protostar Cepheus A HW2*
Vlemmings, W. H. T., Surcis, G., **Torstensson, K. J. E.**, & van Langevelde, H. J. 2010, MNRAS, 404, 134
- *A $\log N_{\text{HI}} = 22.6$ damped Ly α absorber in a dark gamma-ray burst: the environment of GRB 050401*
Watson, D., Fynbo, J. P. U., Ledoux, C., and 33 other authors including **Torstensson, K. J. E.** 2006, ApJ, 652, 1011

Conference Proceedings

- *A preliminary distance to W75N in the Cygnus X star-forming region*
Rygl, K., Brunthaler, A., Menten, K. M., Reid, M. J., van Langevelde, H. J., Honma, M., **Torstensson, K. J. E.**, Fujisawa, K., & Sanna, A. Proceedings of the 10th European VLBI network symposium and EVN users meeting: “VLBI and the new generation of radio arrays”. September 20-24, 2010. Manchester, UK. POS, id. 103
- *The magic of disc-worlds: non-rotating methanol masers*
van Langevelde, H. J., **Torstensson, K. J. E.**, Bartkiewicz, A., Szymczak, M., Vlemmings, W. H. T., Surcis, G., & Brunthaler, A. Proceedings of the 10th European VLBI network symposium and EVN users meeting: “VLBI and the new generation of radio arrays”. September 20-24, 2010. Manchester, UK. POS, id. 2
- *EVN observations of the methanol masers in Cep A*
Torstensson, K. J. E., van Langevelde, H. J., Vlemmings, W. H. T., & van der Tak, F. F. S. Proceedings of the 9th European VLBI network symposium on “The role of VLBI in the golden age for radio astronomy” and EVN users meeting. September 23-26, 2008. Bologna, Italy. POS, p. 39
- *Where methanol masers spring*
Torstensson, K. J. E., van Langevelde, H. J., & Bourke, S. “Astrophysical masers and their environments”, Proceedings of the International Astronomical Union, 2007, IAU Symposium, Volume 242, p. 178

Curriculum Vitae

I was born in Göteborg (Sweden) on the 4th of May, 1977. When I was a couple of years old, my family moved to Kullavik, a small village on the coast just 25 km south of Göteborg. Incidentally, I grew up halfway between Chalmers and the Onsala Space Observatory that would later set me on this path that has led me to where I am today.

After finishing my high-school studies at Aranäsgymnasiet (Kungsbacka) in 1996 I spent a year in northern Sweden doing my military service. To see (and hear) the aurora borealis on a cold winter night is a very special experience. Upon returning to southern Sweden I first studied a year as computer/network technician at Komvux (Kungsbacka) before starting my studies in electrical engineering at Chalmers Lindholmen College (Göteborg). In the spring of 2001, while finishing my B.Sc., I bought a small sailing boat and named her “Embla”. Sailing has since then been one of my greatest passions. I still felt that I wanted to continue my studies and after a year of qualifying courses I enrolled in the masters programme “Advanced Techniques in Radio Astronomy and Space Science” at Chalmers University of Technology in Göteborg.

While working on my master thesis “Radio aeronomy of planetary satellites”, under the supervision of Prof. Dr. John Black at the Onsala Space Observatory, I realised that astronomy was something that I could and wanted to pursue. After finishing my master thesis in the spring of 2004, I spent three months as a summer student at Astron, working with Dr. Willem Baan on EVN data of two AGN/Starburst galaxies. The power of interferometry fascinated me. I spent the next year working as a student support astronomer at the Nordic optical telescope (NOT) on La Palma, Spain, and took great pleasure in learning the inner workings of an (optical) observatory.

In the fall of 2006 I started my Ph.D. studies within the Marie Curie programme ESTRELA at JIVE and Leiden observatory under the supervision of Dr. Huib Jan van Langevelde. During my Ph.D. I have been fortunate to work on data from several top observatories such as: the EVN, JCMT, VLBA, ATCA, VLA, Merlin, and CARMA. In particular, I have benefitted from on-site observations at the JCMT and ATCA. I have also participated in several summer/winter schools such as the IRAM 30m school in Spain, the tenth summer synthesis imaging workshop in New Mexico, scientific writing for young astronomers in Belgium, YERAC 2007, as well as five ESTRELA workshops in Europe. Additionally I have had the opportunity to present my work at several international con-

Curriculum Vitae

ferences, including “Astrophysical masers and their environments”, IAU Symposium 242 in Alice Springs, “Massive star formation: observations confront theory” in Heidelberg, “Masers: the ultimate astrophysical tools” in Bonn, and the 9th EVN Symposium “The role of VLBI in the golden age of radio astronomy” in Bologna.

I am currently employed on a joint project between JIVE and the Dutch ALMA centre Allegro on wide field imaging problems. After this I would like to pursue my career in astronomy with a post-doc, hopefully at one of the new generation radio/submm interferometers.

Acknowledgements

First and foremost, I want to express my gratitude to my family back home in Sweden: Mamma and Pappa to whom I owe everything. My siblings: Ulrica, Lasse, Anders and Niklas. Not only have they supported me during all these years, they have also been taking care of my little boat in Sweden, while I have been enjoying myself in Leiden. My nieces Emma and Alva, and my nephews Max and Melker, I always look forward to seeing them when I come home. I thank my grandmothers, Signe and Ulla-Britt, who are always keen to hear about what I am doing. Also, I wish to thank the extended family with sambos, särbos, in-laws, uncles, aunts, and cousins. It's a great big family! I believe that I can also include my good friend Olof here, he always has something to say that puts astronomy in perspective.

This thesis represents the culmination of five years of work on my part. Still, it would not have been possible without the help and support of many others, all of whom I would like to thank. It has been a privilege to work at the Leiden Observatory, with its rich history and its smörgåsbord of expertise and experience. The students, post-docs, and staff make the "Astrochem corridor" a great and inspiring work environment. I especially wish to acknowledge Thanja, for her help with the Dutch part of this thesis. Over the years I have shared my office with several people and I am grateful to all of them for putting up with me. In particular, I want to thank Joseph and Olivier for the last couple of years, and for making it THE office.

During the first three years of my Ph.D., I was employed by JIVE within the ESTRELA network. My special thanks go to the wonderful staff, support scientists, and secretaries at JIVE whose help has been indispensable, in particular to Stephen for all our discussions. I also wish to express gratitude to my fellow "Estrelas" for the great workshops we had together all over Europe, and especially to Nikta and Hayden, my fellows in Leiden.

My collaborators: Floris, Wouter, and Lars. I have benefited immensely from their advice and guidance. I also wish to thank Ania, for our disk-world discussions. The observatory support groups at the JCMT, VLA, ATCA, and CARMA all have my appreciation for the help they have given me. Gary Fuller and his group in Manchester have my gratitude for housing me during my four-month visit in Manchester during the autumn of 2008.

Acknowledgements

During my Ph.D., there was always a Nordic faction present at the institute, and it has been with great pleasure that I have partaken in the traditions that we all (more or less) have in common. With Julelunch, Påskelunch, Glöggkalas, Midsommarfirande and Kräftskivor; Jeanette, Karin, Stefan, Christian & Tonie, Karoliina, Lars, and Jes (& Suzanne) brought a little bit of the North to Leiden. I am also grateful to all my other friends in Leiden (too many to name), for the many hours of kayaking, climbing, kubb, mölkky, bike trips, picnics, poker, and sailing. In short, for making life in Leiden so good.

Last but not least, I want to send a thought and my deepest gratitude to my two grandfathers, Torsten and Verner, who saw the start of this adventure and whom I think of often.

Notes:

